ABSTRACT

Title of Document:	CHARACTERIZATION OF FLEXIBLE FLAPPING WINGS AND THE EFFECTS OF SOLAR CELLS FOR MINIATURE AIR VEHICLES
	Kelsey C. Cellon
	Master of Science, 2010
Directed By:	Professor Hugh A. Bruck
	Department of Mechanical Engineering

Enhancing the performance of Flapping Wing Miniature Air Vehicles (MAVs) requires reducing the weight and total energy loss while increasing the efficiency. This thesis investigates an approach to reduce total energy loss through an energy harvesting technology, flexible solar cells. These cells are integrated with a flexible wing structure, to minimize the addition of weight to the MAV without comprising efficiency (i.e. performance). An optical technique is developed to characterize the effects of adding flexible solar cells to the shape of the flexible wing structure. A customized test stand for measuring lift and thrust assesses the effects of the solar cells on the flight performance of the MAV, both in stationary configuration (i.e. no air flow), and while subjected to air flow in a customized small-scale wind tunnel. The optical technique is combined with lift and thrust results to describe overall

MAV flight performance. These results are then used in a theoretical analysis, developed for predicting time-in-flight, in order to perform a trade-off analysis.

Characterization of Flexible Flapping Wings and the Effects of Solar Cells
for Miniature Air Vehicles

By

Kelsey C. Cellon

Thesis submitted to the Faculty of the Graduate School of the
University of Maryland, College Park, in partial fulfillment
of the requirements for the degree of
Master of Science
2010

Advisory Committee:
Professor Hugh A. Bruck, Chair
Professor Satayandra K. Gupta
Assistant Professor Sarah Bergbreiter

Acknowledgements

As I approach the end of my whirlwind year at the University of Maryland, I must take the time to stop and thank all the people that have helped me along the way. I have had quite a few unique and challenging experiences, most of which would not have been possible without the help and support of the people in my life.

First, I would like to thank my advisor at the University of Maryland, Dr. Hugh Bruck. Few people are willing to take on the task of completing a Master's Degree with a thesis in Mechanical Engineering in a calendar year; even fewer are willing to advise such a student. From our first meeting, Dr. Bruck accepted my time constraints and worked with me diligently to ensure that my thesis (and my degree) would be finished within my timeline. Every time I wondered whether or not I would graduate or found myself unable to solve a problem, Dr. Bruck was able to come up with a focused solution to get my research back on track. Through guiding my graduate student experience, Dr. Bruck has taught me quite a few life lessons, helping me become more prepared to take on a variety of challenges in my future career.

I wish to acknowledge Professors Satyandra K. Gupta and Sarah Bergbreiter for serving on my advisory committee.

I want to thank all of my lab mates in AML. Because my experience was so constrained by time, many things had to be learned on the fly. Wojciech Bejgerowski, Brian Russ, John Gerdes, and Li-Jen Chang spent a significant amount of time familiarizing me with the MAV, the lab, its workings, and were there to answer countless questions whenever I needed them. Many long hours were spent in

the lab, and I was lucky that those long hours were spent with such fun and entertaining people.

This thesis also contained quite a bit of testing, re-testing, and data analysis. I would like to thank Shoshana Bernstein and Jordan Williams for devoting countless hours to help me complete an inordinately large amount of lab work. Without their help, I would have never completed my research, and for that I thank them.

I would like to thank the U.S. Naval Academy and the U.S. Navy for both allowing me to continue my education and for their financial support. Without the VGEP program, getting my Master's Degree this early in my career would not have been possible.

Most importantly, I want to thank my family and close friends. You guys are the most important people in my life, and I love you. Without your constant support and words of encouragement, this thesis would not have been possible. Mom, Dad, Daniel, Adam, Jeremy, Kali, and Alex, this work is dedicated to you.

Table of Contents

List of Figures

Chapter 1:   Introduction

1.1   Background

Currently, miniature air vehicles are being developed with variations on three different wing configurations: fixed-wing, rotary-wing, and flapping wing designs. The large variety of applications for MAVs reveals both advantages and disadvantages to each type of wing design. However, the biological inspiration of the flapping wing design offers the greatest potential in a wider range of missions when compared with the current capabilities of fixed- and rotary-wing designs.

Many MAV applications require the vehicle to be capable of low-speed flight, maintain stationary hover for extended periods of time, take off and land vertically, and perform complex maneuvers. The rotary-wing design is optimal for this type of flight because it allows stable hovering, vertical take-off and landing, as well as obstacle avoidance. Also, well-established helicopter technology can be used to develop this wing design. Seiko Epson Corporation designed a rotary-wing MAV, known as the FR-II, shown in Figure 1. This MAV weighs 12.3 grams and is capable of a three-minute flight time [1].

Figure 1 Seiko Epson Corporation FR-II MAV [1]

The weight balance is essential for rotary-wing flight, therefore decreasing the size of a rotary-wing MAV greatly decreases the aerodynamic thrust, and consequently, the overall payload of the vehicle [2]. The rapid movement of the rotor blades generates a significant amount of noise that can be easily detected during flight, eliminating stealth capability. Because the rotor blades operate at such high speeds, they also have the potential to be hazardous to nearby people, also limiting flight applications, specifically in terms of altitude and small spaces.

The second option to realize MAVs is through fixed-wing flight. Size scaling is also an issue with fixed-wing fliers. Figure 2 shows small fixed-wing MAVs developed at the University of Florida, which were used test aerodynamic changes that occur in small-scale fixed-wing flight [3]. While large fixed-wing MAVs are very successful, as the wings are reduced in size, aerodynamics affecting the wings change to those of low Reynolds numbers, which reduces aerofoil performance, and negatively affects flight capabilities [4]. As the fixed-wing vehicles are scaled down in size, the amount of speed required to generate lift increases dramatically. Many targeted applications for small-

scale unmanned aerial vehicles (UAVs), including indoor flight, require low flight speeds to allow for complex maneuvers, short take-offs and landings, and quick response time required for obstacle avoidance. Since such high speeds are required to keep them aloft, fixed-wing MAVs are often unsuitable for many applications.

Figure 2 University of Florida fixed-wing MAV prototypes [3]

The third option to realize MAVs is through flapping-wing flight. This type flight has the potential to combine the positive aspects of both fixed-wing and rotary-wing flight, while eliminating many of the negative aspects. The flapping-wing style finds its inspiration in animal flight; birds, bats, and even insects have the ability to land and take off in small spaces, hover, quickly change direction, avoid obstacles, perch, and adjust their flight patterns when presented with significant changes in airflow. Flying animals are able to adjust to changing weather conditions instantaneously by varying wing angle of attack, wingtip trace patterns, wing area, and feather orientation, thus maximizing their efficiency in flight at all times. Animals also possess the ability to glide, allowing energy conservation and extended flight times. Since animals possessing flapping wings have such excellent flight characteristics, the potential for flapping wing flight is significant in miniature robotic applications. Flapping wing MAVs, combining the abilities of

hovering, short take-off and landing, gliding, and low speed flight, present an efficient and effective compromise between fixed-wing and rotary-wing flight. As seen in insects, flapping wing flight is possible at even the smallest scales through an increase in flapping frequency.   Harvard University's Microbiotic Fly, shown in Figure 3, is one of the smallest flapping wing MAVs today, weighing 60 mg with a 3 cm wingspan.
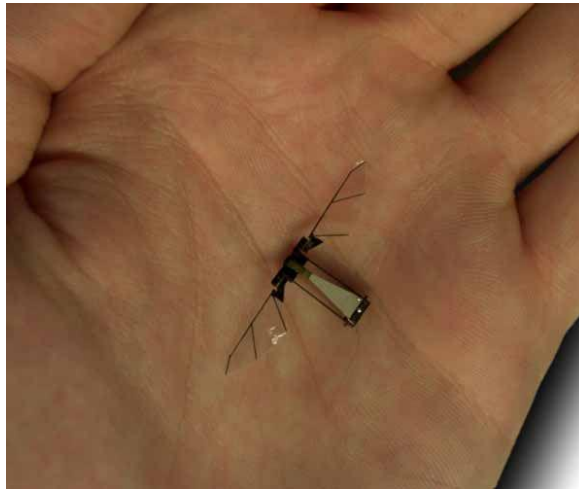
Figure 3 Harvard Microbiotic Fly [5]

In addition to the large range of wing sizes and multiple applications, another huge advantage of flapping wing flight is its ability to operate at a very low frequency when compared to a propeller or rotor. Because low-frequency flight is possible, the noise produced by the MAV can be virtually undetectable, making it suitable for stealth operations.   The combination of potential perching behaviors, as well as visual resemblance to a natural bird, also increases the possible stealth characteristics of a flapping wing MAV. Because of its biological inspiration and the great potential this field contains, flapping wing flight is the best compromise between fixed and rotary-wing flight.

In MAVs, flight endurance is one of the primary concerns for both the manufacturer and the operator. The integration of solar cells into the existing MAV wing structure allows for multi-functionality of the wings. A multi-functional structure (or material) is defined as a material that can perform more than one "primary" function simultaneously or sequentially in time, such that overall system performance can be enhanced. A multi-functional wing structure that not only provides lift and thrust, but also acts as a method of harvesting energy, can be a great improvement to current MAV designs. This combination allows for increased flight time while decreasing the payload contribution of a large power source, thus potentially allowing for either (1) size reduction with the same performance capability, or (2) an increase in overall payload capacity. Should wing multifunctionality prove successful, the integration of multiple functions into single components can be expanded to other aspects of MAVs, continuing the development of state-of-the art unmanned vehicle technology.

1.2   Motivation

The use of unmanned aerial vehicles (UAVs) has become much more prevalent in recent years. Large-scale UAVs have been successfully used in the military, farming, border patrol, search and rescue, mapping, scientific research, and other areas. The combination of the success of larger UAVs and the progression of research in aerodynamics of flight on smaller scales has resulted in the continuing miniaturization of unmanned aerial vehicles. This miniaturization process opens up a whole new world of opportunity for the UAV, as many current applications are restricted by the size of the vehicle. Smaller, lighter, and cheaper miniature air vehicles (MAVs) allow for a wider range of application of UAVs. One such application is improved reconnaissance.

Because MAVs are capable of low-altitude, low-speed flight, they can provide surveillance and gather information about regions that cannot be gleaned from higher altitudes, and can travel into areas that are potentially unsuitable for larger surveillance platforms such as helicopters. Because they are also a much more expendable resource than humans or even helicopters, a large number of MAVs can be deployed at once to survey a large area, thus conserving more expendable resources while still collecting large amounts of data in a efficient manner. The ability of MAVs to travel into unsafe locations makes them quite useful in search and rescue missions and disaster relief efforts. Instead of sending a person or animal into a potentially hazardous area, an MAV could be deployed to inspect the area for those in need of rescuing through any number of mountable devices such as cameras or heat sensors. Because MAVs are small, portable, lightweight, cost-effective, and have many versatile abilities such as rapid deployment and low-altitude, low-speed indoor and outdoor flight, they are a thus far untapped resource that has the potential for many important applications in a variety of fields. Indoor flight capability of MAVs has great potential for application. MAVs could be deployed to inspect buildings that may be structurally unsound during search and rescue missions, or could be used by the military to identify potential threats during building clearing or ship boarding situations. Because MAVs are small and lightweight, one member of any team could carry at least one MAV, making them portable in a majority of situations.

Aerodynamic forces change dramatically when examined for small-scale platforms, significantly challenging the accuracy of theoretical calculations used to predict those forces. This, along with currently broad design variation in the field, and an

inability to generalize performance capability and predict aerodynamic forces through experimentation, drives the need to develop a method to describe how the wings move throughout the flap cycle, and explain why certain wing designs generate certain lift and thrust forces. If such a method is developed, especially one that can be applied to a variety of different wing designs and MAV platforms, MAV development would increase and performance would exponentially improve, since developers would have an understanding of why certain wing structures performed better than others. Thus, development of a wing characterization method that is widely applicable in the field of MAVs is crucial to the expansion of the field.

Multi-functional structures combine more than one functional requirement into a single structural component to create better efficiency in the overall design. For example, Thomas et. al. [6] describe the combination of structure and battery in the design of an electric-propelled UAV as an example of a multi-functional material system. For UAVs, flight endurance time is an important performance metric. Flight endurance time is directly related to the energy supplied by the battery, the weight of each component of the UAV, and aerodynamic parameters. Thus, combining the battery with one of the components of the UAV can result in an increase in the available energy, or a decrease in the vehicle weight. Introducing a multi-functional structure-battery into a UAV can increase the available energy, decrease the structure weight, and possibly the battery weight, along with the addition of structure-battery weight. The implementation of solar cells on the wings of the current MAV at University of Maryland will have many effects; however, the motivation behind this research is to determine whether the reduction of compliance in the wings, through the addition of solar cells, results in better flight

endurance than the wings that do not have solar cells. Should this prove to be the case, and the multi-functional wing improves flight endurance, the implementation of multi-functionality in the field of unmanned aerial vehicles can expand significantly.

In summary, flapping-wing MAV platforms are a highly sought-after instrument in many important applications because of their cost, light weight, portability, and low-speed and low-altitude indoor and outdoor flight capabilities. However, there are several important limitations of the current MAV characterization methods. The aerodynamic forces affecting small-scale fliers such as the MAV are relatively uninvestigated, driving the need to develop a method to describe flapping-wing motion during flight for MAV platforms. Multi-functional structures, which combine more than one functional requirement into a single structure, have been successfully implemented in fixed-wing MAVs with positive results. However, the issue of compliance in flapping-wing fliers has thus far prevented batteries from being integrated into flapping-wing structures. Novel flexible solar cells promise a viable solution when integrated into flapping-wing MAVs, with potentially minimal effects on the wing compliance. The implementation of solar cells as an additional power source has the potential to reduce the battery weight and increase the payload capacity and/or flight endurance. However, the multi-functionality of the MAV depends on whether the power supplied by the solar cells is sufficient to significantly increase flight endurance when compared with a MAV without solar cells.

1.3 *Thesis Goals and Scope*

The challenges outlined in the previous section demonstrate that the current MAV characterization methods have their important limitations. Additionally, the

8

implementation of solar cells as an additional power source causes certain concerns in terms of both the flapping-wing structure compliance, as well as the flight endurance gains. Therefore, the goals of this thesis are to (1) develop a generalized wing characterization method for MAV platforms to correlate lift and thrust values with wing shapes encountered at different points in the flapping cycle, (2) analyze the effects of solar cell integration with the wing structure using the developed characterization methods, and (3) develop a method to analyze the multi-functional performance of an MAV with integrated solar cells.

To reach these goals, many tasks had to be completed. First, the differences in lift and thrust measurements due to different wing constructions were investigated. Through high-speed imaging from multiple angles, the leading spar displacement of each wing design was investigated, and a two by four grid was implemented on each wing design to determine the blowback characteristics throughout the flap cycle. From there, centroid locations both along the leading spar and perpendicular to the leading spar as well as volume calculations were performed to compare the values for different wing designs over the course of the flap cycle. Using the same grid structure that was used for blowback characterization, length changes were used to develop both calculated and measured three-dimensional images of the deformed wing at different points throughout the flap cycle. By interpreting results of the leading spar displacements, blowback characterizations, centroid calculations, volume calculations, and measured and calculated imaging, the different wing designs can be characterized, and the lift and thrust forces generated by each of the wing sets can be justified.

Second, the developed wing characterization method was applied to two wing designs with four different solar cell configurations. Based on these findings, combined with the lift and thrust forces generated for the solar cell wings, the effects of the addition of solar cells to flexible flapping wings were determined.

Finally, the multi-functional effects of solar cells integrated into flexible flapping wings were considered. The impact of lift, thrust, and power on overall time of flight were compared for wings both with and without the solar cells, proving the future work in solar cell implementation in flapping wing flight is beneficial for the MAV field.

1.4   Organization

Chapter 2 contains a literature survey of relevant MAVs and technology associated with this thesis. There are three basic areas covered by the literature survey, each of which is equally important in the development of this thesis. The first area covers current MAV platforms, including tail designs, wing designs, and mechanism designs. The second area covers multi-functional applications as they relate to MAVs, either through platforms already being tested, or concepts that can be applied to the MAV design. The third and final area covers image characterization techniques, as they apply to MAV designs. The literature survey concludes with a summary of how these three areas are applicable to this thesis.

Chapter 3 contains a discussion of the 'Jumbo Bird' miniature air vehicle platform. This platform is used to develop the wing characterization and do solar cell testing. The sections discuss the body design, the electronic components, the wing design, and the mechanism design associated with the 'Jumbo Bird' platform. The test stand, wind tunnel, and imaging equipment are also introduced. The measurement

techniques for the generated lift and thrust forces generated are described. The chapter concludes with a summary of the new developments in equipment.

Chapter 4 contains a complete description of the wing characterization developed in this thesis. This chapter characterizes the lift and thrust forces generated by six different wing designs, as well as a method for tracking the movement of the leading spar of the wing. The model for measuring length changes to determine blowback characteristics is also presented. The development of the centroid calculation method, including the necessary perspective corrections performed, is presented with the calculation results. The development of the volume calculation method, which uses the bi-linear interpolation method, is presented as well, including the results from the calculations. The final portion of the wing characterization method presents the calculated and measured imaging. The chapter concludes with a summary of the wing characterization method and justification of the lift and thrust results generated for the different wing types.

Chapter 5 contains a discussion of the solar cells tested in this thesis. The chapter begins with a discussion of the motivation behind solar cell testing, and a description of the solar cells used in testing. The wing characterization method is performed on the different solar cell configurations, and the results are compared with the results of the original wing designs. The chapter concludes with an analysis of the impact of solar cells on the compliance of the wing.

Chapter 6 contains a discussion of the multi-functional performance of the MAV with the addition of the solar cells discussed in chapter 5. The chapter begins with a theoretical analysis of time-of-flight of the MAV, presenting the assumptions made, and

the development of the final equation. The theoretical time-of-flight based on the solar cell ratings is also determined. Using the theoretical equation determined earlier in the chapter, experimental predictions of time-of-flight are made and compared between the wings with, and without, solar cells. The chapter concludes with a discussion addressing the impact of multi-functionality on the performance of MAVs.

Finally, Chapter 7 presents the intellectual contributions resulting from this thesis. It also suggests the possible future directions that can be initiated as a continuation of this work.

Chapter 2:   Literature Review

This chapter is a literature survey of relevant MAVs and technology associated with this thesis. There are three basic areas covered by the literature survey: (1) current MAV platforms, including tail designs, wing designs, and mechanism designs; (2) multi-functional applications as they relate to MAVs; and (3) image characterization techniques, as they apply to MAV designs. Each section presents information on the topic and explains its application to this thesis.

2.1   MAV Designs

The field of flapping wing miniature air vehicles is relatively new, and is constantly growing and expanding. There are many designs currently being explored, with each one emphasizing a different aspect of the vehicle's construction. Because the size range of unmanned flapping wing air vehicles is so large, due to their wide variety of application, "miniature" in respect to UAVs constitutes any flapping wing flier weighing between 10 and 100 grams. Flapping wing MAVs can be divided into three major categories that are critical in determining an MAV's flight envelope: directional control scheme, wing design, and mechanism design [7].

While control schemes are not the focus of this thesis, the work presented by John Gerdes in his survey paper can be used to elucidate on the effects that integrating solar cells may have on the control schemes. For example, adding solar cells to the tail structure, much like this thesis presents for the wing structure, may change the performance accordingly. Thus, the characterization techniques and analyses that we

present for the wing could be used to determine this performance change, and the consequent effects on the control of the MAV.

While the mechanism was not a portion of the MAV that was considered heavily in this thesis, an understanding of the mechanism's workings and how to repair the mechanism is crucial, as the mechanism allows for testing to occur. For the investigation into the wing characterization and solar cell implementation, a single mechanism design was used consistently throughout testing, to eliminate additional variations in the results. Also, the mechanism and wing concepts are inherently coupled; if the wing design is changed, the lift and thrust forces produced change, and the mechanism must be tailored to fit those specific lift and thrust forces. Thus, an understanding of the current working mechanisms in the MAV field, as well as the types of applications they are used for, was crucial to the development of this thesis.

2.1.1   Wing Design

Wing design varies greatly across the spectrum of MAV platforms. In current applications, there are three different types of wing design: flapping wings, four clapping wings, and folding wings [7]. Flapping wing designs are bio-inspired. Birds, bats, and a variety of insects all employ flapping wing flight; however, the type of flight varies with size. Birds, which generally have larger wingspans, use a much slower flap rate than insects, whose smaller wings require a much greater flap rate to allow for flight. This same relationship between wing size and flap rate exists in MAVs; as wing size decreases, a higher flap frequency is required to generate enough lift and thrust for the MAV to stay aloft. Thus, MAV designers are presented with a unique challenge, since practical aerodynamics break down with small wings. The microbat, which was

discussed in the directional control scheme section, uses flapping wings created using MEMS technology. The 9 inch wingspan, constructed out of titanium-alloy metal (Ti-6Al-4V) structure materials and a poly-monochloro-para-xylelene (parylene-C) membrane, had variation in parameters such as chord and spar width, membrane thickness, number of spars, and sweep angles [8]. The MEMS technology allowed the wings to be manufactured in exactly the same way every time, eliminating any variation due to construction, since even small variations can create large discrepancies in results [8].
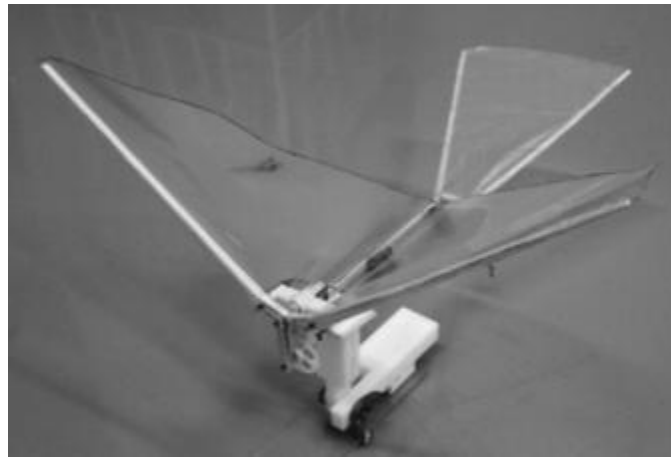
Figure 4 MEMS wings with PVDF sensing capability [10]

Another MAV constructed with MEMS technology has a membrane made of a PVDF skin, allowing it to act as a real time load sensor to directly analyze flight performance [9, 10]. This MAV can be seen in Figure 4. Being able to accurately measure flight performance is a key aspect of future development within the MAV field.

Flapping wings have also been constructed by hand; the wings of the small bird and big bird at the University of Maryland, as well as the ornithopter at the University of Delaware, are all constructed using stiff, lightweight rods as structural materials and a

thin Mylar-based film as the wing surface [11, 12, 13]. However, because these wings are man-made, repeatability in manufacturing is a drawback, as small differences are present in each set of wings constructed. The I-fly Vamp and Wasp within the toy market also employ thin films stretched across front and rear spars in their flapping wings.

Four clapping wings include any MAV that uses one or two pairs of wings flapping against each other; this motion cancels out any vertical inertial oscillations created by a sing set of wings, enabling more stable flight. The Osaka Slow Fliers Club MAV, the Wowee Flytech Dragonfly MAV, and the Wingmaster MAV all utilize pairs of wings constructed of thin film that flap in opposing phase [14,15]. The Delfly Micro, Delfly I, and Delfly II also use similar wing construction, with the Delfly II being the most advanced since it can fly forward, backward, and hover [16]. The NPS MAV, with its non-traditional construction, is classified as a clapping wing MAV because its pair of wings flaps in counter phase, propelling the MAV forward while also generating lift [17]. The NPS MAV is the most energy efficient of the MAVs discussed, because its unique design allows all energy to be used solely to flap the wings, while in other models, some energy is expended in excessive oscillations in the body or in carrying structural components that don't contribute to flight [17]. Another form of clapping wing flight is the three-way clap and fling, which is used to augment lift. Clap and fling, which involves the generation of lift where the wing pairs meet on the left and right sides, was shown to be successful in insect flight in multiple studies [18-24]; however, the concept of three-way clap and fling adds an additional component of lift by incorporating the

meeting of the opposing wing pairs at the top of the flap cycle. This method was successful in an MAV at WSU, seen in Figure 5 [25].

Figure 5 WSU MAV [25]
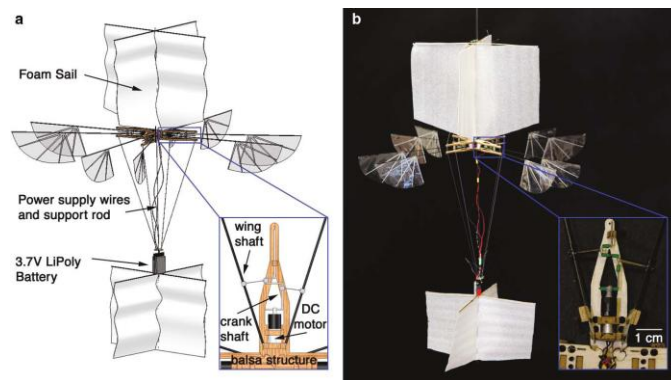
Figure 6 Passively stable hovering MAV [26]

Another clapping wing MAV, designed to mimic insect flight, uses the concept of passive stability through generating opposing forces and the addition of sails to reduce and absorb oscillatory motion to be able to hover [26]. This MAV can be seen in Figure 6.

Folding wings are another wing design aimed at mimicking flight patterns of larger birds. Birds flap their wings differently during take-off and at cruising altitude; because they do not have airflow over their wings during take-off, birds must alter their wingspan to create more lift. So, during the up-flap of the flap cycle, birds bend their

wings in towards their body, minimizing the negative lift created, and then extend them to their full wingspan during the downward flap to maximize positive lift. This concept is one that is difficult to achieve in MAVs, since adding actuators to initiate wing folding would cause significant increases in weight. Mueller et. al. [28] created a successful MAV that exhibited one-way compliance, allowing the wings to passively fold in a fashion similar to the wings of large birds during take-off without the addition of heavy actuation systems. This MAV is pictured in Figure 7.

Figure 7 Wings with one-way compliance [28]

Billingsley et. al. [29, 30] attempted a similar type of wing that created significantly more lift in stagnant testing; however, their design did not succeed in actual flight-testing because the extreme folding of the wingspan negatively affected the force balance in flight.

An understanding of current wing design is an important portion of this thesis, because it directly affects how the wing characterization method is approached and influences how the wings are modified so that solar cells can be added. Without a

thorough understanding of current wing constructions, an applicable wing characterization method would be difficult to develop.

2.1.2 Summary

As seen in the previous sections, there are a large number of capable flapping-wing miniature air vehicles that can be classified by the tail structure, wing design, and mechanism type. Each of the different MAVs presented have different strengths and weaknesses; Table 1 highlights the major aspects of the different platforms discussed, so that they can be compared. Currently, flapping-wing MAVs are capable of performing a variety of missions that fixed or rotor wing fliers cannot; however, the small scale required for successful flight is a drawback that must be overcome for future advancement in the field. Areas such as autonomous flight, payload increase, and more sophisticated wing control have great potential for expansion; autonomous flight would allow for take-off, landing, and perching to occur without assistance, payload increase would improve flight duration and the ability to carry additional sensors for various missions, and more wing control would better approximate the flight of birds, since their many degrees of freedom improve maneuverability, endurance, and flight in adverse conditions.

Table 1: Physical data [7, 31-38]

Category	Name	DOF	Weight (g)	Span (in)	Length (in)
Clapping Wing MAVs	Wright State University	2	12.56	7.9	9
	I-Fly I-bird/fairy/wings (wingsmaster ornithopters)	2	12	10.5	8.25
	Delfly I	3	30	19.69	20
	Delfly II (hover)	3	16.07	11.02	11
	Delfly II (forward)				
	Delfly Micro	3	3.07	3.94	4
	NPS Flier Dr. Jones	2	12.4	10.6	7.09
	OSFC Flier	2	1.47	2.36	2.76
	Flytech Dragonfly	2	28.35	12.3	16.5
Flapping Wing MAVs	I-Fly Vamp/Wasp	2	13	10.5	8.5
	Microbat (UF/DARPA)	2	12.5	9.06	6
	UMD small bird	2	16.3	13.5	8
	UMD big bird	2	47	22.5	10.5
Animals	Northern Oriole	many	35	10.5	7
	Ruby-Throated Hummingbird	many	3	4	3.5
	Northern Cardinal	many	45	11	8.5
	Canary	many	23	6.5	5

2.2 Multi-functional Applications

Multi-functional materials are designed to perform more than one function, either simultaneously or sequentially, and improve system performance by reducing the number of subsystems required to execute those functions [39]. By creating structural components with heat transfer capabilities or battery function, or integrating sensors into structures to detect and suppress noise and vibration, or creating nanocomposites that both reinforce and assess impact damage, the number of subsystems required for an

object is reduced, while overall system performance is enhanced. Multi-functional materials are the first step in ideally designing each system for its intended purpose.

2.2.1 Multi-functional Structure-Battery Concept

Structural components make up one of the subsystems of every multi-functional material; thus, it is a frequently chosen subsystem for incorporating multiple functions. Because it generally does not move, using the structure of a material to serve more than one purpose can be less complicated than utilizing other subsystems. Also, there are known methods established to track structural performance, making the success or failure of the components easy to determine and analyze for improvement. For these reasons, the structural components of flapping wing vehicles are prime candidates for creating multi-functional components.

In analyzing flapping wing vehicles, it is apparent that one of the limiting factors of performance is battery life. Due to the small size and low weight of current MAVs, the payload capacity is very low, limiting the power supply that can be carried. Integrating a power source into the structure of a device is a form of multi-functionality, as it allows for weight savings while providing energy and structural support for the system. Unmanned air vehicles stand to greatly benefit from multi-functional structure-power materials, which provide structure while also providing some method of propulsion energy storage, because replacing simple structural parts with these multi-functional materials increases endurance, range, or payload capacity [6]. The applicable areas of structure into which batteries or other sources of power can be integrated include the body, the tail, and the wingspan. Although the majority of the research available involves using batteries as structural components in the body and wingspan, a great deal

of potential exists for integrating flexible components that harvest energy into the wings and tail.

Liu et al. [40] have designed and fabricated multi-functional lithium ion batteries with elastic and structure load bearing capabilities. Different properties are realized by varying the polymer matrix used; for elastic batteries, an elastic polymer matrix is used, and for load bearing capabilities, a structural polymer matrix reinforced with fibers is used [40]. As seen in Figure 8, a structural battery was fabricated using a carbon fiber reinforced PVDF composite; the battery possessed good mechanical strength and minimal energy storage capabilities. All particulate fillers in the design are replaced by fibers and a high molecular weight polymer serves as the structural polymer binder [40].
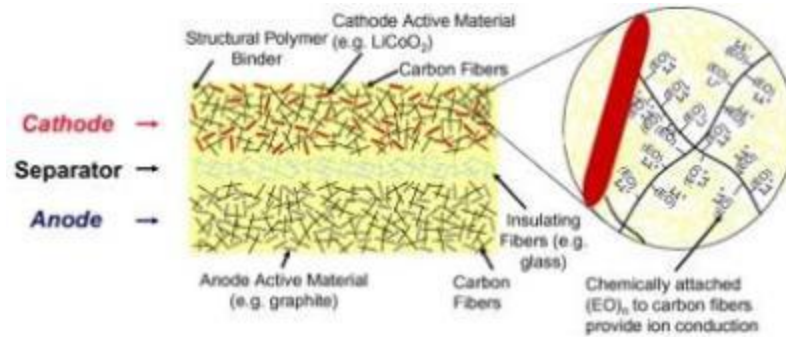
Figure 8 Design of a structural battery [40]

Although this research cannot directly be applied to flapping wing vehicles, it constitutes a step towards developing energy sources that can be manipulated to serve a wider range of applications. This research could potentially lead to the development of flexible battery composites to be implemented in the wings and tail of flapping wing miniature air vehicles, or the development of rigid structural batteries to be implemented

in the body of the same flapping wing MAVs, providing multi-functional energy supplies.

2.2.2 DARPA Structure-Power Concepts

Many companies invested in the world of unmanned aerial vehicles have begun research programs dedicated to the expansion of multi-functional structure-power concepts. Multi-functional structure-power concepts, once completely developed, may have an enormous impact on the field of unmanned aerial vehicles because of the current energy limitations that exist. Once energy sources are no longer limited, the field of UAVs, especially MAVs, should be able to expand exponentially. DARPA is pursuing three different structure-power concepts: (1) structure-battery, (2) autophagous structure-fuel, and (3) variform structure-power. In the structure-battery concept seen in Figure 9, a commercially available plastic-lithium-ion battery system is combined with the wing skin of the Wasp micro-air vehicle. Although the overall weight of the MAV does not decrease, the endurance improves by twenty minutes, making the multi-functionality effective [39]. Another example of this structure-battery concept is found in the Black Widow MAV design seen in Figure 10, also part of DARPA research. The Black Widow MAV also incorporates lithium-ion batteries, and the future design, if successful, although increasing the mass by forty grams, should increase the flight time by forty minutes, which is a 133% increase from the current flight time of thirty minutes [6].
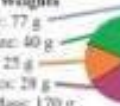
Multifunctional Designs		Conventional Design
PLI Wasp I (Flown)	PLI Wasp II (Notional)	Kokam Wasp (Notional)
4x 24.5 g — 3-Layer PLI Cell	2x 49.5 g — 6-Layer PLI Cell	2x 38.5 g — Kokam Cell
107 minute endurance	**126 minute endurance**	**115 minute endurance**
Electrical	Electrical	Electrical
* Cruise Power: 6.5 W	* Cruise Power: 6.5 W	* Cruise Power: 6.5 W
* S-B Sp. Energy: 136 Wh/kg	* S-B Sp. Energy: 161 Wh/kg	* S-B Sp. Energy: 185 Wh/kg
* S-B Sp. Power: 68 W/kg	* S-B Sp. Power: 67 W/kg	* S-B Sp. Power: 86 W/kg
Weights	Weights	Weights
* S-Battery: 98 g	* S-Battery: 97 g	* Battery: 77 g
* Structure: 20 g	* Structure: 20 g	* Structure: 40 g
* Motor: 25 g	* Motor: 25 g	* Motor: 25 g
* Avionics: 28 g	* Avionics: 28 g	* Avionics: 28 g
* Total Mass: 171 g	* Total Mass: 170 g	* Total Mass: 170 g

Figure 9 Design optimization of flight endurance of Wasp MAVs [39].

Black Widow Design				Notional Design
1	2	3	4	5
Current Design				
• Eagle-Picher cells	• NiMH batteries	• 2-ply PLI cells	• 3-ply PLI cells	• 4-ply PLI cells
• Primary	• Rechargeable	• Rechargeable	• Rechargeable	• Rechargeable
• 15 cm span	• 15 cm span	• 15 cm span	• 15 cm span	• 28 cm span
• 81 gram mass	• 71 gram mass	• 82 gram mass	• 101 gram mass	• 121 gram mass
• 30 min endurance	• 5 min endurance	• 29 min endurance	• 34 min endurance	• 70 min endurance!
• Flight tested	• Flight tested	• Wind tunnel test	• Wind tunnel test	
		• Structural mockup	• Structural mockup	

Figure 10 Black Widow MAV design progression [6]

Although these designs are marked improvements from the majority of current battery power sources in the field of MAVs, they are only applicable to fixed-wing

platforms, or platforms that have large structural surface areas within which these larger, flat batteries can be integrated. Also, the ideal designs, which incorporate batteries into structures, would be accomplished without any weight additions, making final product solely an improvement from the previous model.

The second concept, autophagous structure-fuel, incorporates a fuel source into the structure of the UAV, allowing it to provide structural support during high or peak loading before being utilized as an energy source [39]. Currently, two autophagous structure-fuel concepts are being developed; a super-corroding Mg-Fe alloy that generates heat and hydrogen gas when exposed to an electrolyte and a carbon fiber reinforced polymer that provides energy when combusted [39]. This type of energy harvesting is only applicable in really large UAVs that require large bursts of energy early in use, since those UAVs require a large amount of energy to reach flying altitudes, and then much less energy to maintain flight. MAVs generally require sustained amounts of energy, not bursts, and their structures are very weight conscious, making very little extra room for even short-term energy storage. The final concept, variform structure-power, focuses on developing morphing structures whose geometries can change with the amount of fuel, and has yet to be seriously investigated [39]. Much like the autophagous structure-fuel concept, this concept would be more applicable to large UAVs; MAVs are small enough that weight placement affects flight performance, making an energy source with changing geometry difficult to effectively incorporate with good results.

DARPA's work on the development of power-structure concepts is essential to the development of better multi-functional capabilities within the MAV field. Although none of these methods can be directly applied to flexible flapping-wing vehicles, since

adding batteries to the wings greatly inhibits compliance, the most important function of the wing structure, this concept of adding a power source to the wing influenced the idea of flexible solar cell integration into flexible flapping-wing MAVs, which is developed in this thesis.

Integrating power sources into structural components is an integral multi-functional concept with many future possibilities. Expanding on the examples previously described would greatly enhance the field of multi-functional structures and allow cutting-edge technology, such as UAVs, to make marked improvements in endurance and range. Multi-functionality within UAVs and MAVs would allow for rapid growth and expansion in that field, creating a much wider range of applications and performable tasks.

2.3   *Visual Image Correlation with Flexible-Material Rigid Wings*

As stated previously, one of the greatest difficulties in developing flexible flapping wings for small-scale MAVs lies in the lack of knowledge available to predict aerodynamic forces, and thus flight patterns and behavior, for small-scale aerial vehicles that operate at very low Reynolds numbers. Because mathematical models do not exist, another method must be developed to characterize aerodynamic forces and their effects on flexible wings. One such method, as performed at the University of Florida, is visual image correlation [41]. While a simpler approach in terms of technology, set-up, calibration, and overall time commitment was chosen for this thesis, work in the area of VIC is highly applicable to flexible flapping-wing characterization methods and an area for future work with flexible flapping-wing MAVs.

The method of visual image correlation, pioneered at the University of South Carolina, is a process in which the displacement field of an object is calculated by tracking the deformations of a random speckling pattern applied to the surface of that object [44]. At the University of Florida, this method was applied to a flexible-material fixed-wing MAV, seen in Figure 2 [41]. The setup used, seen in Figure 11, involved a wind tunnel with two ceiling-mounted synchronized cameras and two lamps to increase the exposure of the images captured [42]. The VIC setup is dependent on the two cameras obtaining instantaneous pictures; thus, a specialized setup is used to engage the triggers for each camera simultaneously [41]. The calibration of this setup is extremely challenging, since precision is a must. The VIC system then takes the images, compares them with an established zero parameter, and produces a displacement field with the geometry of the surface in x, y, and z coordinates and displacements described as u, v, and w [41].

Figure 11 Visual Image Correlation setup at the University of Florida [42]

Through this method, the team at the University of Florida was able to obtain very detailed and precise images of the flexible fixed wings at different angles of attack,

allowing for the best angles of attack for different types of flight at different frequencies to be determined [42]. Figure 12 shows an example of the type of image results obtained using VIC.
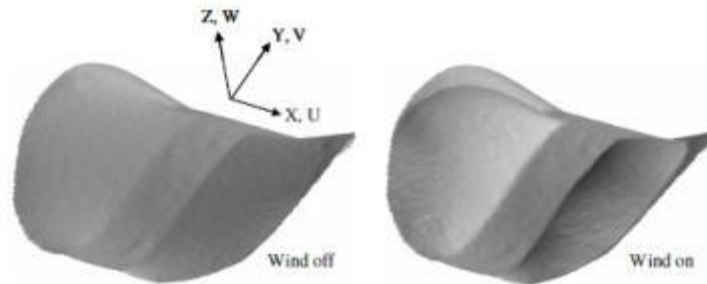
Figure 12 Shape changes of a perimeter reinforced wing [42]

Visual Image Correlation is a state-of-the-art technique that has proven extremely beneficial in obtaining object shape imaging, displacements, and strains in flexible fixed-wing MAV platforms. However, this technique requires expensive equipment, highly precise calibration, and detailed set-up. While the wing characterization method presented in this thesis utilized a much simpler method, the concept of VIC has great potential for application to flexible flapping-wing MAVs instead of simply flexible fixed-wing platforms.

2.4   Summary

In this chapter, three different areas of literature were presented: (1) current MAV platforms, including tail designs, wing designs, and mechanism designs; (2) multi-functional applications as they relate to MAVs; and (3) image characterization techniques, as they apply to MAV designs. In the MAV platforms section, examples of all current flapping-wing MAV platforms were described, based on their tail design,

28

mechanism design, or wing design. While it is obvious how the wing design section is applicable to this thesis, tail design is an area with potential for future work and mechanism design is coupled with wing design, as the lift and thrust forces generated by the wing must be able to be handled and transmitted through the mechanism. In the multi-functional application section, structure-battery concepts and DARPA fuel concepts were discussed; although the structure-battery concepts cannot be directly applied to MAVs, research in that area may eventually be used in MAVs, and the DARPA research is already being used in fixed-wing MAV platforms, with potential for future work in flapping-wing platforms. In the image characterization section, the concept of visual image correlation was introduced; while that technique was beyond the scope of this thesis, there is potential for future applications of this method to flapping-wing MAV platforms.

Chapter 3: 'Jumbo Bird' Flapping Wing MAV

The 'Jumbo Bird' flapping wing MAV was designed and manufactured in the Advanced Manufacturing Lab at the University of Maryland. The 'Jumbo Bird' is the most recent MAV manufactured at UMD; its predecessors include the Small Bird and the Big Bird [12, 13]. Like all flapping wing MAVs, the major components include an electronic system, a body, and a flapping mechanism. The primary concerns for the MAV were weight savings and efficiency. Therefore, it was desired to determine the lightest electronic components that were capable of transferring battery power to the mechanism, and the lightest flapping mechanism that efficiently transformed electric power to flapping motion. Also, a minimal volume body design that promotes stability, while contributing as little weight as possible, was necessary. The original 'Jumbo Bird', as developed by Gerdes [43], was comprised of lightweight electronic components, a foam body design with carbon fiber rod reinforcing, and a compliant mechanism . While the electronic components of the MAV remained the same, improvements have been made in the body design and compliant mechanism to create a more stable flying platform.

3.1   Electronic Components

In order for an MAV to fly successfully, five major electronic components are necessary: (1) the battery to supply power; (2) the motor to convert the power into rotary motion, (3) the speed controller to adjust the wing flapping frequency, (4) the servo-motor to adjust the tilt of the tail, and hence, to control the direction of flight, and (5) the receiver to capture the signal from the radio controller and send it to the speed controller

and the servo [43]. Payload capacity is highly desired for most MAVs capable of real-life applications. In the 'Jumbo Bird' design, payload capacity was considered as one of the main performance measures, and therefore, the lightest electronics available on the market were selected.

3.1.1   Brushless Motor

The motor selected to convert electronic power to rotary motion is the LRK 13/6/11Y brushless DC motor. This motor, as seen in Figure 13, was selected based on its high thrust output of 210 grams, good efficiency, compact size, and light weight [43].
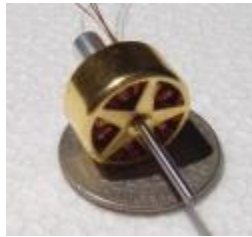
Figure 13 LRK 13/6/11Y brushless DC motor [44]

3.1.2   Speed Controller

The brushless DC motor requires a speed controller to operate; thus, a lightweight, brushless speed controller seen in Figure 14 was selected to convert the throttle signals from the radio controller into the electronic pulses received by the motor. The Feigao 6A brushless electronic speed controller is rated for six Amperes of current draw. Although the selected motor requires only three Amperes of current, a speed controller rated for a larger current draw was necessary due to the irregular loading

pattern introduced by the flapping wings. This solution also helped during slow speed flight, where less air flow introduced overheating as a risk factor [43].

Figure 14 Feigao 6A brushless electronic speed controller [45]

3.1.3 Receiver

A compatible remote control receiver was necessary to connect the radio controller to the speed controller and servo. The lightest receiver that was compatible with the Feigao speed controller was the Microinvent Minor, seen in Figure 15. This receiver weighs only 0.75 grams and is equipped with five channels. Since only two channels are needed for the speed controller and servo, three remaining channels are available to serve additional functions should the need arise.
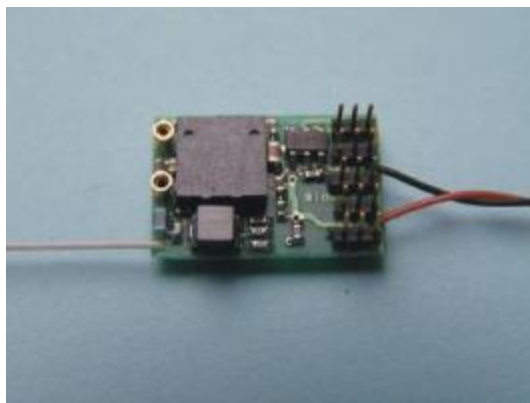
Figure 15 Microinvent Minor receiver [46]

3.1.4 Servo

In order to steer the MAV, the tail was attached to a servo-motor which controlled the tail's tilt. The lightest available servo was selected, the Blue Arrow S0251 servo shown in Figure 16. The tail, acting as a rudder by disrupting the airflow and creating an uneven drag left to right, is rotated by the servo based on the signals sent by the radio controller to the receiver. Although lighter actuators do exist, such as the magnetic actuator employed in the UMD Small Bird, they are impractical for the large size of the 'Jumbo Bird'. The concept of an elevator was also considered for the 'Jumbo Bird' design. However, since flapping frequency has the main impact on MAV elevation, the elevator servo was deemed impractical in a lightweight MAV [43].

Figure 16 Blue Arrow S0251 servo used for tail rudder actuation [47]

3.1.5 Battery

The final electronic component necessary to facilitate the flight is a battery. Three Full River lithium polymer battery cells, seen in Figure 17, were wired in series to create a battery pack providing 11.1 volts of power. Because these batteries come in a variety of sizes, the weight of the battery pack can be altered based on the desired amount of payload; however, lighter battery packs translate into shorter flight time. The typical battery pack used provides 250 milliamp-hours of power and weighs approximately twenty grams with the lightweight connector wires and packaging. The battery pack is a significant contributing factor to the overall weight of the MAV [43].
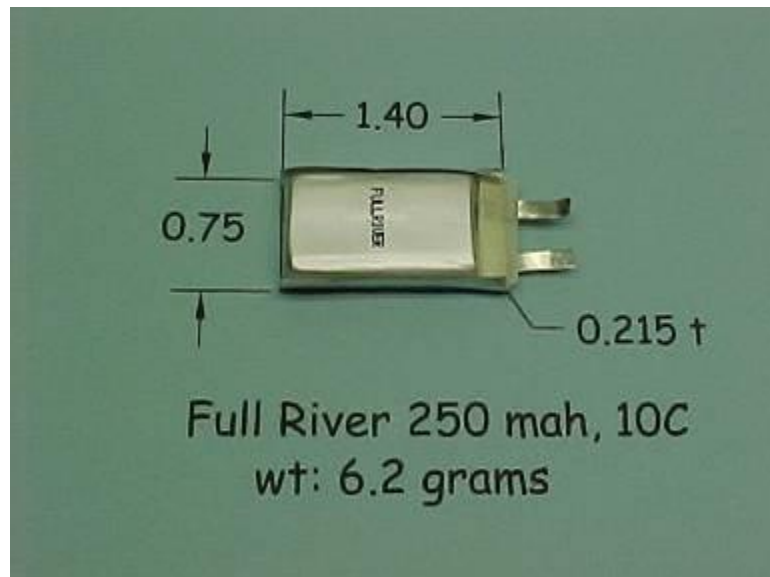
Figure 17 Lithium polymer battery cell [48]

3.2 *Body Design*

3.2.1 Main Body Design

The main body of the 'Jumbo Bird' flapping-wing MAV serves no purpose except to connect the wings to the mechanism to the tail and provide a structure to which the electronic components can be attached. The original body for the 'Jumbo Bird' was constructed of thin foam made stiff by 2 0.06" thick carbon fiber rods aligned vertically, one above the other. These rods inserted into the mechanism. The wings, tail, and other electronic components were attached using heavy-duty hinge tape [46]. Because the foam provided very little structural support, the MAV body was prone to twisting during flight, primarily caused by the lack of support in the connection of the servo to the rest of the body. The body was redesigned, removing the foam shell and using instead four 0.06" thick carbon fiber rods arranged in a diamond, to provide both horizontal and vertical support. New attachment pieces were machined for the mechanism and servo, creating firm, secure attachment points for the mechanism, servo, and tail. The new body design and attachment pieces are seen in Figure 18 and Figure 19.

Figure 18 New UMD MAV body design

Figure 19 MAV tail attachment

3.2.2   Wing Design

The wings of any flapping wing MAV are one of the most crucial components governing overall performance in flight.   Wings affect the endurance, speed, maneuverability, climbing, gliding, and other behaviors, as well as provide the capability to support the weight of the MAV and any additional desired payloads.   The wings are also the source of lift and thrust; flexible flapping wings deform as they are accelerated through the flap cycle into an aerofoil shape and aerodynamic loading produces large angles of attack to generate thrust and lift when in a moving airstream [46].   Because the wings are such a crucial component for successful flight, their design is extremely important.   The wings used in the 'Jumbo Bird' MAV are made of carbon fiber rods of varying thicknesses to provide structure, and coated Mylar-based foil to provide a lifting surface.   Because the used Mylar-based foil was coated with a thermally-activated adhesive, no adhesives were necessary in the construction of the wings.   The carbon fiber rods were designed to act as spars, similar to that of skeletal structures in bats and birds. The general approach to the layout of the spars is seen in Figure 20, with each wing being

constructed with the same Mylar-based foil pattern. The span L was set to 13 inches and the chord H was set to 6 inches for every wing design, resulting in an overall surface area of 68 square inches for each wing [46]. Six prototypes were constructed; their specific parameters can be seen in Table 2.
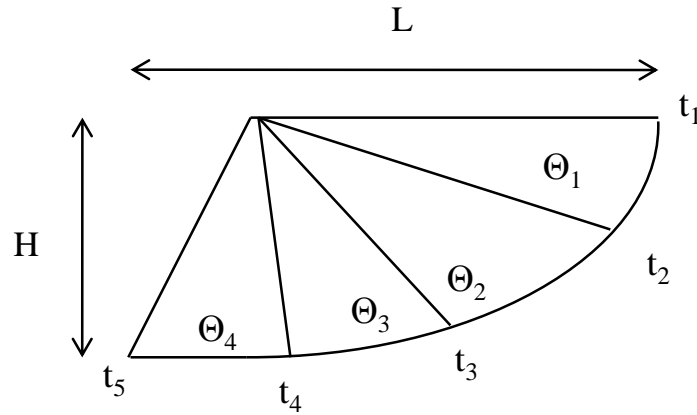
Figure 20 Wing configuration template [46]

Table 2: Wing prototype parameters [46]

Wing	t_1	t_2	t_3	t_4	t_5	Θ_1	Θ_2	Θ_3	Θ_4
A (655)	0.06"	0.05"	0.05"	-	-	36	69	-	-
B (63435)	0.06"	0.04"	0.03"	0.04"	0.05"	20	19	32	34
C (6445)	0.06"	0.04"	0.04"	0.05"	-	19	51	35	-
D (6445v2)	0.06"	0.04"	0.04"	0.05"	-	34	36	35	-
E (6445v3)	0.06"	0.04"	0.04"	0.05"	-	69	17	19	-
F (6445v4)	0.06"	0.04"	0.04"	0.05"	-	17	17	71	-

The wings were named based on the thickness and number of spars used in the carbon fiber rod structure; for example, wing A is also referred to as 655 because its three spars are 0.06", 0.05", and 0.05" thick moving from leading edge to trailing edge.

3.2.3 Tail Design

The tail is constructed of the same Mylar-based foil and carbon fiber rods as the wings. It is designed as a triangle, with the two side spars inserted into a plastic connection piece to allow for attachment to the servo. The Mylar-based foil is securely wrapped around the carbon fiber rods and adhered to itself using heat, while the carbon fiber rods are attached to the servo connection with an adhesive. The original tail design had only one plastic piece connecting to the servo [46]. This design allowed for a large amount of flexion in the tail, which negatively affected steering. The tail was therefore reconfigured, doubling the thickness of the plastic connector, which provided for much more stiffness and hence, improved steering capabilities. The modified tail is shown in Figure 21.
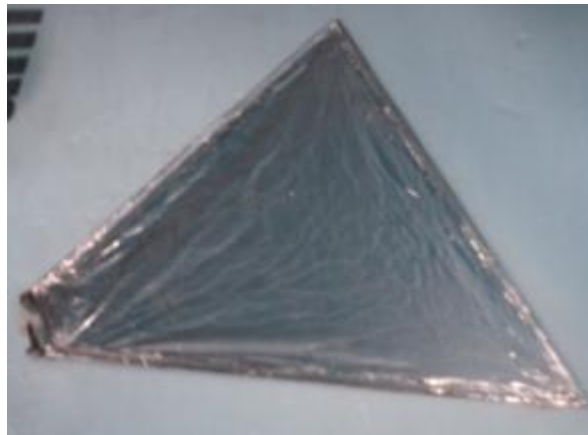
Figure 21 Modified tail design

3.3   *Flapping Mechanism*

3.3.1   Original Compliant Mechanism

The original compliant mechanism was the as the mechanism used on the University of Maryland Big Bird, shown in. It was a single-material compliant crank mechanism made in the Advanced Manufacturing Lab using the CNC milling machine. While this mechanism was successful in generating enough flapping force to fly, the reaction forces were great enough to cause a significant amount of sway in the mechanism. Due to this sway and the difficulty of mass-production of this mechanism, a new mechanism design was developed.
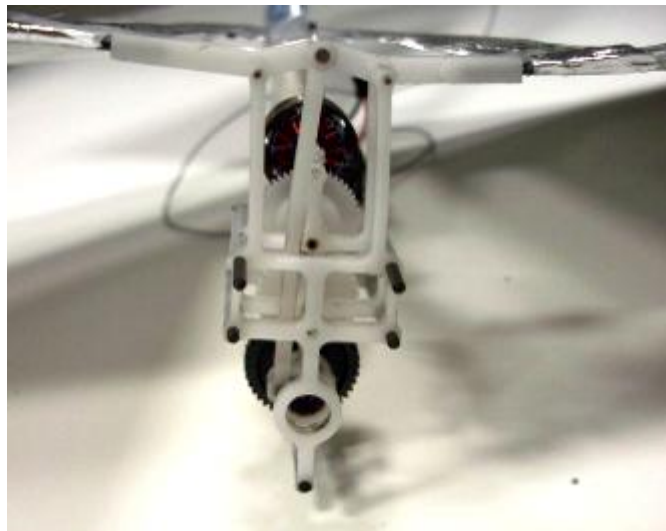
Figure 22 Original compliant mechanism design [12]

3.3.2 Redesigned Compliant Mechanism

The newly designed compliant mechanism was manufactured in the Advanced Manufacturing Lab at the University of Maryland [43, 49]. This mechanism, seen in Figure 23, was made using in-mold assembly methods and contained multiple compliant joints, which allowed for more flexion and reduction of backlash friction. Additionally, a slider-pin joint was introduced to eliminate the sway present in the original mechanism. The remaining joints were designed as rigid body articulating joints to ensure more reliable testing during wing characterization.
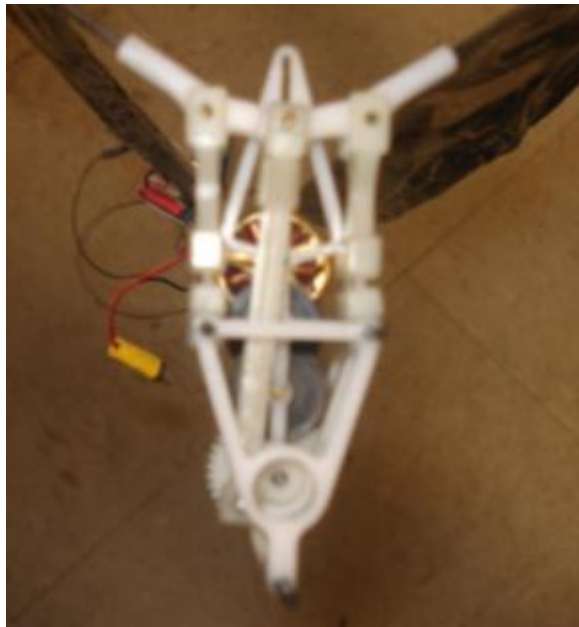
Figure 23 New compliant mechanism design [43]

3.4   Testing Setup

Since the existing computational models are inadequate for determining the wing forces in compliant flapping wings, the direct measurement of forces in the wings during the flapping cycle was selected as the method for gaining insight into the wing design

parameters. Lift and thrust measurements for compliant flapping wings were obtained through a combination of a test stand with a load cell and an air bearing, as well as the post-processing software [43]. In addition to lift and thrust data, high-speed imaging was used to develop an image representation of the wing at different points throughout the flapping cycle, assisting in the description of the wing movement.

3.4.1 Test Stand and Equipment

The test stand used to evaluate the relative lift and thrust forces for the MAV was comprised of a transducer, an air bearing system, a breadboard with four rubber mounts, and a CNC-machined test fixture to hold the MAV in place during testing. The transducer, an LCFD-1KG miniature load cell, seen in Figure 24, converted the loads generated by the wing flapping into a voltage signal for processing. With its 1000-gram capacity and precision of 1.5 grams, this load cell was selected based on its high frequency resonant characteristics, minimal contamination from off-axis loads, and impressive overloading tolerances [43].

Figure 24 Omega Engineering, Inc. LCFD-1KG miniature load cell [50]

The load cell was mounted on a RABIS linear air bearing system, seen in Figure 25, to minimize friction and stiction caused by the off-axis loads generated during flapping. The bearing system had an inner slider bar that slides along a single axis inside the outer housing on a cushion of air provided by a pressurized air supply to eliminate friction in the bearing. Because the mounting system aligned the air bearing axis of motion with the axis of the load cell, the lift and thrust forces were sufficiently isolated from any external signals [43].
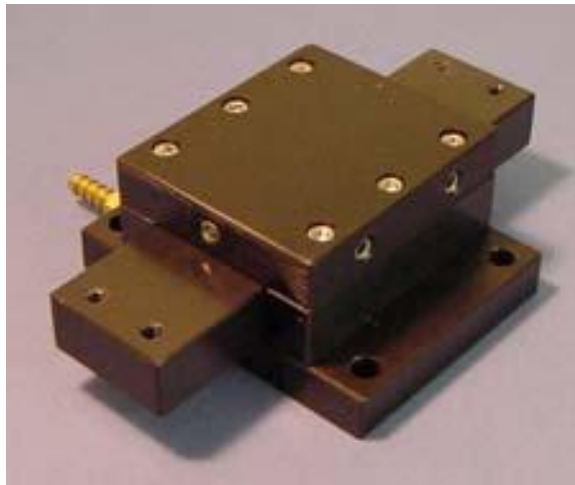
Figure 25 Nelson Air Corporation RABIS linear air bearing [43]

The bearing system and load cell were securely mounted on a solid aluminum Newport Optics SA breadboard, seen in Figure 26. The platform had considerable mass, providing a stable platform for testing.

Figure 26 Newport Corporation SA2 aluminum optics breadboard

On the four corners of the breadboard, four hemispheric Edmund Optics Sorbothane mounts were attached, as seen in Figure 27. Because the mounts were made of a polymer material that provides 57% absorption of energy and 70% specific damping, they provided additional isolation from any noise contaminating the measurement signal, originating from the testing surface vibration or the surrounding environment [51].

Figure 27 Edmund Optics Sorbothane polymer mounts [51]

The last piece of equipment within the test stand was the CNC-machined mounting fixture, used to attach the MAV to the test stand. Because the load cell and the air bearing were configured to operate on a single axis, the mounting fixture was

designed to be configured for both lift and thrust modes. The mounting fixture in thrust

mode can be seen in Figure 28.

Figure 28 Mounting fixture with MAV configured in thrust mode

In this configuration, two mounting posts held the MAV clamping fixture at the

appropriate angle of attack. The mounting posts were machined for a tight fit of both the

air bearing and the MAV clamping fixture, ensuring the MAV remains securely in place.

For lift measurement, the MAV was oriented such that the moving airstream can be used

to measure the lift forces. In this orientation, the clamping fixture was attached directly

to the two holes in the end of the slider bar of the air bearing system using two screws, as

seen in Figure 29.

Figure 29 Mounting fixture with MAV configured in lift mode

3.4.2 Wind Tunnel

The test stand described in the previous section was sufficient to measure the static forces; however, the measurement of lift forces required a moving airstream. The thrust was calculated using non-moving air, because the flapping motion of the flexible wings was sufficient to generate the thrust forces. Lift, however, is the force that develops when the aerofoil shape created by flapping motion is placed in a moving airstream, allowing for flight [46]. The wind tunnel, shown in Figure 30, is a common method used to generate a moving airstream. Wind tunnels are generally designed in a specific manner to produce a highly laminar and smooth airstream. Since the tested MAV was relatively small and the desired results required the replication of real-world flight conditions, a somewhat turbulent airstream was desired [46]. The wind tunnel consisted of five interlocking three-foot square foam sections, each four feet in length, resulting in an overall length of 20 feet. The test stand was placed on a table within the front section, with a large fan placed at the end of the tunnel to generate the airstream.

Figure 30 Tunnel used for lift testing of the MAV [43]

3.4.3 High Speed Imaging

In order to develop a better understanding of how aerodynamic loading affects the deformation of the wings on flapping-wing MAVs, high-speed imaging was used to capture the images of the wings at different points during the flap cycle. Using a high-speed camera at a fixed distance from the MAV, images were taken both from the head-on and over-top angles to describe the deformation of the wings. The Casio Exilim EX-F1 high-speed camera was used, capable of high-speed video capturing at 300 frames per second. High-speed imaging was a crucial part of the wing characterization discussed in the latter sections.

3.5 Summary

In this chapter, the 'Jumbo Bird' MAV platform was presented and its components were described. The testing equipment, including the test stand, the wind tunnel, and the high-speed camera were introduced. While the majority of this chapter was based on previous work, several new developments in both the MAV platform and the testing equipment have been made for this thesis. The body was redesigned to significantly increase stiffness, and the tail attachments were improved to reduce the flexibility and improve the turning abilities. The mechanism was introduced with compliant hinges to increase the efficiency, and the slider-pin joint to eliminate the sway during the flap cycle. Due to the new body, the mounting fixture for the test stand had to be redesigned to provide a tight fit and allow for an easy switch between lift and thrust modes. This was achieved by reducing the number of parts in the fixture assembly, which resulted in much improved rigidity of the setup. Thus, the contributions of this thesis include the new body design, the new tail attachment, a new compliant mechanism design, and the new mounting fixture.

Chapter 4:   Wing Characterization

As seen in the literature review in Chapter 2, there are many types of flapping wings used in MAVs, but very little is known about the forces acting on the wings, and how they deform throughout their respective flapping cycles. Because so little is known, it is hard to accurately analyze different wing designs to improve their performance. This chapter develops a method of wing characterization that combines leading spar motion, deformation measurement, centroid and volume calculation, and calcualted and measured image generation to understand how flexible flapping wings move throughout the flap cycle, and provide an explanation of the lift and thrust forces generated when flapped the wings are flapped.

4.1   Previous Methods

In his thesis, John Gerdes developed six different wing designs and performed lift and thrust measurements as described in chapter 3. His results are shown in Figure 31. From this figure and actual flight-testing, he determined that wing F was the best performing wing; however, there was no method for explaining why the results were obtained other than using the actual flight-testing.
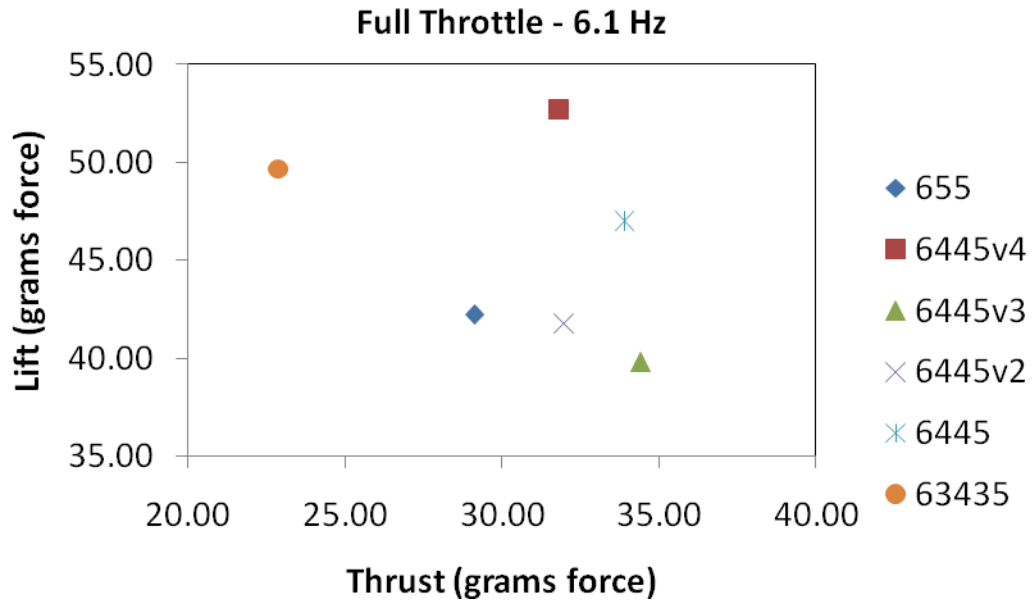
Figure 31 Previous lift and thrust results for six wing designs [43]

In order to explain the results, Gerdes measured the deflections of the Mylar-based films at the centroid for each wing, which was located 4.45 inches from the wing root, using high-speed imaging [43]. These deflections for the up-flap and the down-flap can be seen in Figure 32.
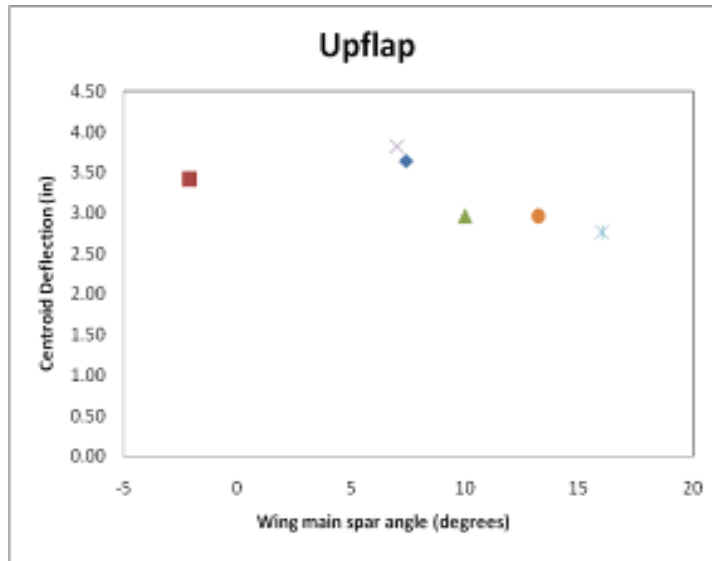
(a)
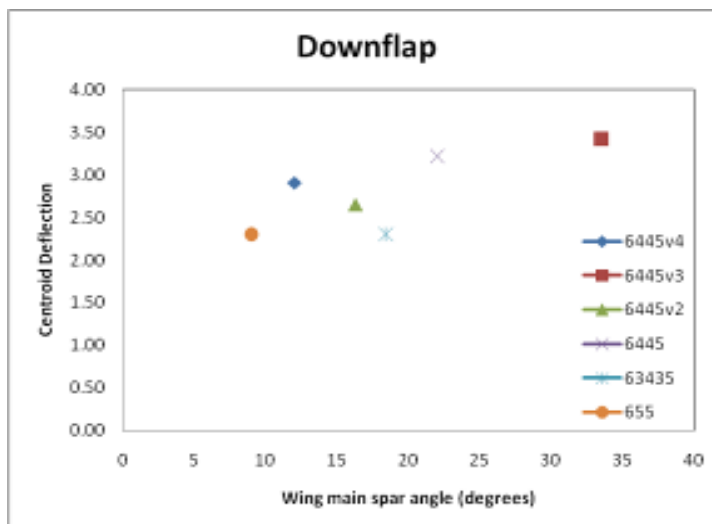
(b)

Figure 32 Centroid deflections for wing designs [43]

He saw that during the up-flap, the sooner that a greater deflection was reached (meaning that the largest deflection occurred at a smaller angle), and the better the performance of the wing because a larger air flow rate was achieved. Similarly, he noticed that during the down-flap, the sooner a greater deflection was reached (the largest

deflection occurred at a larger angle), the better the performance of the wing. He concluded that wings with effective stiffness distributions exhibited larger centroid deflections earlier in the flapping cycle, and thus had an increased amount of time for useful force production [43]. These results were combined with the span-wise location of the peak deflection exhibited by each wing, seen in Figure 33. Gerdes claimed that if the peak deflection was close to the centroid and maximized, the overall performance of the wing would be maximized because the thrust was aimed parallel to the flight path; if the peak deflection was further out on the span, air was escaping laterally instead of being directed backward, reducing thrust forces generated [43]. So, in Figure 33, the best performing wing would fall in the upper-left quadrant; wing F did fall up and to the left, supporting his claim.
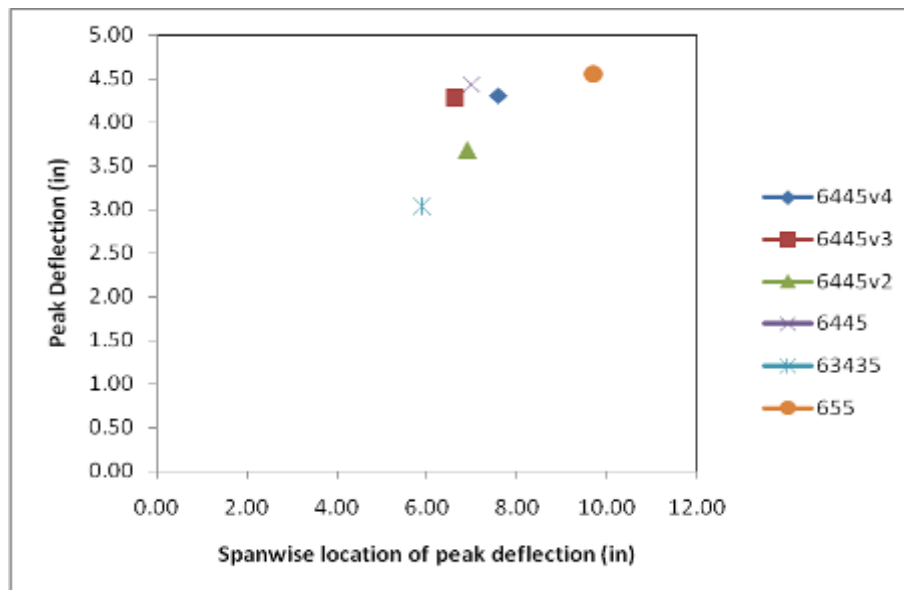

Figure 33 Peak Deflection vs. Location for wing designs [43]

While the data and explanation provided by Gerdes explained his results, additional data and imaging would present a more thorough picture of the wings to support the claims made. This chapter provides a thorough method for characterizing how flexible flapping wings deform and move throughout their flapping cycle.

4.2 Data Collection

In order to better illustrate how the wings moved throughout the flap cycle, data was collected to describe the movements of the front spar, the blowback effects, and the lift and thrust forces for the wings. High-speed video was used to capture images of the wings at different frames and angles during the flap cycle. Each cycle, when filmed using the high-speed camera described in chapter 3, consisted of forty-five frames, thus, fifteen evenly spaced frames from each flap cycle were used in creating wing plots. The plots shown from the data collected contain fifteen plots for this reason.

4.2.1 Front Spar Displacement

Throughout the wing cycle, there are a few different parts that affect how the wing develops, one of which is the motion of the front spar. Using high-speed imaging, the movement of the front spar was tracked throughout the flap cycle, from both the head-on perspective, seen in Figure 34, and the over-top perspective, seen in Figure 35. The displacement was calculated by determining where the fixed wing location would have been if the wing was perfectly stiff, and measuring the distance between its fixed wing location and its actual location. The measurement was made using image analysis software on each of the fifteen evenly spaced frames for each of the six different wing

types.   This measurement was used to calculate both the head-on and over-top displacement of the front spar.
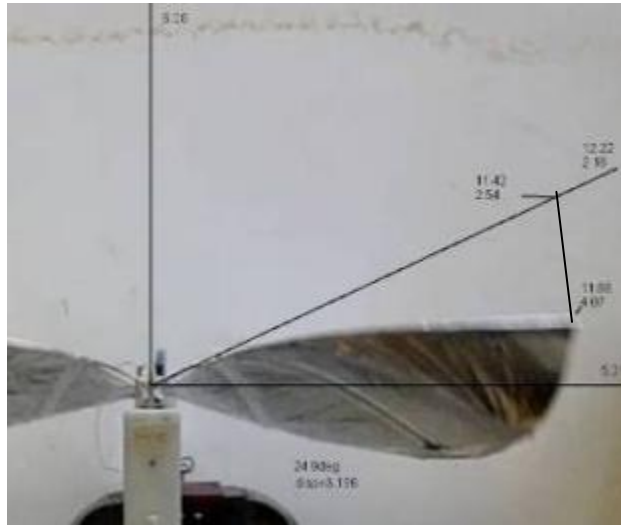
Figure 34 Head-on perspective for front spar displacement

Figure 35 Over-top perspective for front spar displacement

Plots comparing the front spar displacement for both the over-top and head-on perspectives can be seen in Figure 36 and Figure 37, respectfully. The ideal paths of the front spar for both perspectives were illustrated using thick black lines; from the over top perspective, the front spar should move away from the center line towards the rear of the wing during the up-flap, snap forward of the center line during the transition between the up-flap and the down-flap, and then move away from the center line towards the rear of the wing once again during the down-flap as the wing fills up with air and deforms, snapping back to zero at the transition. From observing the plot of the front spar paths in Figure 36, it was obvious that the wing F best followed the ideal path, allowing the wing to collect the most useful amount of air and expel it in the most efficient way. Wings A and D followed the ideal path the least accurately, which reflected their generation of smaller lift and thrust forces.
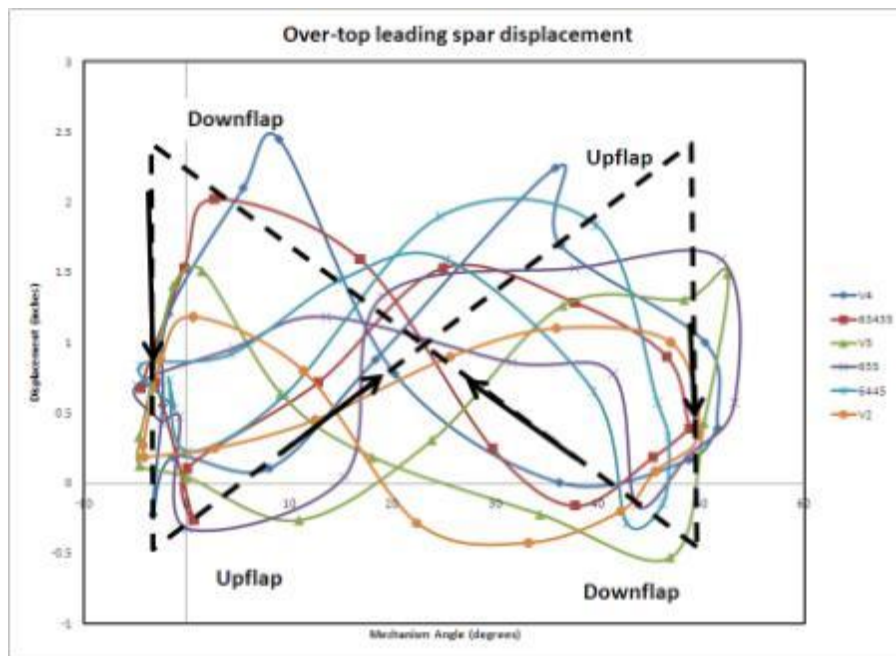
Figure 36 Over-top leading spar displacement

The ideal path for the leading spar from the head-on perspective resembles a parallelogram; the leading spar trails the ideal spar location during the up-flap so the displacement is negative, crosses over the ideal location during the transition between up and down flaps, and then trails the idea spar location during the down flap, resulting in positive displacement. As seen in Figure 37, all of the wing constructions followed the ideal leading spar path in approximately the same manner; this reflected the fact that the wings are all constructed with the same leading spar thickness, 0.06" carbon fiber.
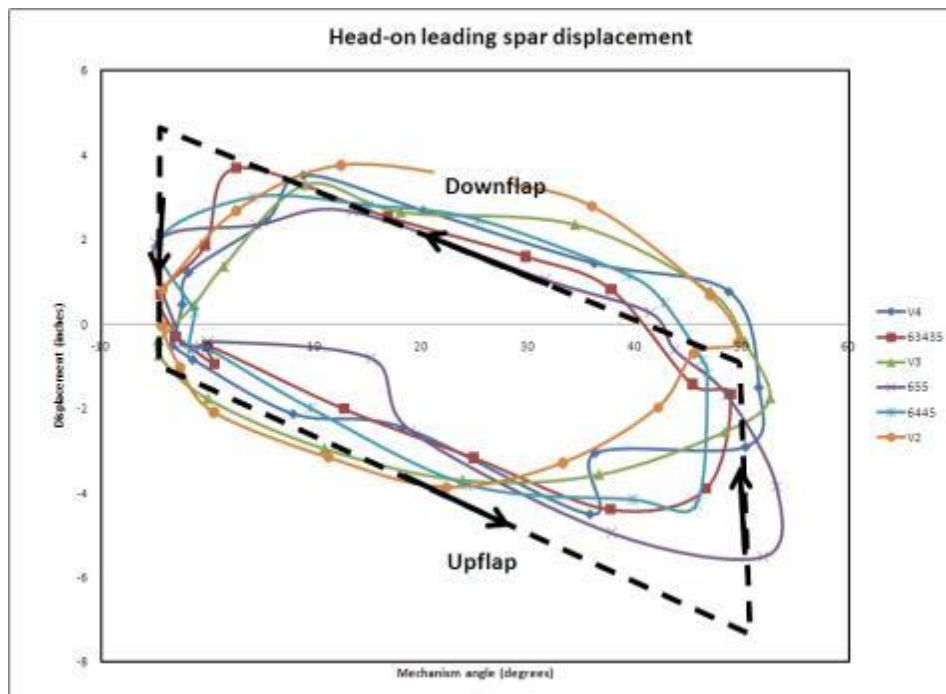

Figure 37 Head-on leading spar displacement

The displacement of the leading spar, from both the head-on and over-top perspectives, indicated the direction in which the spar moved during the up-flap and down-flap of the flapping cycle. This improved the understanding of wing shape during the cycle and how that shape affected the lift and thrust forces generated during flight

because it defined the location of the front edge of the wing at fifteen different points throughout the flap cycle.

4.2.2   Blowback Characterization

While the motion of the front spar did impact how the wing captures air and deforms throughout the flap cycle, the motion of the Mylar-based wing film covering the carbon fiber spars has a much larger affect on the amount of air captured and how that air is displaced to generate lift and thrust. The deformation of the Mylar-based film and carbon fiber spars is known as blowback, because the air forces the wing film to move away from the connecting spars at the leading and center edges. To capture this blowback effect, each of the six wing designs was manufactured out of Mylar-based film with a black external coating. Then, a two by four grid was marked on the wing using white out tape. This stark contrast of black and white allows for the squares to be easily captured in images taken by a high-speed camera. The use of grid squares divided the area of the wing into eight smaller parts, allowing for the changes in each square to be tracked and the results summed, determining the changes for the entire wing. This process provided greater accuracy in the calculations than previous methods, which simply looked at images of the whole wing and made assumptions based on the perceived shapes. The grid squares were labeled as seen in Figure 38, allowing for easy identification of the squares when processing the data collected.

Figure 38 Image of wing with blowback grids marked and labeled

Using image-processing software, lengths along the leading spar and perpendicular to the leading spar of each of the squares were measured, and the length changes calculated by subtracting the measured length from the original lengths of each grid square; the greater the length change, the greater the change in overall deformation in the grid square. Only the left wing of each wing set was measured, based on the assumption that the left and right wings were manufactured in an identical fashion and that both wings flapped in an identical manner. Based on the wing construction, the length changes were greater in grids 3, 4, 7, and 8, since these grids were further away from the leading and center edge spars; this also indicates that the outer locations in the wings captured a greater amount of air during the flap cycle and thus had a greater influence on flight performance. A comparison of the length change parallel to the leading spar for grid square three between the different wing constructions is seen in Figure 39. From this plot, it is obvious that the greatest deformations for the wings occurred at the end of the up-flap, with the direction switching during the transition

between up and down flaps and an equal magnitude being reached at the start of the down-flap; this reflects the fact that the majority of the air is captured at the start of the down-flap during the flap cycle.
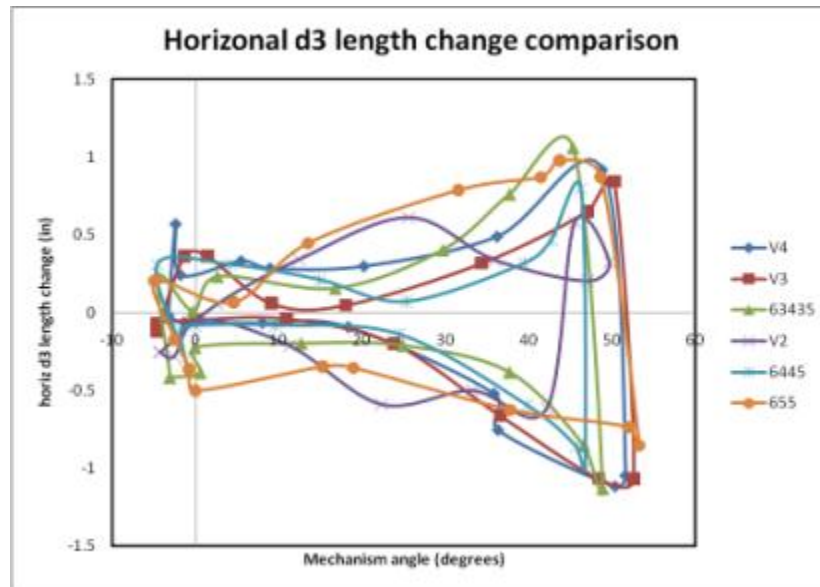
Figure 39 Length change comparison of horizontal length of grid 3 between wings

4.2.3   Lift and Thrust Measurement Verification

A good combination of lift and thrust values are necessary to achieve successful flight. The best performing wings have large lift and thrust values; in a lift vs. thrust plot, the most successful wings fall in the upper right quadrant. While lift and thrust measurements for the 6 wing constructions described in chapter 3 were determined in previous work, the method was not verified to be accurate, and the wings were being tested using a new mechanism, body design, and test stand clamp. Using the methods described in chapter 3, the same six wing configurations were tested in both lift and thrust modes in the wind tunnel and the results collected using the same data collection

software. When compared with the results seen in Figure 31, the lift and thrust results found in Figure 40 were very similar, validating the results found in previous work. As found in previous work, wing F performed the best, maximizing lift and thrust, while wings A, B, and D performed the worst, with low values of lift and/or thrust.
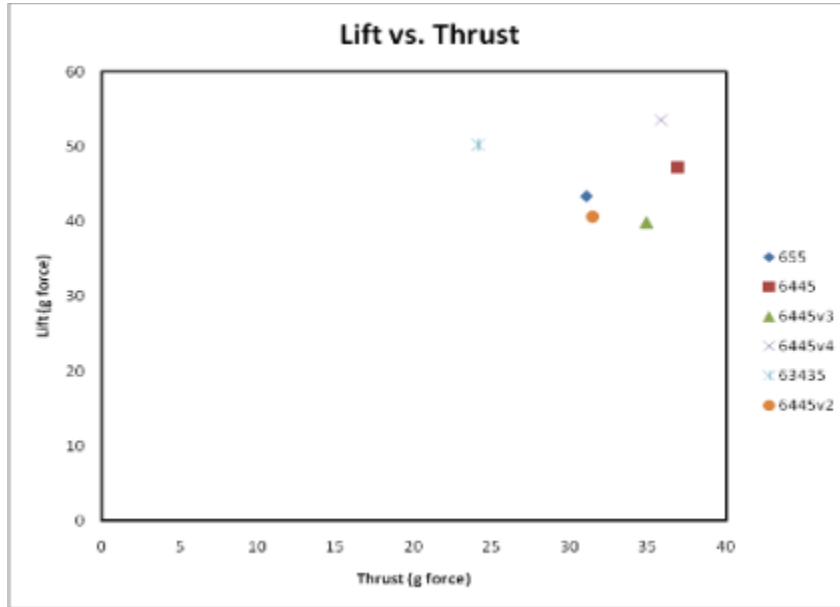
Figure 40 Lift vs. Thrust values for the six wing configurations

4.3   Centroid Calculation

4.3.1   Motivation

While the movement of the leading spar and the length change of the grid squares on the Mylar-based film gives an idea of the deformations that occur and begin to paint a picture of wing motion throughout the flap cycle, further calculations and imaging are needed to fully characterize the wing shape during flapping motion. Calculation of the centroid of the wing at different points during the flap cycle shows how the area of the

wing surface has changed from its original shape, and thus further defines how the wing film moves throughout the flap cycle.

4.3.2   Description

The centroid of each wing was calculated by summing the centroids of each of the eight grid squares, which were calculated using the length changes measured from the high-speed images taken for each of the different wing constructions.   In order to calculate the centroid for each of the grid squares, an origin point was selected on the point of the wing closest to the mechanism angle and center points were selected in each of the grid squares. These points can be seen in Figure 41; the origin point is red while the center points for the grid squares are white.
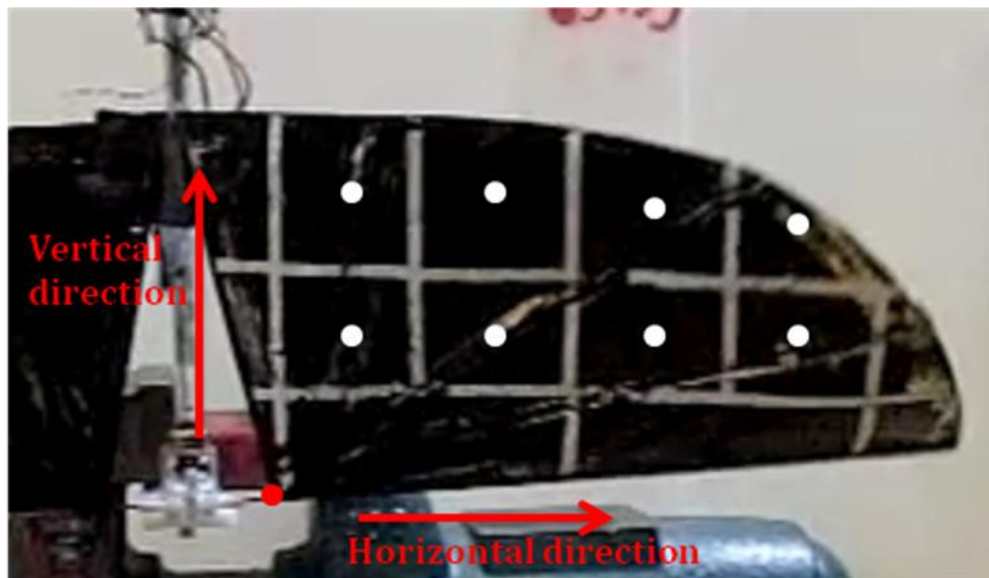

Figure 41 Centroid approximations and definition of directions

The definitions of horizontal and vertical directions are also indicated in the above figure.   Horizontal is defined as along the leading spar, while vertical is defined as

60

perpendicular to the leading spar. Both directions must be consideredk since the centroid location varies along the spar. The centroid location is a measurement of distance, calculated by multiplying the length change by the area of the grid square by the distance from the origin to the center point of that grid square and summing this for each of the grid squares, and then dividing by the summation of the length change multiplied the area of each grid square. The equation used is seen below.

$$centroid = \frac{\sum_{i=1}^{8} a_i A_i x_i}{\sum_{i=1}^{8} a_i A_i}$$

a= value of length change
A= area of grid square
x= distance from selected point on wing to center point in grid square

EQ.1

Centroids both along and perpendicular to the leading spar were calculated using the above equation for each set of wings, and the values were compared to determine how the movement of the centroid location affected lift and thrust values for each wing type.

4.3.3 Perspective Correction

Upon further examination of the image collection technique and the resulting data, it was observed that the method of collection did not take into account the change in perspective within the images taken at different points of the flap cycle. Because the camera stayed at a fixed distance from the wing, and the wing moved toward the camera as it reached the upper angles of the up-flap and away from the camera at the bottom of its down-flap, the perspective for the image at each angle during the flap cycle was slightly different. To correct for this perspective discrepancy, images were taken of the

stiff wing at eleven evenly spaced angles throughout the flap cycle, which ranges from five to 50°. The changes in vertical and horizontal lengths for the stiff wing were calculated relative to the lengths at the 0° mechanism angle, and a line of best fit was found. Because the perspective change only affected the vertical lengths one-dimensionally as the wing moved closer to the camera, the fit was linear, as seen in Figure 42.
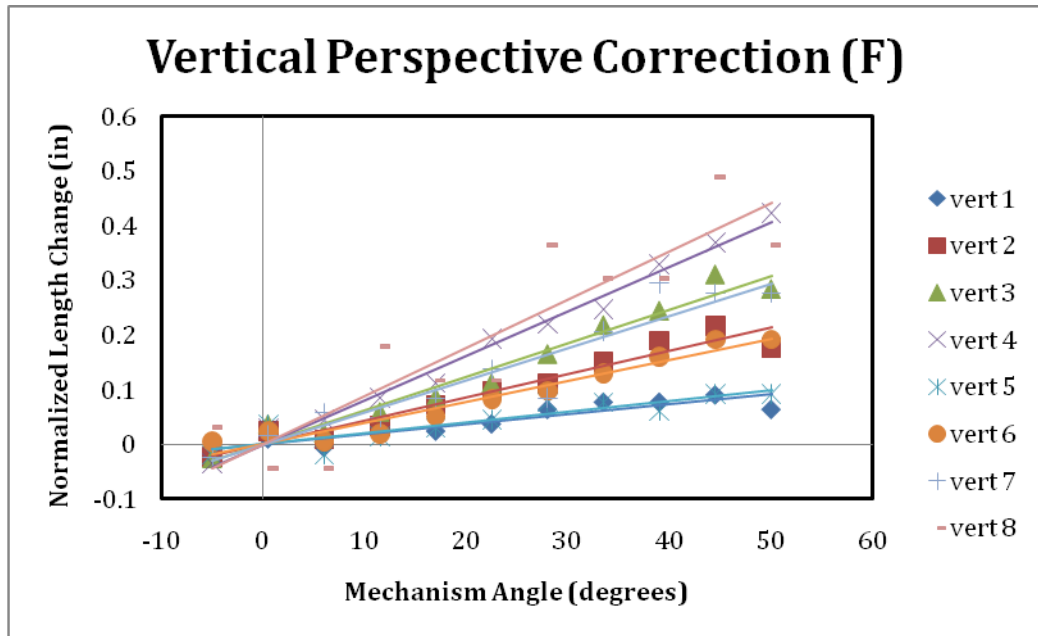

Figure 42 Perspective correction for vertical lengths of wing F

The horizontal lengths, however, were affected by the perspective change in two dimensions; one dimension as the wing moved closer to the camera, and the second as the wing rotated through the mechanism angle. The resulting best-fit line was a second-degree polynomial, as seen in Figure 43.
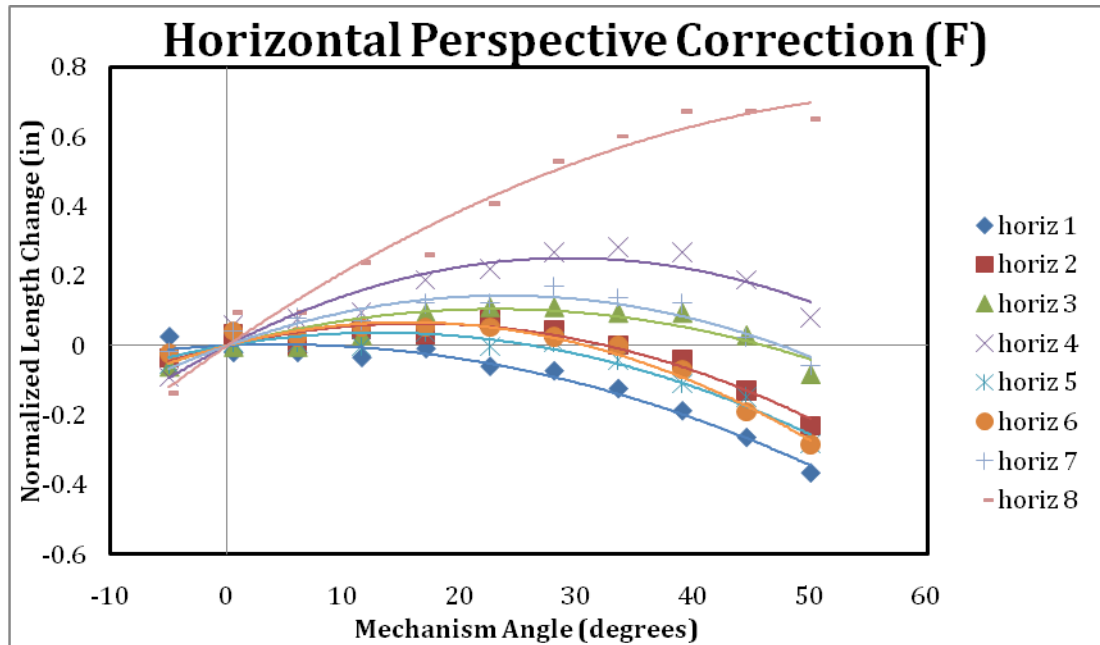
Figure 43 Perspective correction for the horizontal lengths of Wing F

The equations for each of the lengths were then used to determine what the horizontal and vertical lengths of each grid square were for a completely rigid wing at every angle during the flap cycle, giving a more accurate value for the length change calculated. Now, the length change was calculated to be the difference between the length measured in the image at an angle and the length of the grid if the wing were completely rigid at that same angle, instead of the difference between the measured length and the original flat length of the grid.

4.3.4 Results

The perspective corrections were made for each wing construction and the centroids were normalized based on the original wing centroid values. The resulting horizontal and vertical centroid plots as the wings move through the flap cycle can be seen in Figure 44 and Figure 45, respectively.
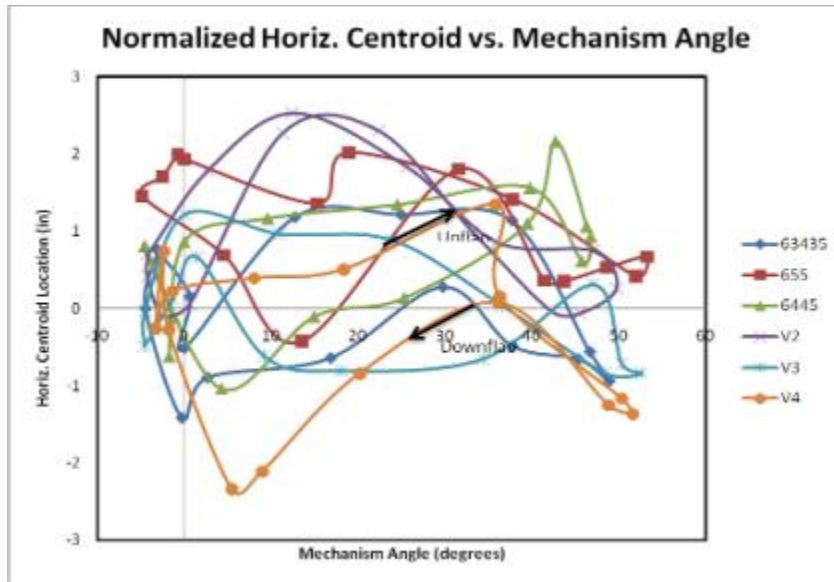
63

Figure 44 Normalized horizontal centroid location versus mechanism angle
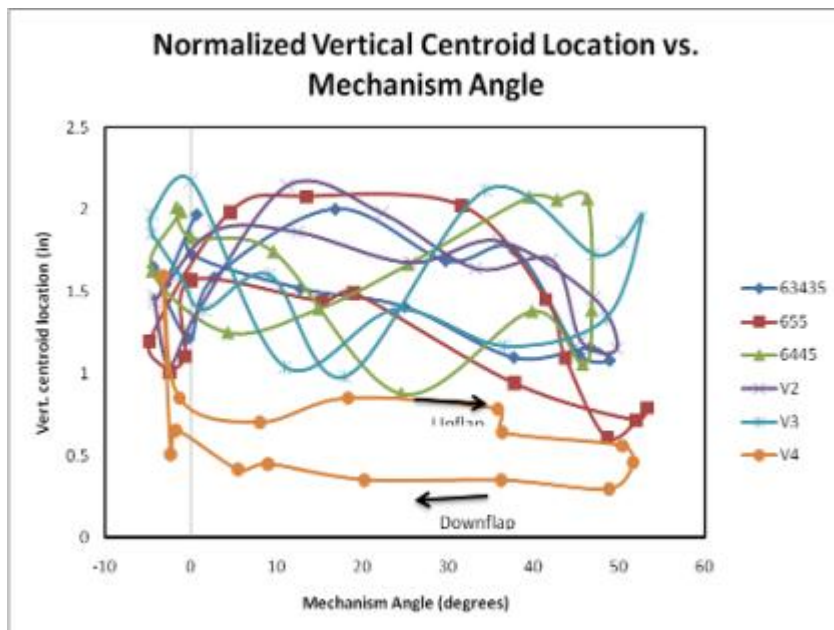

Figure 45 Normalized vertical centroid location versus mechanism angle

The ideal centroid values would move away from the leading spar for the vertical

values and away from the center spar for the horizontal values during the up-flap and

towards the leading spar for the vertical values and towards the center spar for the horizontal values during the down-flap. For both the horizontal and vertical centroid locations, wing F most closely approximates these ideal values, while wings A and D least closely approximate these values.

4.3.5   Summary

The centroid calculation allows for a better idea of wing motion throughout the flap cycle to be generated by showing how the area of the wing surface moves between different points in the flap cycle. Because the centroid location reflects how the surface area of the wing film changes throughout the flap cycle, it helps describe how the wing film deforms at different points.   Once the issue with the image perspective was identified and corrected, the horizontal and centroid values help provide explanation as to why the different wing constructions have different lift and thrust values; shifts in the centroid, both horizontally and vertically, change the effectiveness of the wing area in moving air to generate lift and thrust. Each of the different wings exhibited different movements of the centroid, and thus perform differently.

4.4   Volume Calculation

4.4.1   Motivation

While the combination of the leading spar movements, blowback approximations through grid square length changes, and the addition of centroid location movement throughout the flap cycle continue to improve the characterization of wing deformation during flapping motion, the addition of a calculation of the volume of the area under the wing film would improve the understanding of how the wing deforms during flapping.

By comparing the volume under the wing film at different angles during the flap cycle, the amount of air captured and displaced at different times can be determined and used to explain the measured lift and thrust forces for the wing. Also, the volumes of different wings at the same point in the flap cycle can be compared to better understand how certain wing configurations result in better overall performance.

4.4.2   Theoretical Volume Calculation

In order to ensure that the volume calculation used provides an accurate approximation of the volume under the wing, a theoretical volume calculation was done to validate the equation. A rectangular piece of Mylar-based film with a marked grid was taped to a surface and deflected one inch at the center point, as seen in Figure 46.

Figure 46 Mylar-based film with grid deflected one inch to verify volume equation

Because the area of the square and the deflection were both known, the volume was calculated to be 17.4125 in^3 using equation 2.

$$V_t = \frac{d \cdot A_0}{3} = \frac{(1) \cdot (52.2375)}{3} = 17.4125 \qquad \text{EQ.2}$$

The horizontal and vertical lengths of the grids in the deflected film were calculated using geometry, since the shape of the deflected film, a pyramid, is known. Because the original horizontal and vertical lengths as well as the areas of the grid square were known, the volume was calculated to be 14.70065 in^3 using equation 3.

$$V_t = \sum_{i=1}^{8} \left(lx_{oi} \sin\left(\cos^{-1}\left(\frac{lx_{fi}}{lx_{oi}} \right) \right) + ly_{oi} \sin\left(\cos^{-1}\left(\frac{ly_{fi}}{ly_{oi}} \right) \right) \right) \cdot \frac{A_i}{3} = 14.70065 \, (15.57\%) \quad \text{EQ.3}$$

This volume was a 15% change from the theoretical volume expected; because it was under 20% and also less than the expected volume, the equation was then used with length changes determined using measured horizontal and vertical values from image analysis software. The resulting calculated volume was 26.001 in^3, seen in equation 4.

$$V_c = \sum_{i=1}^{8} \left(lx_{oi} \sin\left(\cos^{-1}\left(\frac{lx_{fi}}{lx_{oi}} \right) \right) + ly_{oi} \sin\left(\cos^{-1}\left(\frac{ly_{fi}}{ly_{oi}} \right) \right) \right) \cdot \frac{A_i}{3} = 26.001 \, (49.32\%) \quad \text{EQ.4}$$

This value was 50% greater than the theoretical value for volume; this change was much too great to be acceptable. The first difference between the theoretical volumes was reasonably small; however, when the selected equation produces a 50% increase in volume, the equation needs to be re-evaluated.

4.4.3   Bi-Linear Interpolation Method

Since the original equation did not accurately approximate the values of volume under the wings, a new method had to be developed to calculate volume. The next method of calculating volume used was the bi-linear interpolation method. In this

method, deformations of each point are calculated using changes in length, and volume is calculated using deformation matrices made from the x and y locations of each grid square. These locations were determined using the horizontal and vertical lengths that were measured for each grid square. Figure 47 demonstrates the location of the deformation points below.
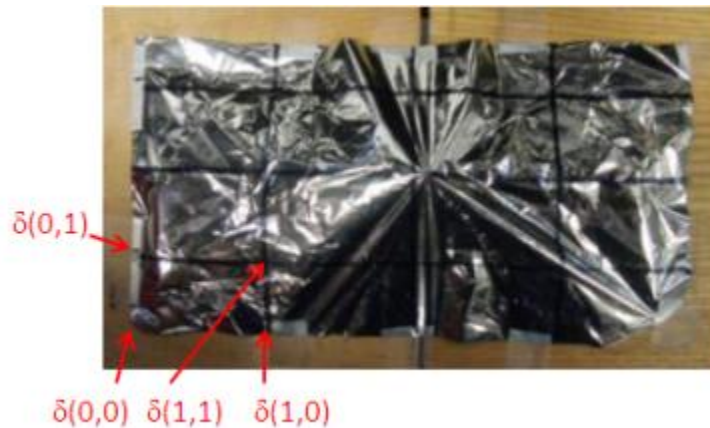

Figure 47 Bi-linear interpolation deformation point definitions

Using the following equations, the changes in length were used as the deformations, and the x and y locations made up the matrix for each grid square. The constants were then solved for, and the constants were multiplied with the x and y lengths for each grid square as described in equation. Based on the volume equation, seen in equation 6, the volume underneath the square was calculated for each grid square. The volumes were then summed to calculate the total volume for the entire area.

$$\begin{Bmatrix} \delta(0,0) \\ \delta(0,1) \\ \delta(1,0) \\ \delta(1,1) \end{Bmatrix} = \begin{bmatrix} x_{00} & y_{00} & x_{00}y_{00} & 1 \\ x_{01} & y_{01} & x_{01}y_{01} & 1 \\ x_{10} & y_{10} & x_{10}y_{10} & 1 \\ x_{11} & y_{11} & x_{11}y_{11} & 1 \end{bmatrix} \begin{Bmatrix} a_0 \\ b_0 \\ c_0 \\ d_0 \end{Bmatrix}$$
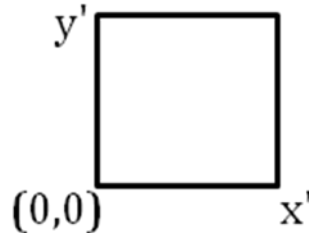
EQ.5

$$\delta(1,1) = \delta(0,1) + \delta(1,0)$$

$$\delta(x,y) = a_0 x + b_0 y + c_0 xy + d_0$$

$$volume_i = \int_0^{x_i'} \int_0^{y_i'} \delta(x_i, y_i) dA_i$$

$$= \frac{y_i' a_{0i} x_i'^2}{2} + \frac{x_i' b_{0i} y_i'^2}{2} + \frac{c_{0i} x_i'^2 y_i'^2}{4} + d_{0i} x_i' y_i'$$

$$total\ volume = \sum_{i=1}^{8} volume_i$$

EQ.6

Using the bi-linear interpolation method, the theoretical volume for the square Mylar-based film was determined to be 15.733 in^3, a much closer approximation to the original theoretical volume of 17.4125 in^3 since it is only a 9.65% decrease. The calculated volume for the square Mylar-based film when using the new method was determined to be 12.587 in^3, which is a 27.7% difference from the original theoretical volume, but only a 19% difference from the bi-linear theoretical volume. Because the two values are within 20% of each other, this method was selected for calculating volume. The mesh grid images of the theoretical volume and calculated volume approximations can be seen in Figure 48 and Figure 49, respectively. The depictions are only slightly different, thus indicating that the equation for the bi-linear interpolation

method provides an accurate representation of the volume under the area of the Mylar-based film and that this method can be applied effectively to the wing grids as well.
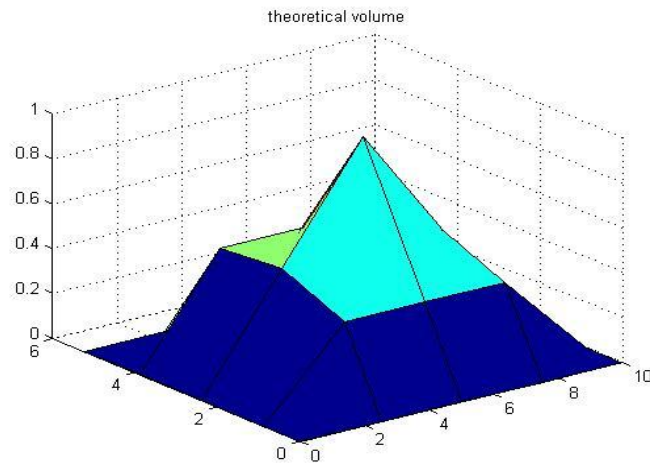

Figure 48 Theoretical volume for Mylar-based film square

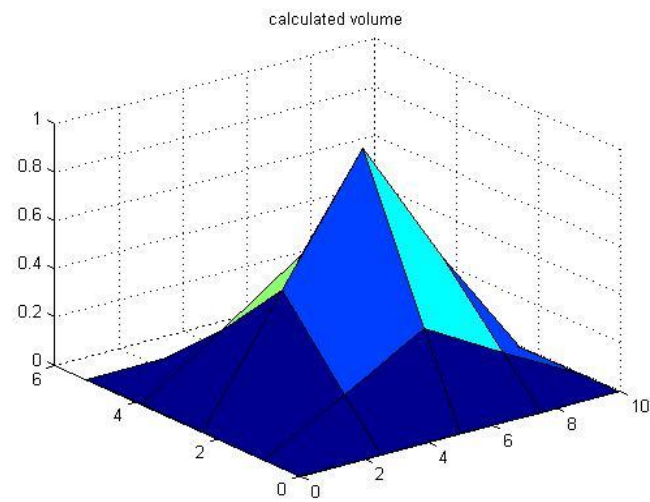Figure 49 Calculated volume for Mylar-based film square

4.4.4 Results

Using the bi-linear interpolation method equations, volumes were calculated at fifteen evenly spaced points throughout the flapping cycle for all six of the different wing

constructions. Figure 50 compares the normalized volume over the flapping cycle for all six configurations.
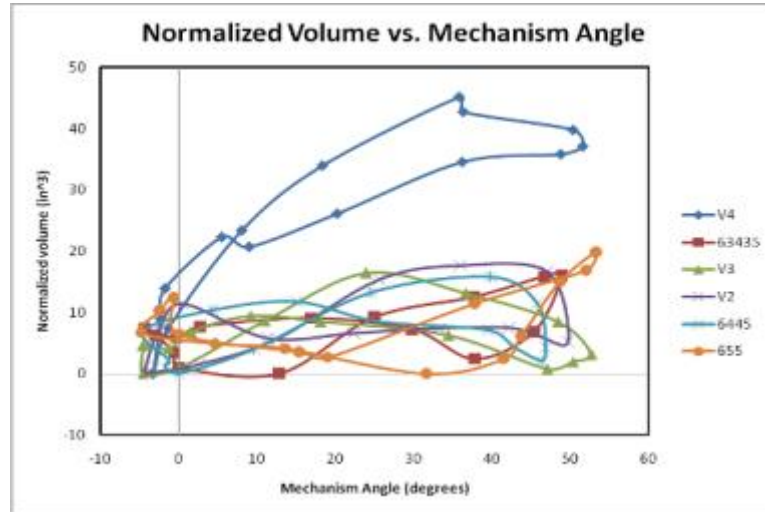

Figure 50 Normalized volume over the flapping cycle for all wing constructions

The ideal path for volume for a wing is to increase on the up-flap as the aerodynamic forces the wing to billow towards the ground, come back down through the transition between up and down-flap, and then quickly grow again as the down-flap is initiated. The volume should increase again as the wing moves through the down-flap and air is collected, to be expelled once again on the transition to the up-flap. Based on the results, it is obvious that the wing F collects significantly more volume than the other wing designs. This reinforces the fact that wing F is the top-performing wing out of the six; its lift and thrust data reflects the large amount of volume displaced by the wing design.

4.4.5 Summary

The calculation for determining the volume of air captured by the wing throughout the flap cycle is a necessary element of the wing characterization. In combination with the leading spar displacement and centroid location, it helps complete the picture describing how the wings deform and change throughout the flapping cycle. A simple geometric calculation was not enough to accurately calculate the volume under the Mylar-based film; however, the bi-linear interpolation approach was successful in accurately approximating the volume under the film. Wing F captures the most volume during the flap cycle as compared with the other wings; this reflects its overall superiority in performance.

4.5 Wing Imaging

4.5.1 Motivation

The motion of the leading spar in two planes, the variation of both the horizontal and vertical centroid locations, and the changing volume contained underneath the Mylar-based film of the wingspan, describe how the wing changes and supports the resulting lift and thrust values; however, the characterization using solely these concepts lacks a visual depiction of the wing shape at each point. Because length changes can be used to describe deformations, the deformations of each corner of the grid squares can be used to create a visual representation of the wing at each point in its flap cycle. By having a visual representation of the wing as it progresses through its flapping motion, the performance of the wing can be validated based on whether the wing shape supports the

lift and thrust forces generated. Thus, wing imaging is another element that can help characterize the performance of flexible flapping wings.

4.5.2 Calculated Imaging

The first sets of wing images generated were the calculated images. At each of the fifteen angles throughout the flap cycle, the length changes were used to calculate deformation in the z-dimension. Using the bottom left point of the first grid as the origin, the changes of the position in the z-direction of 16 points on the wing were plotted at 15 different angles in the flap cycle. The imaging was considered calculated because the x and y values were not tracked at each point; the y-values used were the original x and y-coordinates from the zero degree configuration of the wing. The resulting images for wing F can be seen in Figure 51-Figure 54, show the wing shapes at each of 15 angles based on the z-axis deformations. The volumes calculated using the bi-linear interpolation method for each of the angles are indicated in the respective figures. As the angle of the mechanism increased, the volume increased and the wing became more bowl-shaped until the mechanism reached its top angle; once the top of the flap cycle was reached, the bowl-shape of the wing was reversed, with the shape becoming less rounded as the wing returned towards the bottom of the flap cycle. The volume also decreased as the wing became less rounded, validating the accuracy of the volume equation. The shape of wing F was consistently smooth as it progressed through the 15 points in the flap cycle.
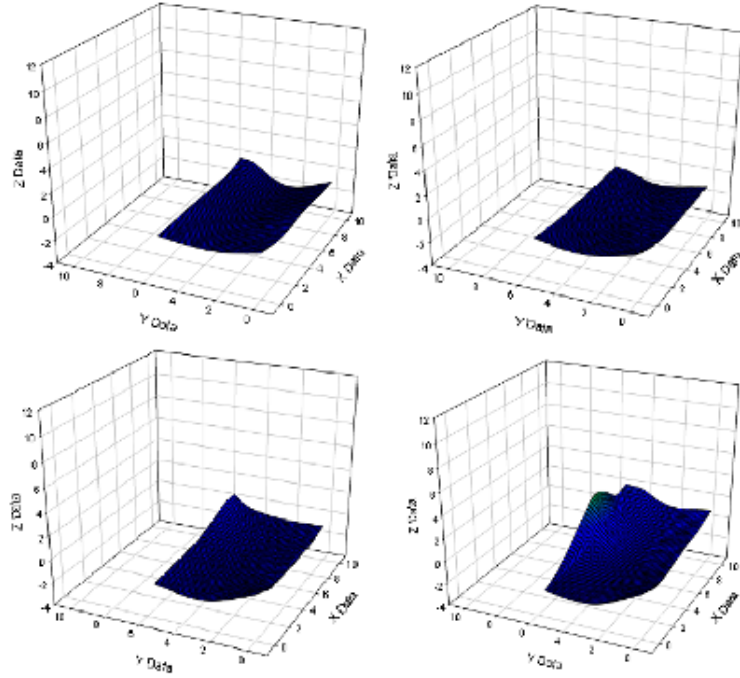
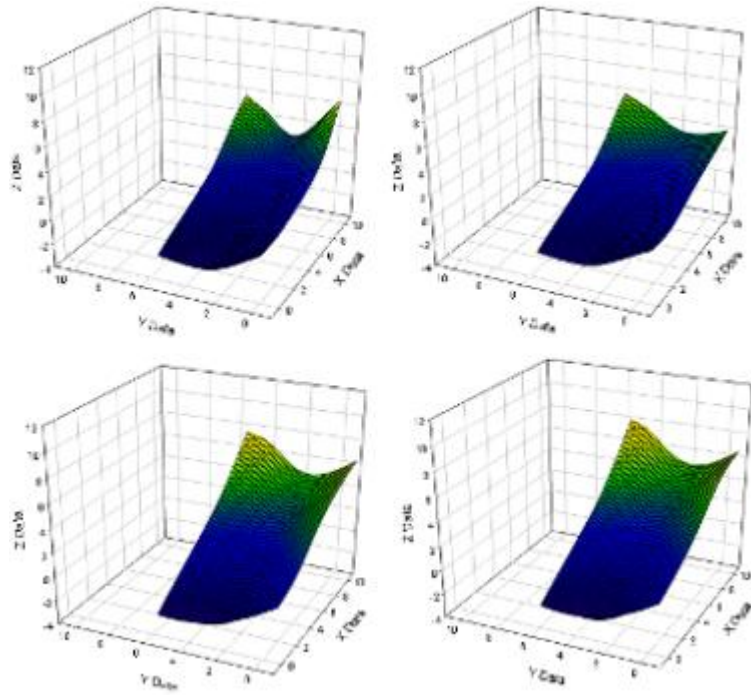Figure 51 Calculated imaging for wing F, angles 1-4

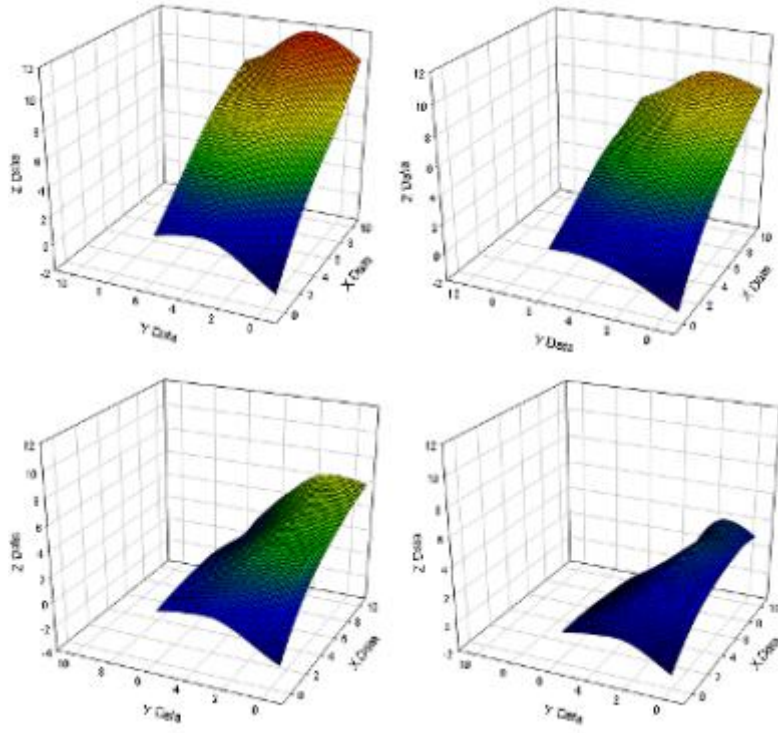Figure 52 Calculated imaging for wing F, angles 5-8

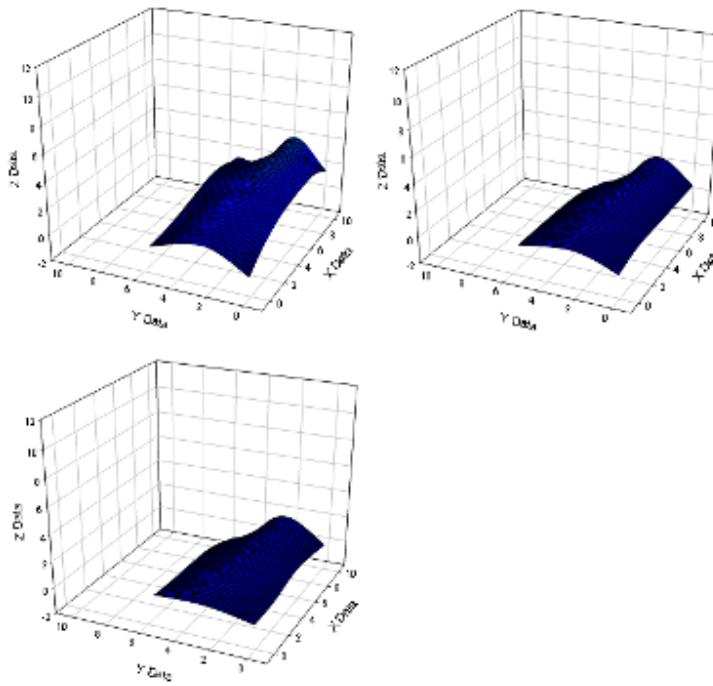Figure 53 Calculated imaging for wing F, angles 9-12

Figure 54 Calculated imaging for wing F, angles 13-15

The 15 images were generated for all six different wing constructions; the progression of the wing throughout the up-flap and down-flap for each wing design can be seen in Figure 55-Figure 60. All of the up-flap and down-flap images are on the same scale; thus, the flap cycles for each of the wing constructions can be compared. From the images, one can observe that wing F forms the smoothest shapes throughout the fifteen angles; it also captures the greatest amount of volume since its outer edge reaches the highest value in the z-axis. Wings A, D, and E all have ripples and bubbles in their shapes and do not form the smooth bowl-shape like the images of wing F. Also, wings A and C do not capture large volumes like wing F. Based on these observations and the lift and thrust values generated in section 4.2.3, the smoother the shape of the wing and the more volume captured, the better the flight performance. This reflects the lift and thrust results for the wing constructions.
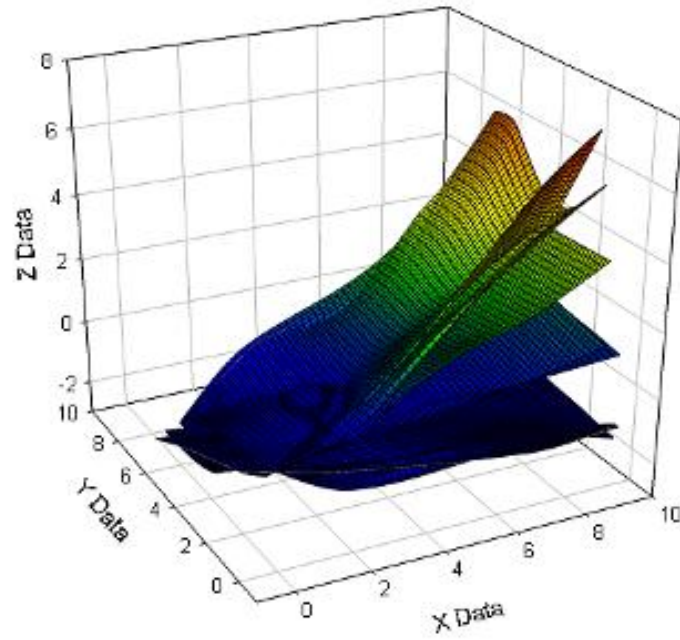
(a)
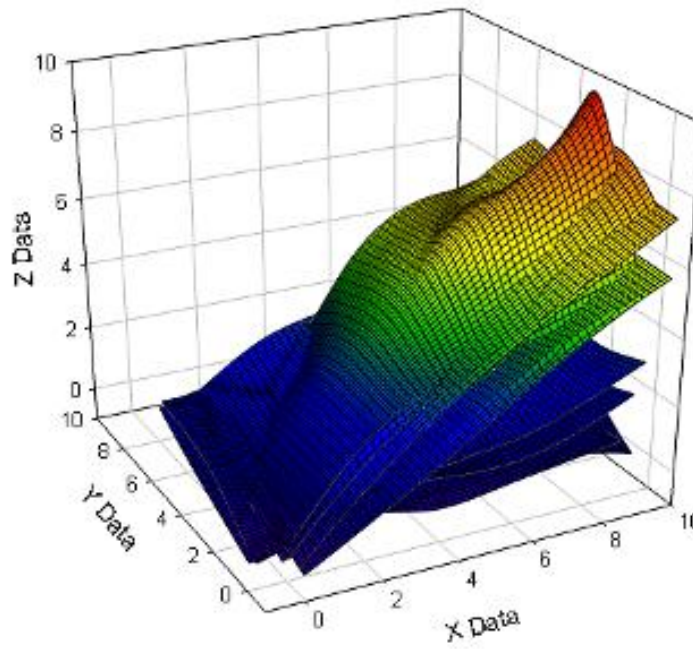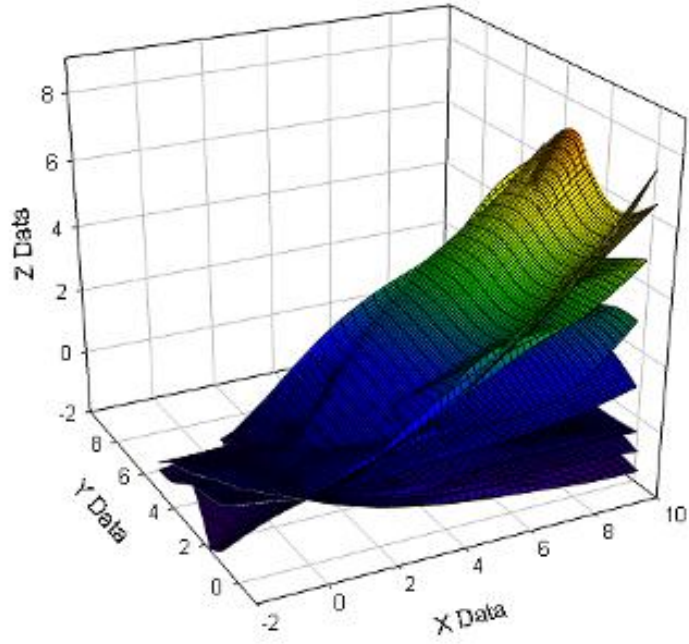

(b)

Figure 55 Wing A Up-flap (a) and Down-flap (b) Images

(a)

(b)

Figure 56 Wing B Up-flap (a) and Down-flap (b) Images

(a)

(b)

Figure 57 Wing C Up-flap (a) and Down-flap (b) Images
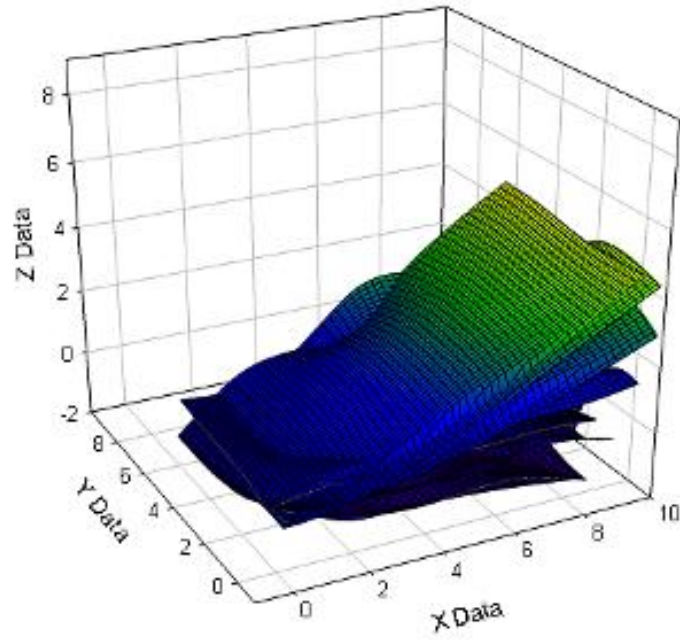
(a)

(b)

Figure 58 Wing D Up-flap (a) and Down-flap (b) Images
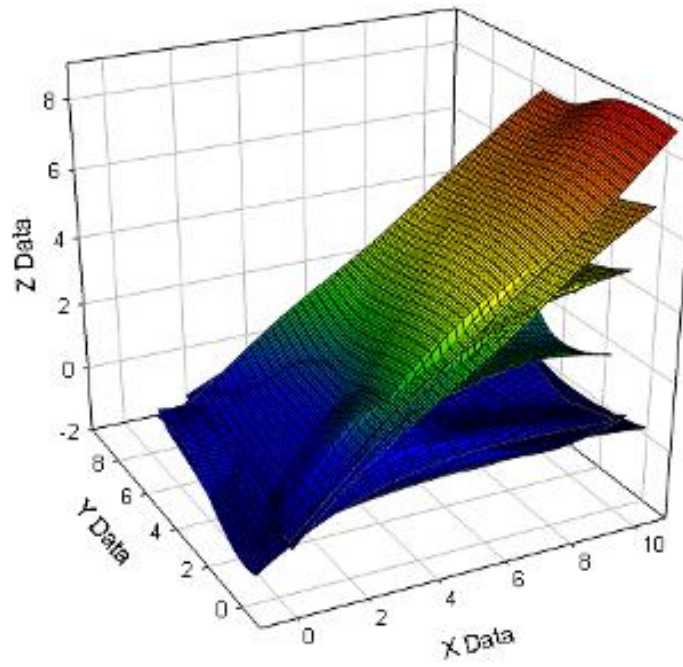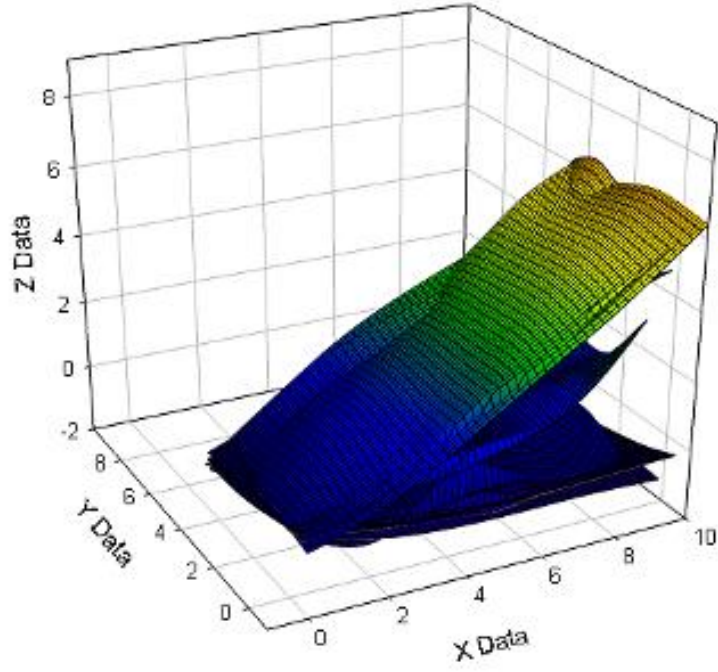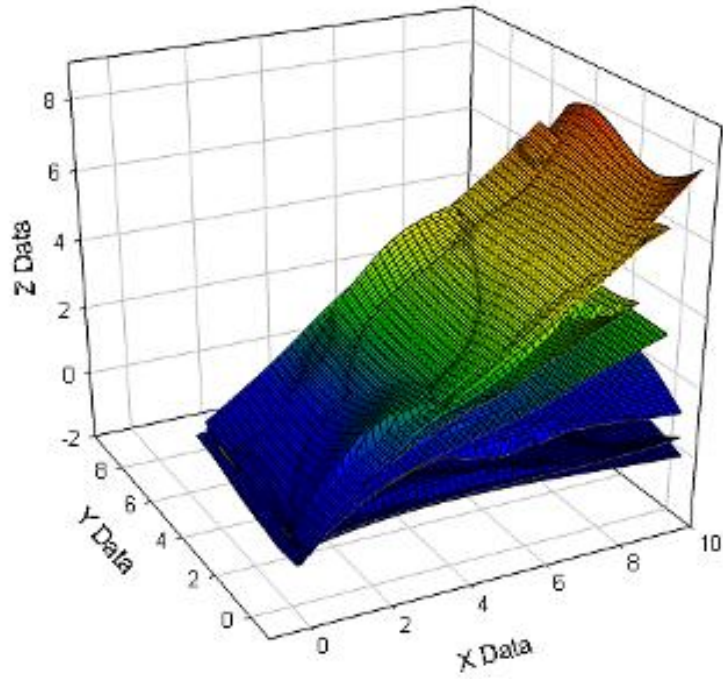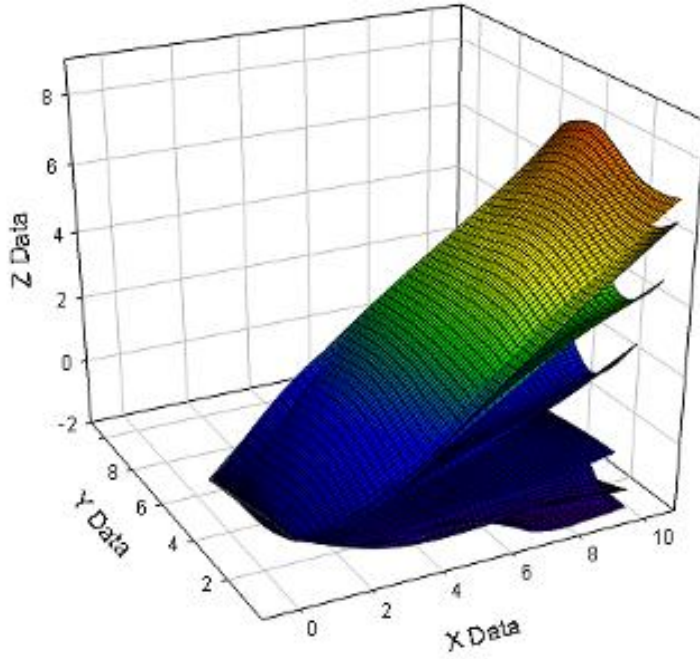
(a)

(b)

Figure 59 Wing E Up-flap (a) and Down-flap (b) Images
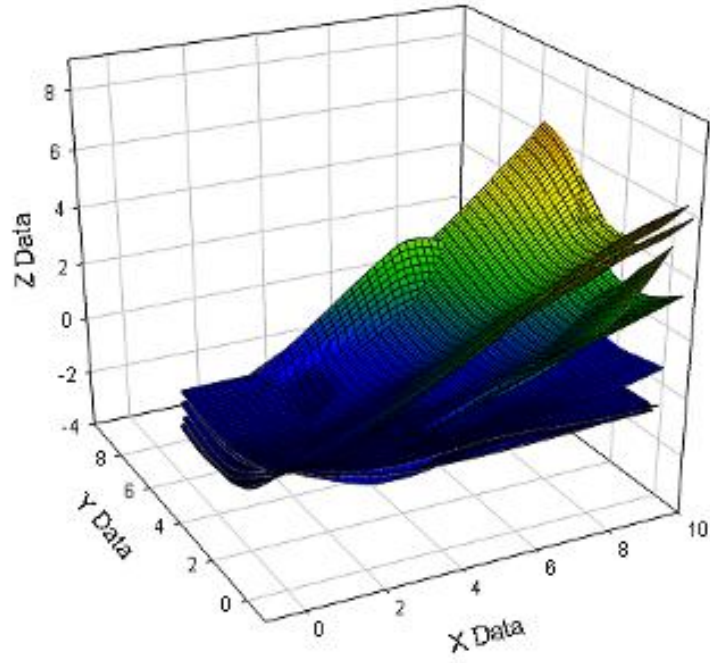
(a)
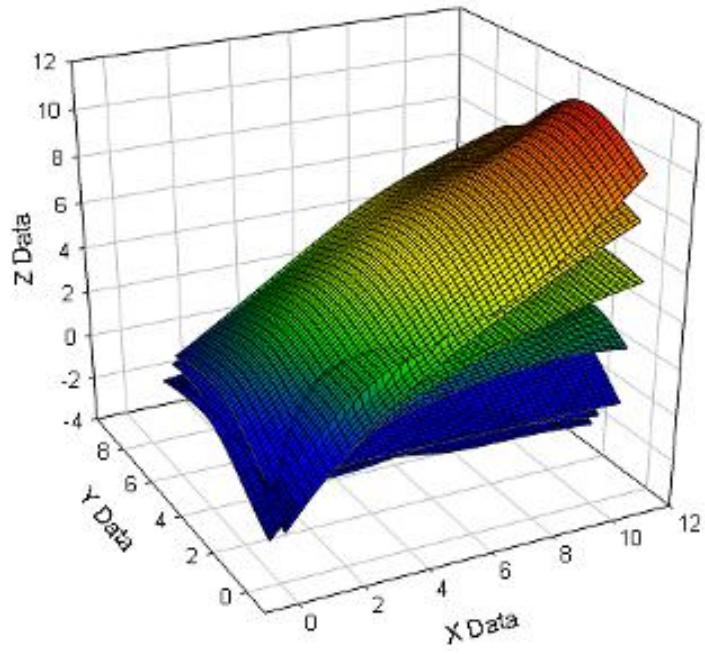
(b)

Figure 60 Wing F Up-flap (a) and Down-flap (b) Images

4.5.3 Measured Imaging

Once calculated images were created, the next step was to develop measured images for the six different wing constructions. The wings move laterally as well as vertically, as indicated by the tracking of the leading spar from the over-top perspective; the calculated images neglect this lateral motion. The z dimension deformations calculated for the calculated imaging are carried over into the measured imaging; however, the x and y values for each of the 15 points in each wing image needed to be tracked throughout the 15 different mechanism angles. Using image analysis software, values for x and y for each point in the wing throughout the 15 different mechanism angles were determined and used to create 3-D image plots. Figure 61-Figure 64 show the 15 measured images for wing F.
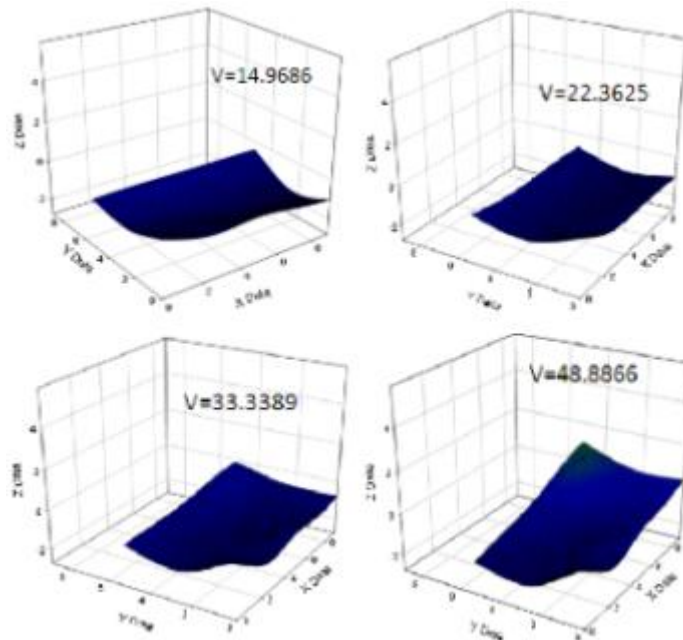
Figure 61 Measured imaging for wing F, angles 1-4
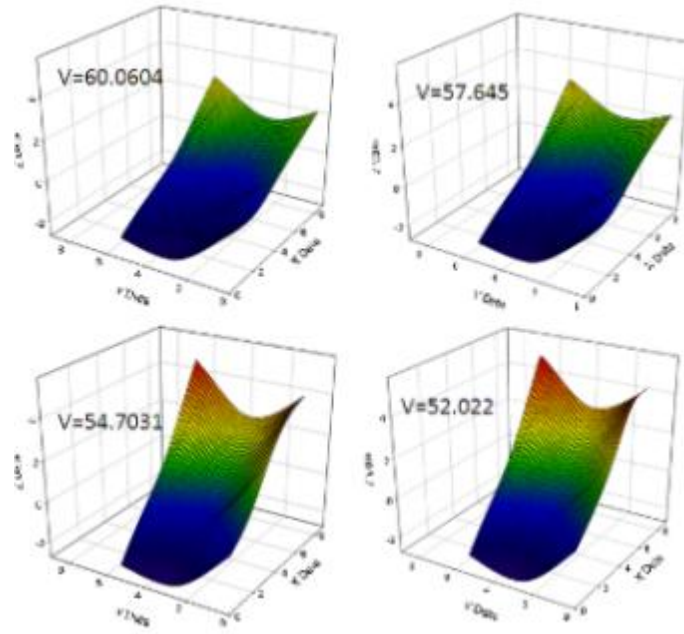
Figure 62 Measured imaging for wing F, angles 5-8
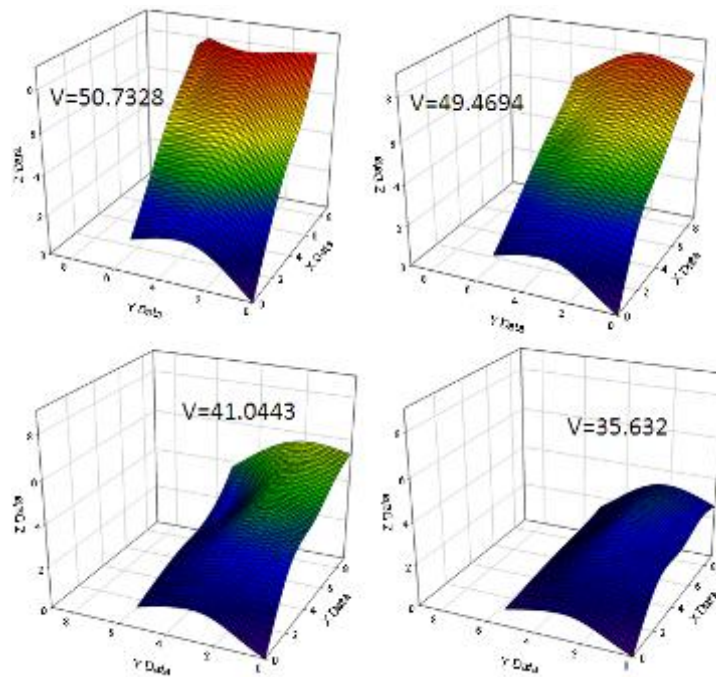
Figure 63 Measured imaging for wing F, angles 9-12
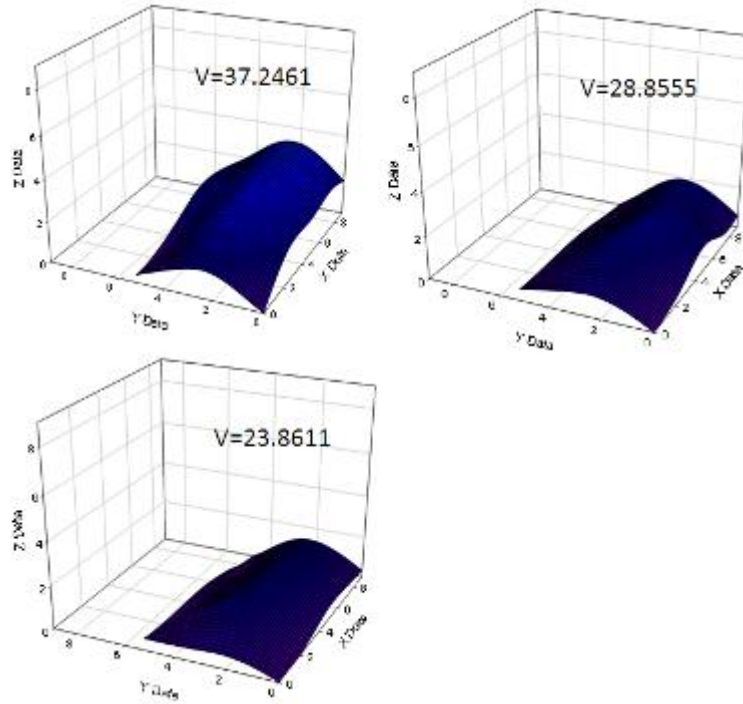
Figure 64 Measured imaging for wing F, angles 13-15

Much like the calculated images, the wing F measured images were generally smooth throughout the flap cycle. Also, the general bowl-shape again increased throughout the up-flap, reversed direction at the peak angle, and decreased throughout the down-flap as the air was forced out of the wing. The measured images, however, more accurately depict the position of the shape relative to the mechanism attachment point and show how much the rear edge of the wing moves to create the bowl shape. Measured imaging was completed for the remaining five wing designs; Figure 65-Figure 70 show the combined images for both the down-flap and the up-flap of each different wing construction.
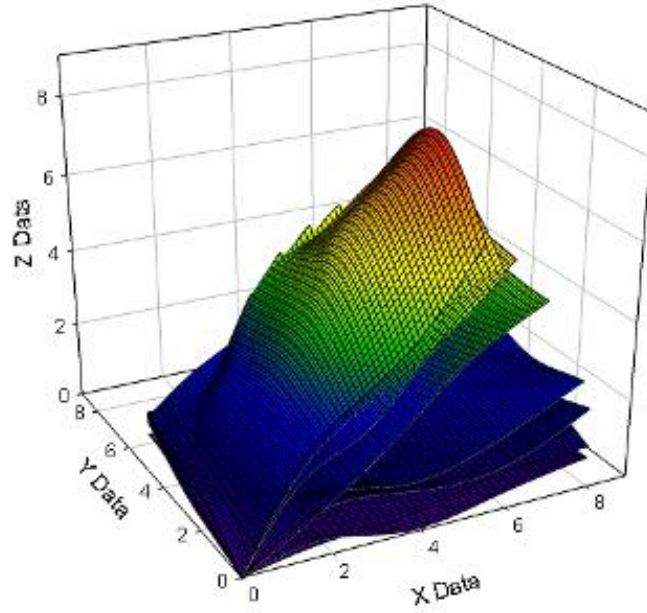
(a)
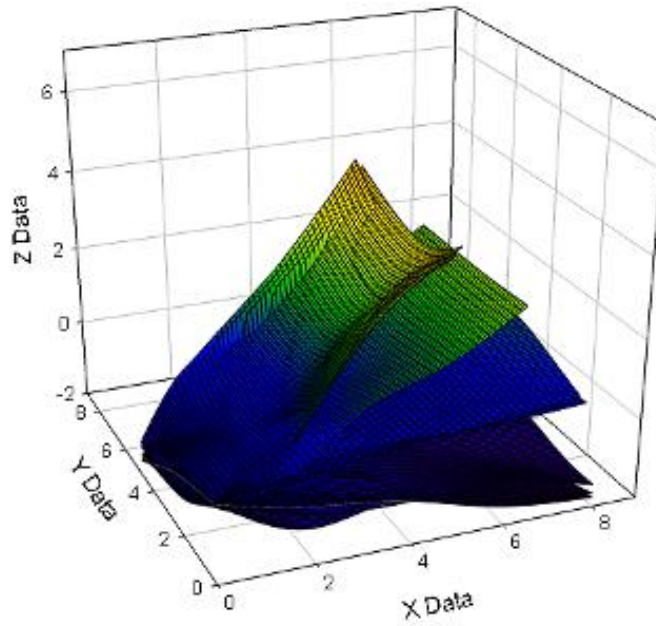
(b)

Figure 65 Wing A Down-flap (a) and Up-flap (b) Images
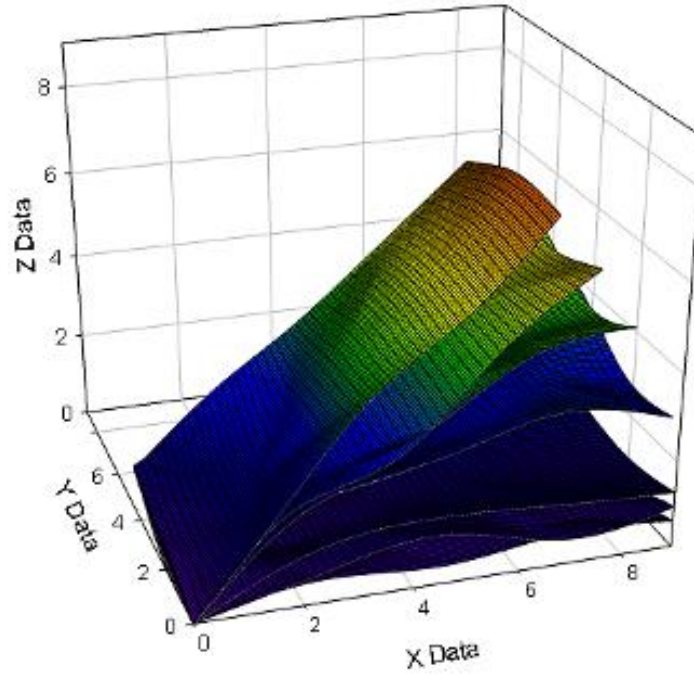
(a)
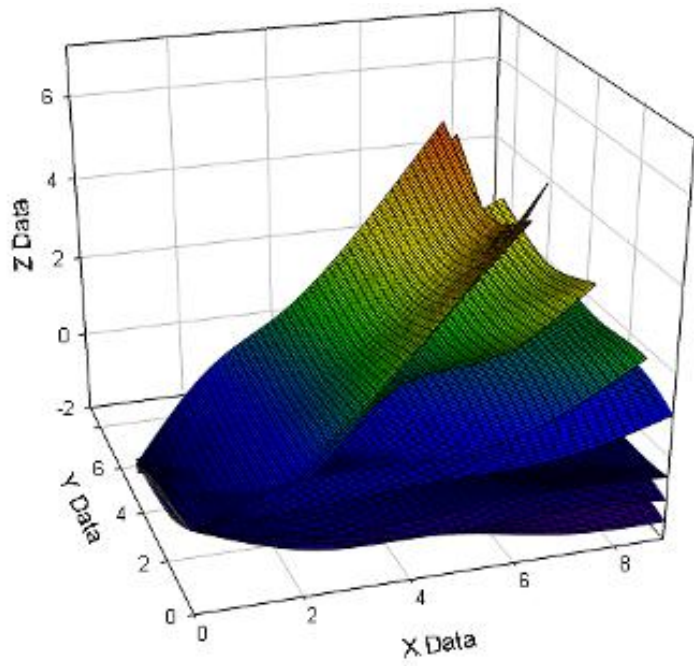
(b)

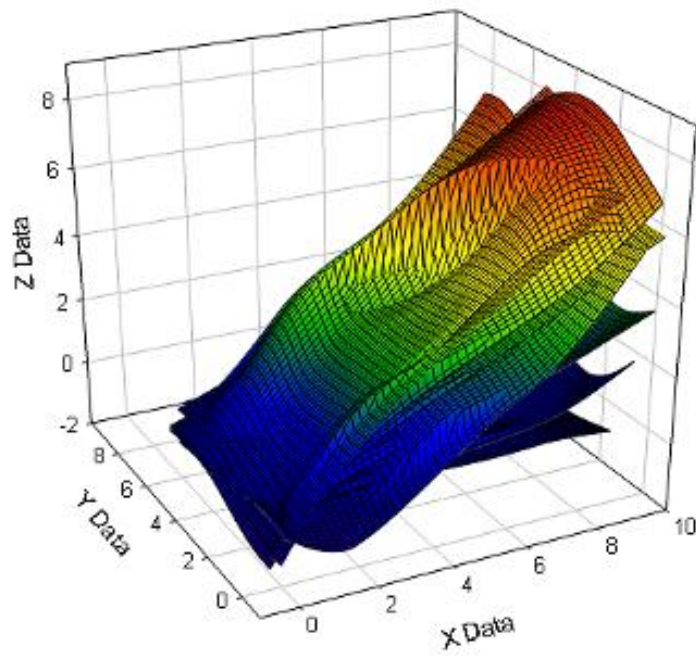Figure 66 Wing B Down-flap (a) and Up-flap (b) Images
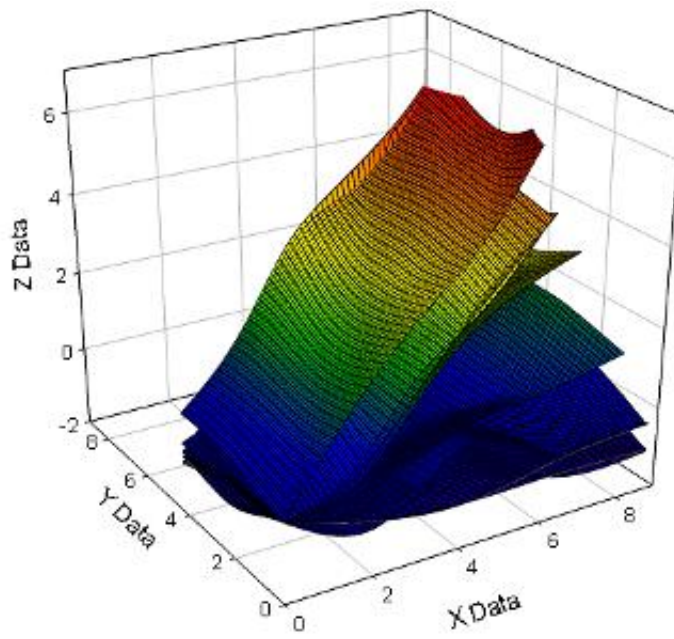
(a)
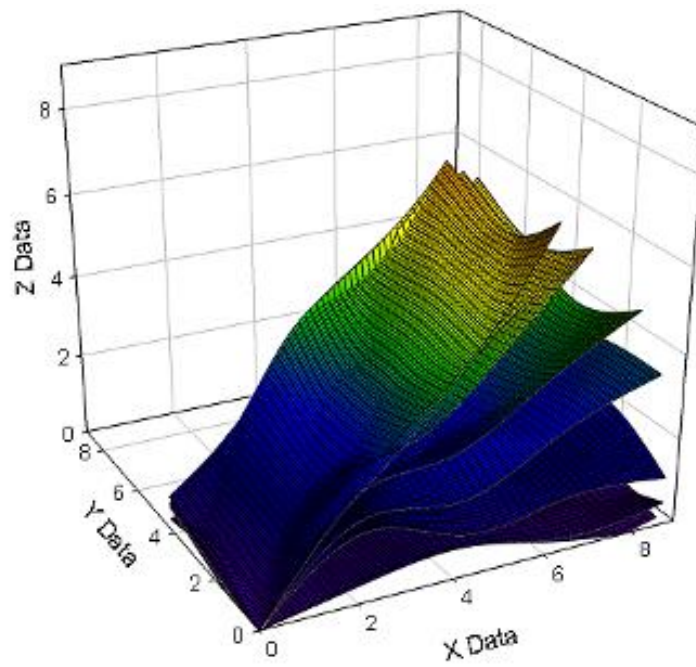
(b)

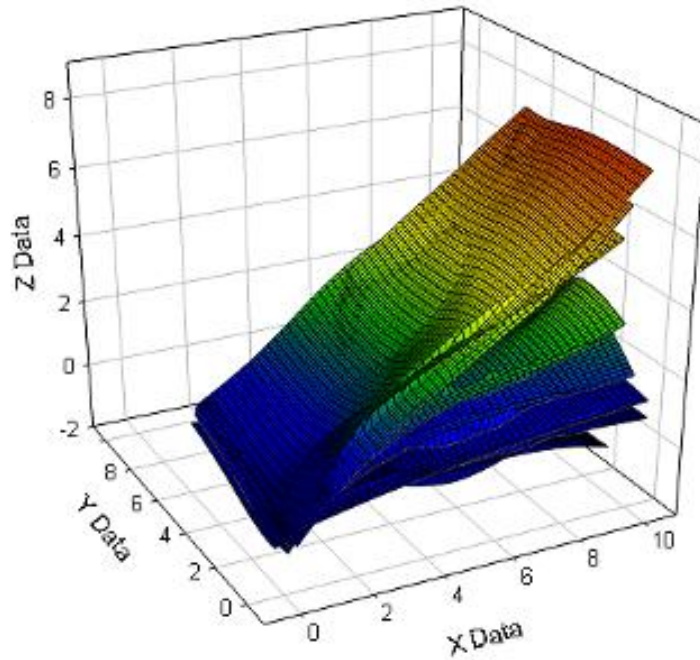Figure 67 Wing C Down-flap (a) and Up-flap (b) Images
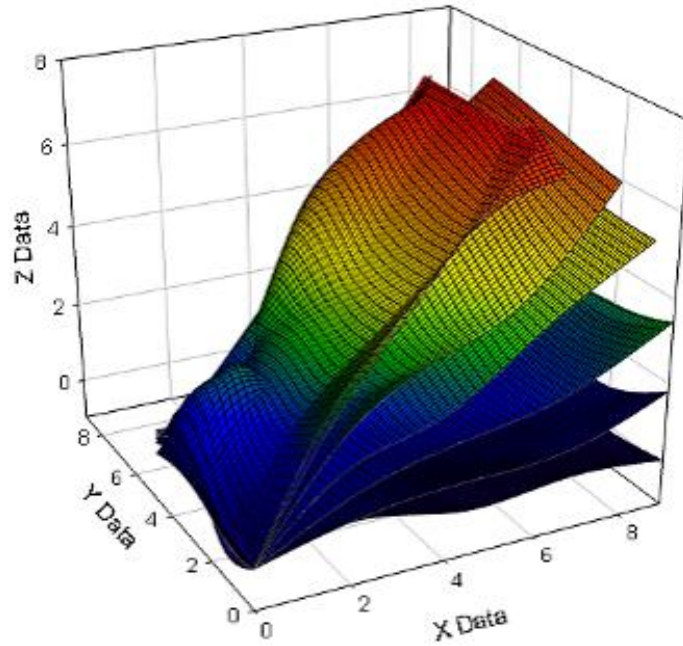
(a)
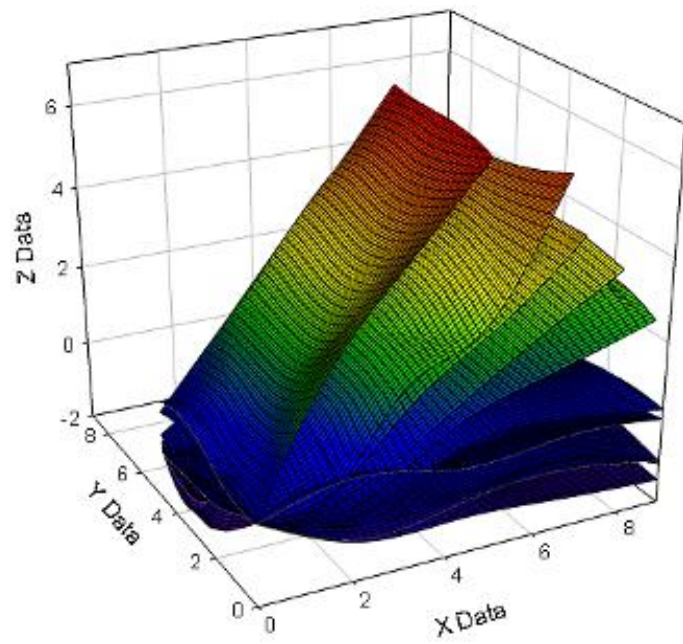

(b)

Figure 68 Wing D Down-flap (a) and Up-flap (b) Images
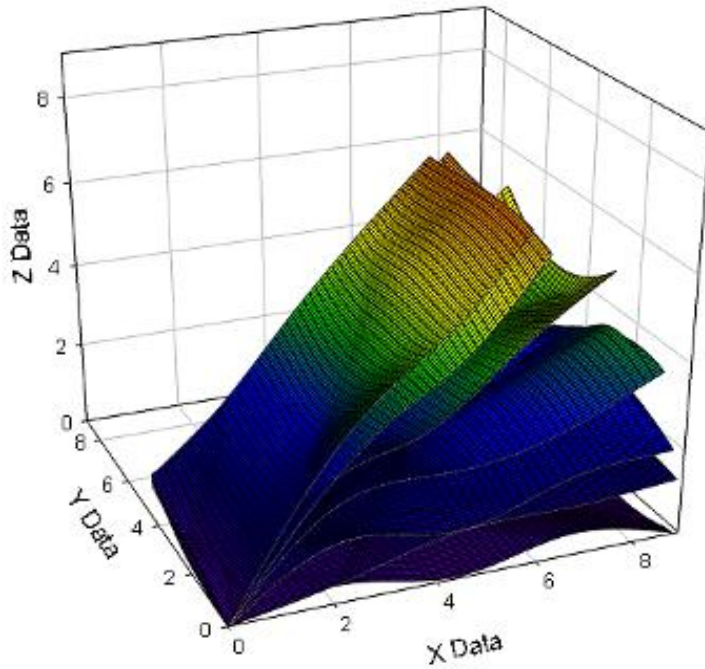
(a)
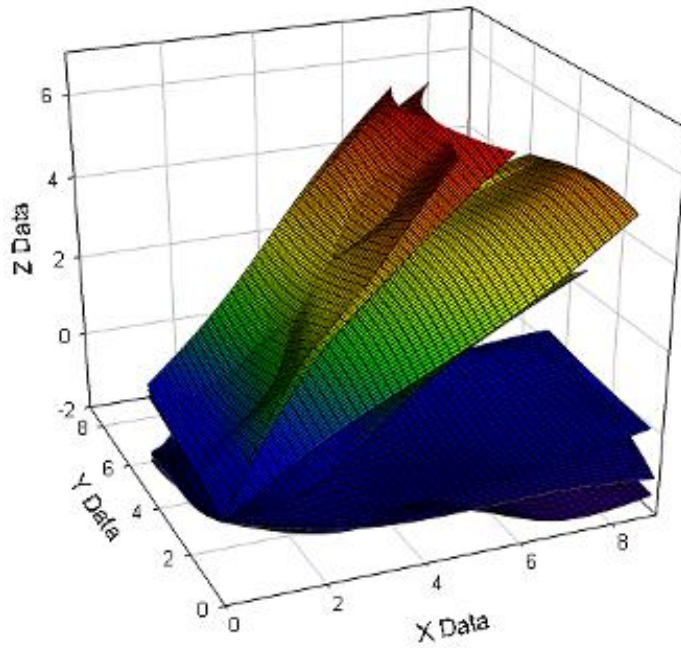
(b)

Figure 69 Wing E Down-flap (a) and Up-flap (b) Images
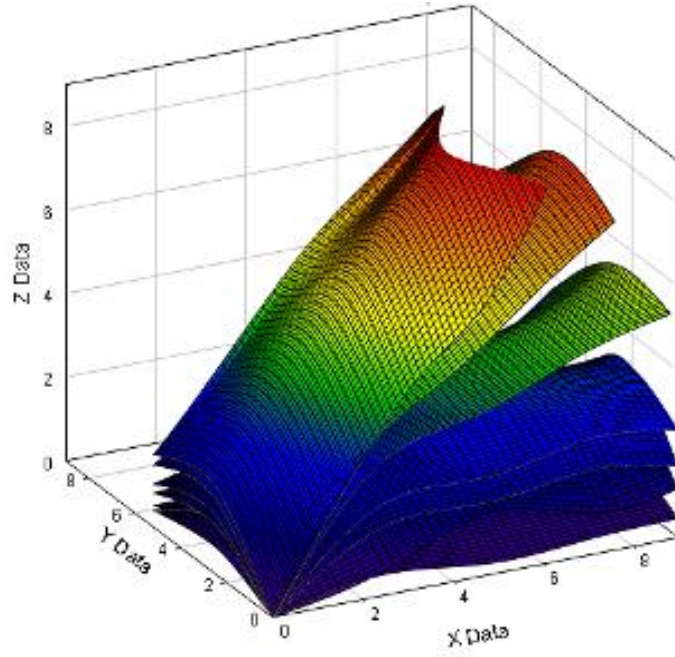
(a)
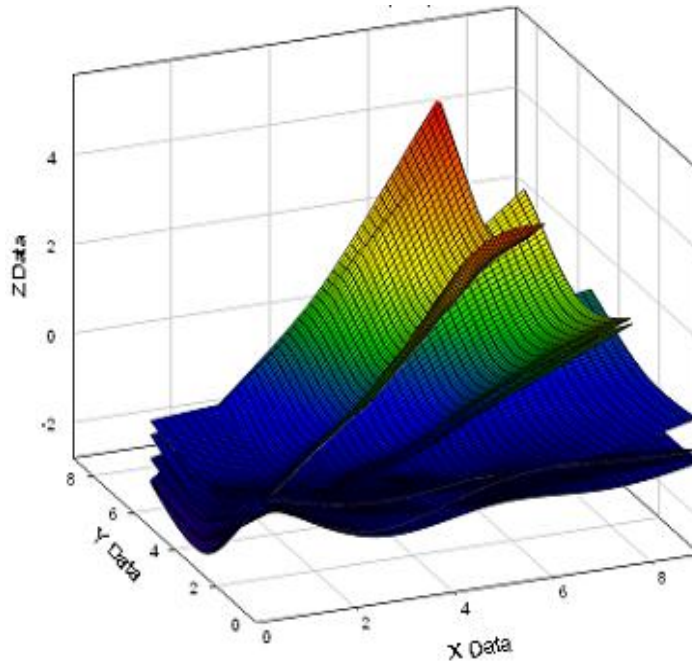
(b)

Figure 70 Wing F Down-flap (a) and Up-flap (b) Images

91

Much like in the calculated images, the ideal wing shape forms a bowl-like structure during the up-flap, with volume increasing as the mechanism angle increases. At the maximum mechanism angle, the direction of the wing shape reverses, and the bowl-like structure decreases as the wing travels through the down-flap and forces the air out. In the calculated imaging, all of the wing designs at least slightly resembled the bowl-like structure; for the measured imaging, however, the rippling and folding effects were much more magnified. Wings A, B, D, and E all have significant rippling and folding effects, reflecting their lower lift and thrust force outputs. Also, the magnitudes of the volumes in these wing constructions are much less than those of wing F. Wing F has the smoothest bowl-like structures of all the wing constructions; this is reflected in its high volume, lift and thrust values, as well as its overall performance.

4.5.4 Summary

Wing imaging is an important part of the wing characterization because it provides visual confirmation of the accuracy of the other components of the characterization. The calculated imaging verifies the centroid along the leading spar and volume calculations, while the measured imaging verifies the movement of the leading spar and the centroid calculations perpendicular to the leading spar, as well as confirming the calculated results. The wing imaging as a whole also reinforces the lift and thrust forces measured for each wing set. Because wing imaging is the visual representation of all of the data found, the addition of measured and calculated imaging to the wing characterization enhances the value of the complete wing characterization for flexible flapping wings.

4.6   Wing F Repeatability and Sensitivity Data

While wing imaging, both measured and calculated, confirm the lift and thrust forces calculated for the wing designs, the repeatability of the tests for identical wing sets is still questionable. Also, the wing designs are comprised of six grossly different spar configurations; how does slight variation in spar angle affect wing performance? Slight deviations occur during construction, but the actual sensitivity of the deviations in spar placement had not been explored. To investigate this, four additional wings were constructed: two identical wings were manufactured using the wing F spar orientation to determine the repeatability of the testing methods, while two more wings were constructed with slight variations on the wing F design to determine the sensitivity of the testing methods. In these two wings, the 0.04" carbon fiber spar closest to the center spar was moved either towards or away from the center spar by one inch. While one inch is a larger amount of deviation than would likely be encountered during manufacturing, it is a smaller change in spar location than the differences between the original six wing designs. Lift and thrust testing, as well as volume calculations and wing imaging, were done on all four additional wing sets.

4.6.1   Lift and Thrust Data

Lift and thrust were measured for the four-newly constructed wings. The resulting data can be seen in Figure 71.
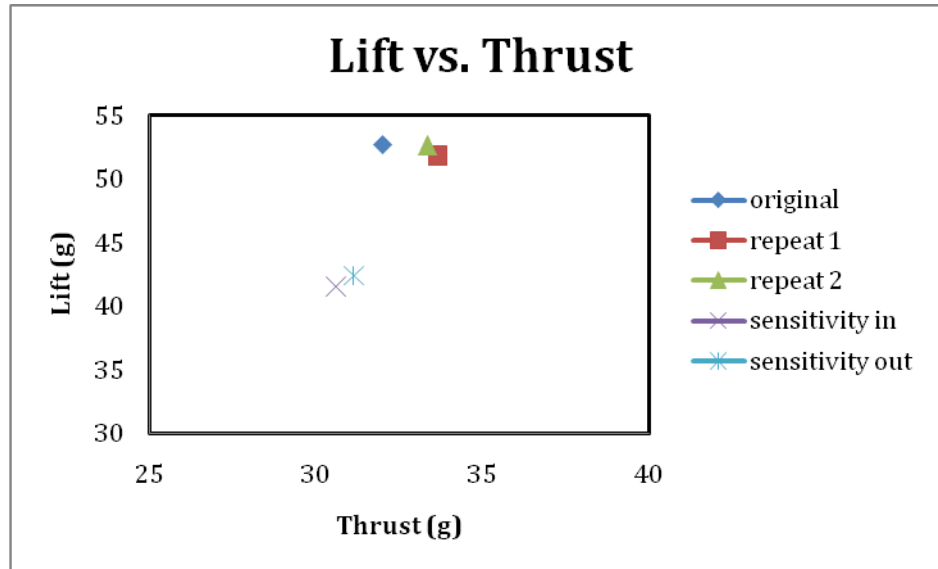
Figure 71 Lift vs. thrust data comparing the four wing F designs

As seen in the above graph, the two identical F wings performed very similarly to the original wing; the lift values were almost exactly identical, while the thrust in the two newly constructed wings was approximately one gram greater than the original value. This similarity indicates that the testing and manufacturing processes are repeatable and reliable. The two F wings with variation in the 0.04" carbon fiber spar nearest the center spar performed similarly, although significantly worse than the original F wing design. A decrease of approximately ten grams of lift and four grams of thrust, which is a 14% decrease in thrust performance and an 18% decrease in lift performance, occurred due to a one inch variation in spar location. This noticeable decrease in performance indicates the importance of accuracy in spar placement.

4.6.2 Volume Calculation

The volumes of the four wings were calculated at fifteen different angles throughout the flap cycle, as was done previously for the original six wing designs.

Figure 72 compares the progression of volume captured throughout the flap cycle for the four wings.
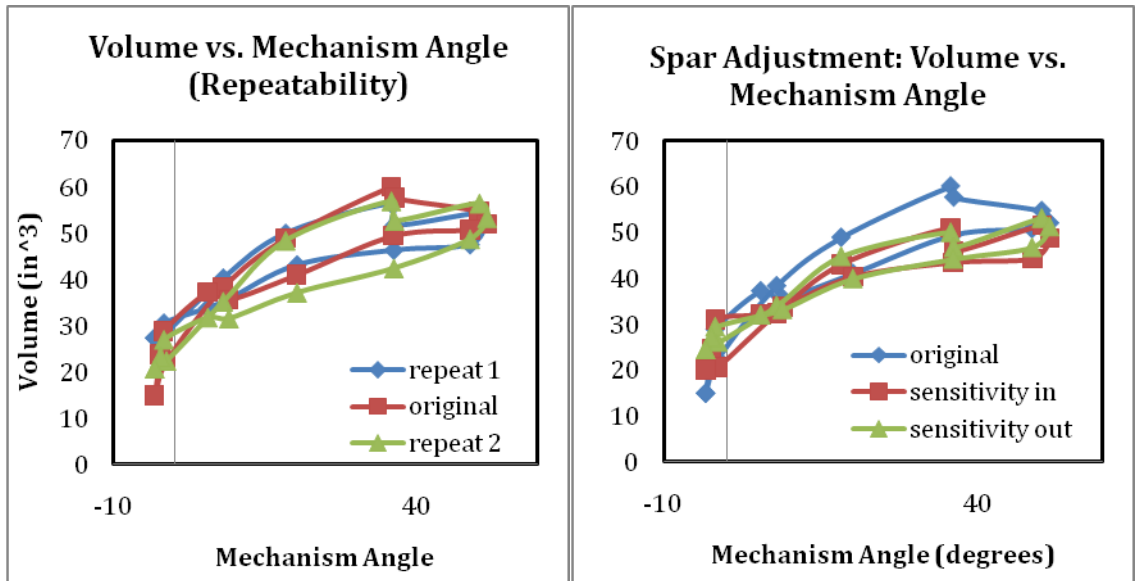
Figure 72 Graph comparing volume captured over flap cycle for the four wings

As seen in the above figure, the volume captured by the four wing sets is similar; however, the two wings in which the 0.04" spar was moved, named sensitivity in and sensitivity out in the graph, capture less volume than the other three wing sets. Also, the two wings identical to the original F wing design capture slightly less volume than the original wing, but still capture more volume than the other two wing sets. Since the difference in volume is small, the differences in the lift and thrust values must come from another factor, such as the overall shape of the wing throughout the flap cycle.

4.6.3 Wing Imaging

Like the original six wing designs, the four additional F wings were recreated using measured imaging at 15 different mechanism angles in the flap cycle. Figure 73-

Figure 76 show the resulting images. All four wings have smooth, bowl-like structures, just like the original F wing images. However, the two wings that were made identically to the original wing F, labeled repeat 1 and repeat 2, have more curve to their wing structures than the two wings with variations in their 0.04" carbon fiber spars located adjacent to the center spar, labeled sensitivity (in) and (out). The latter two wings are slightly flatter and do reach lesser maximum values than the wings constructed with the original wing F design. This difference in shape, even though it is slight, contributes to the lesser values generated by the sensitivity (in) and (out) wings in lift and thrust testing. This again indicates the importance of precision placement of carbon fiber spars during wing construction.
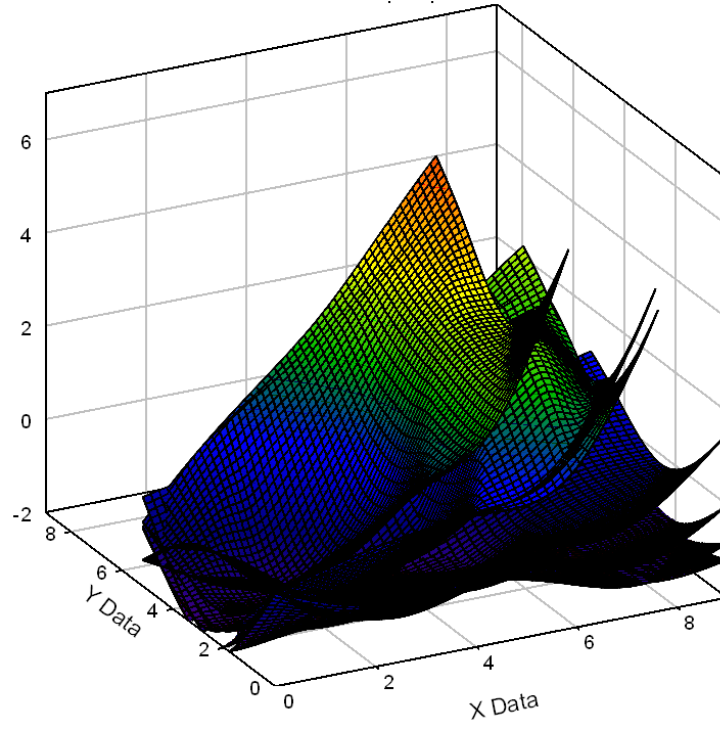
(a)
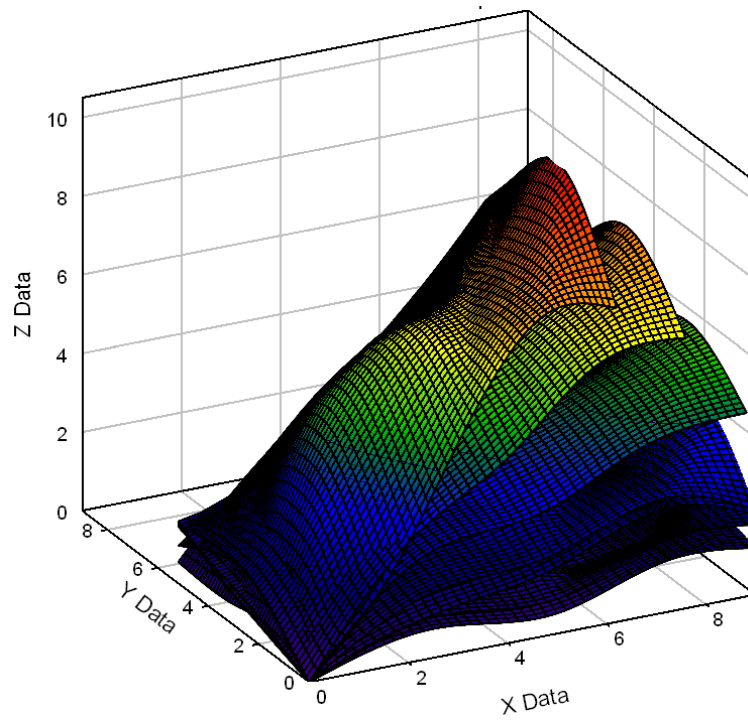
(b)

Figure 73 Wing F repeat wing 1 up-flap (a) and down-flap (b) images
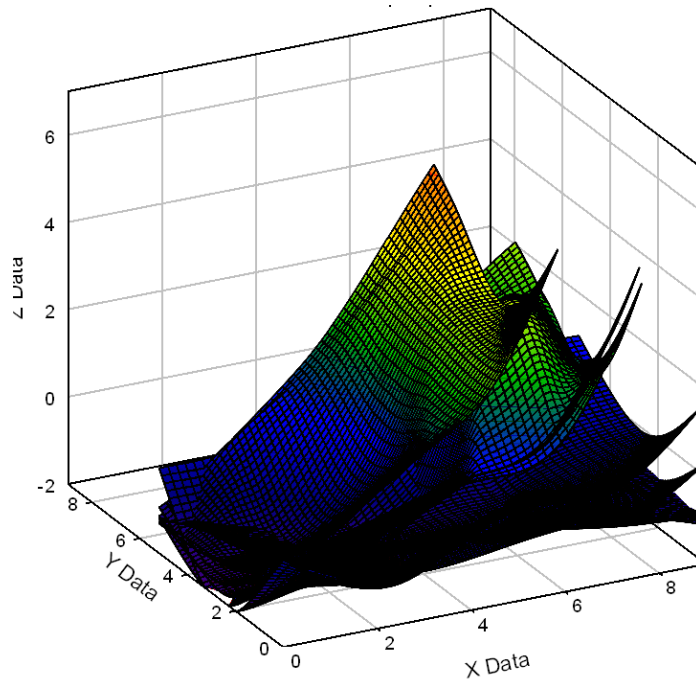
(a)
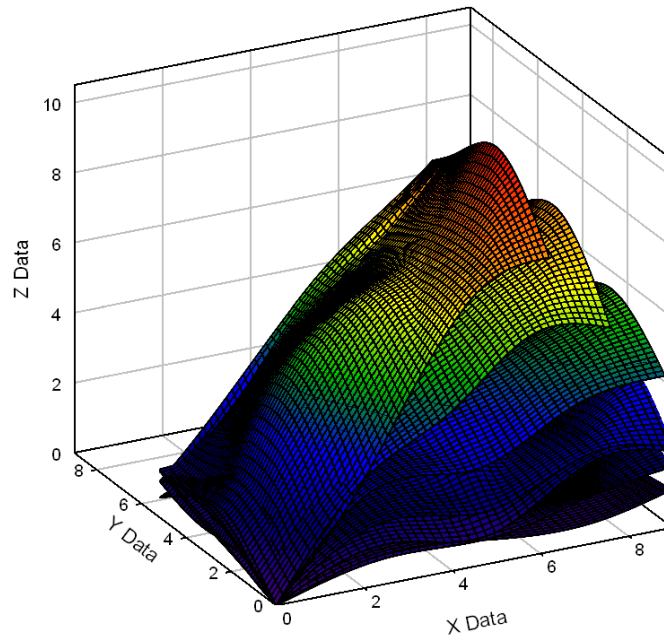
(b)

Figure 74 Wing F repeat wing 2 up-flap (a) and down-flap (b) images
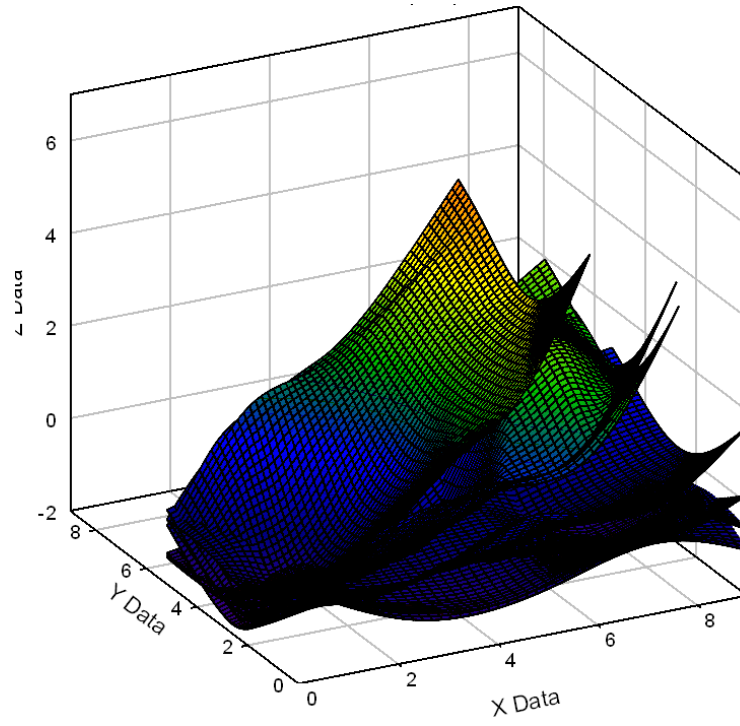
(a)
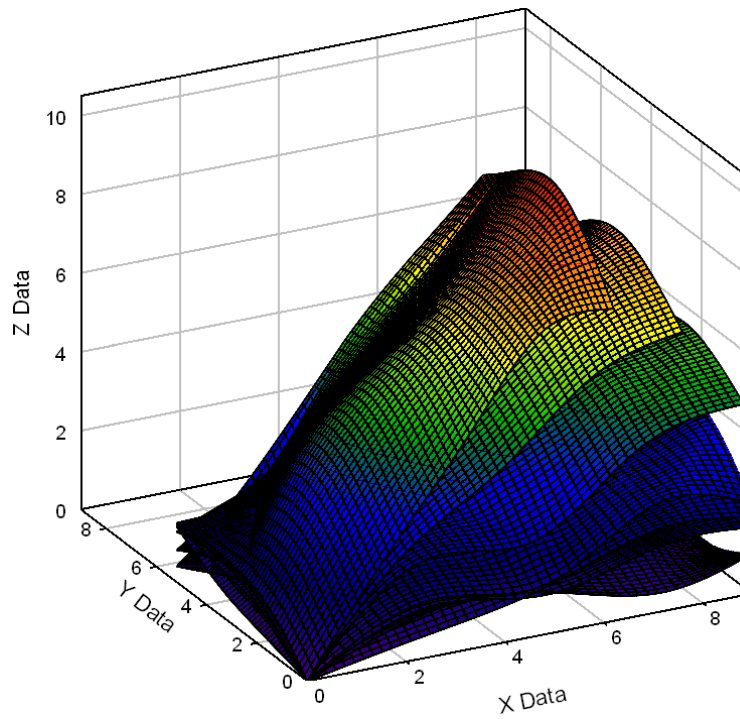
(b)

Figure 75 Wing F sensitivity wing (in) up-flap (a) and down-flap (b) images
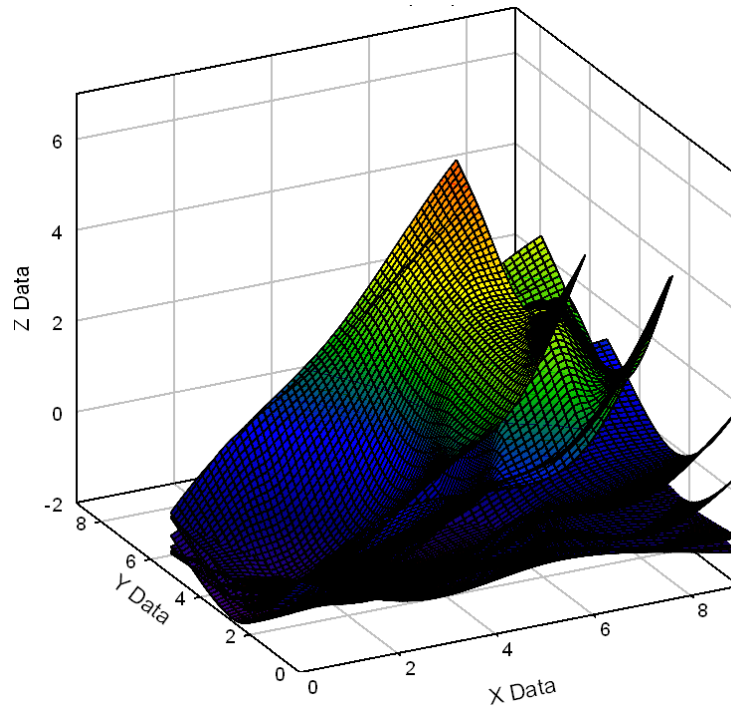
(a)
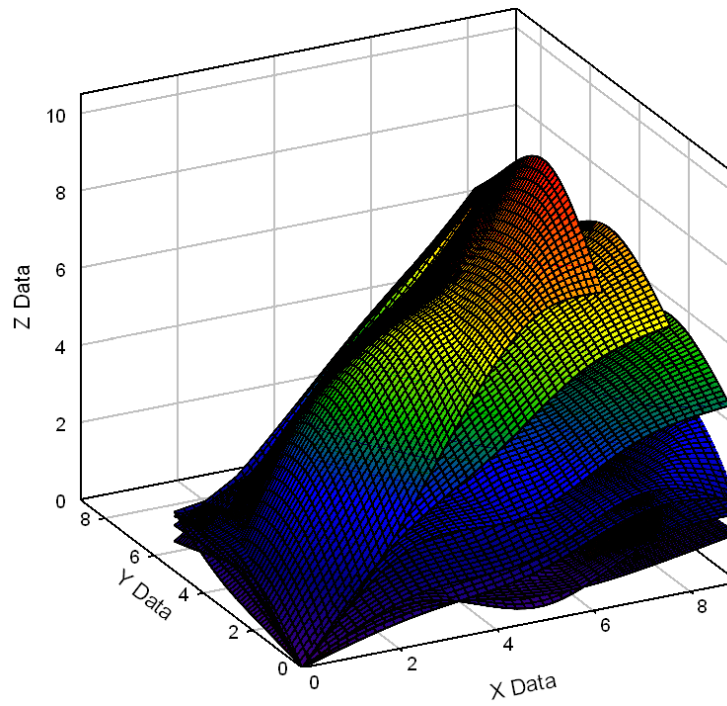
(b)

Figure 76 Wing F sensitivity wing (out) up-flap (a) and down-flap (b) images

The issues of repeatability and sensitivity in wing testing and construction were obvious concerns; thus, four wings were constructed, two as identical copies of wing F to test repeatability, and two with small spar variation in the wing F design to test sensitivity. All four wings were subjected to lift and thrust testing, and the wings were characterized using high-speed imaging to obtain volume values and measured images throughout the flap cycle. As indicated by the results presented in this section, the methods used are indeed repeatable between identical wing constructions, and precision in spar placement is crucial during wing construction to provide accurate results.

4.7   Summary

In this chapter, a method of characterizing flexible flapping wings was presented. The method, completed using high-speed imaging from multiple angles and image processing software, incorporates leading spar tracking, deformation measurement, centroid and volume calculations, and measured and calculated imaging to fully describe wing motion through fifteen different angles in the 55-degree flap cycle. The wing characterization developed was used to explain the lift and thrust forces generated in wing testing; results confirmed that the wing F design was the best performing in lift and thrust due to the large amount of volume captured, and smooth shape formation throughout the flap cycle. The large amount of volume captured was seen in the volume calculations, as well as represented in the movement of the leading spar and the changes in centroid location, both horizontally and vertically. Issues including repeatability and sensitivity were evaluated and discussed; the method was deemed repeatable and the importance of precision in construction was emphasized. Thus, an accurate method of characterizing flapping wing flight has been developed.

Chapter 5:   Solar Cell Testing

The repeated success in the field of large UAVs and the progression of research in aerodynamics of small-scale flight has led to groundbreaking work in the development of miniature air vehicles (MAVs).   The development of small-scale unmanned vehicles opens up a whole field for the UAV, as many of today's applications are restricted by the size of the current vehicles used. Smaller, lighter, and cheaper micro-air vehicles allow for a wider range of application of UAVs; however, miniaturization forces trade-offs to be considered. In order to reduce the size of the vehicle, sacrifices in terms of payload and flight time must be made. Creating a multi-functional structure within the micro-air vehicle allows for fewer trade-offs to be considered, since an additional energy-harvesting source provides power to the MAV. In MAVs, flight endurance is one of the most important factors affecting successful performance and implementation in different applications. Flight endurance time is directly related to the energy supplied by the battery, the weight of each component of the MAV, and aerodynamic parameters. Thus, combining the battery with one of the components of the MAV would result in a multi-functional structure that would provide an additional energy source while minimizing the weight increase. The implementation of solar cells on the wings of the current MAV at University of Maryland should decrease the battery weight, increase the weight of the wings, decrease the compliance of the wings, and increase the payload capacity. The goal of this chapter is to determine a carbon-fiber spar/solar cell configuration in order to minimize the change in compliance of the wings, making the gain in payload capacity and decrease in overall weight offset the decrease in lift and thrust performance due to change in compliance, and resulting in an overall positive performance change.

5.1 Solar Cells

5.1.1 Motivation

The integration of solar cells into the current MAV wing structure would create multi-functionality within the wings. Multi-functional wing structures that not only provide lift and thrust, but act as an energy source would be a great improvement to current MAV design. It would allow for an increased flight time, while decreasing the payload contribution of a large power source, thus potentially allowing for either a size reduction with the same performance capability, or an increase in overall payload capacity. The integration of solar cells is also a stepping-stone on the path of completely removing the need for an external power source, such as a heavy battery, which creates huge improvements in payload requirements. Additionally, the integration of solar cells may pave the way for other components within the MAV to become multi-functional; the vast array of MAV applications may create a need for additional capabilities that would best be incorporated in a multi-functional capacity.

5.1.2 Types of Solar Cells

In order for the solar cells to be successfully incorporated into the MAV, the correct type of solar cell must be selected. The solar cell must be able to charge a 3.7-volt battery while also demonstrating flexibility and durability; a completely rigid solar cell would disrupt the compliance of the Mylar-based film, and durability is required since testing and applications involve outdoor flight. Also, a variety of shapes and sizes are necessary to determine the best combination of spar configuration and solar cells to produce successful flight. The solar cells selected for testing were four variations of

Silicon Solar's flexible solar panels [55]. The 2x5 solar cell is 3.9" long and 1" wide, and is rated at 3V / 25mA / 0.07W [55]. The 3x5 solar cell is 2.5" long and 1.5" wide, and is rated at 3V / 22mA / 0.06W [55]. The 3x7 solar cell, seen in Figure 77, is 3.3" long and 1.5" wide, and is rated at 4.2V / 22mA / 0.09W [55]. The 7x3 solar cell is 3" long and 2.9" wide, and is rated at 3.6V / 50mA / 0.18W [55].

Figure 77 Flexible Solar Panel from Silicon Solar, Inc. [55]

5.1.3 Locations on Wings

Because no data had previously been accumulated to guide how solar cell placement would affect the compliance of the wings, the placement of the solar cells was selected based on the location of the spars, and the shapes of the different cells. The goal was to minimize the increase in stiffness in the Mylar-based film, so that the wing could still form the ideal bowl-like shape, to capture as much volume and direct the flow of air out of the wing in a direction to maintain good lift and thrust performance. For that

reason, the solar cells were placed near spars in areas that seemed to minimize an increase in stiffness. Figure 78 shows where each of the different sized solar cells was placed.
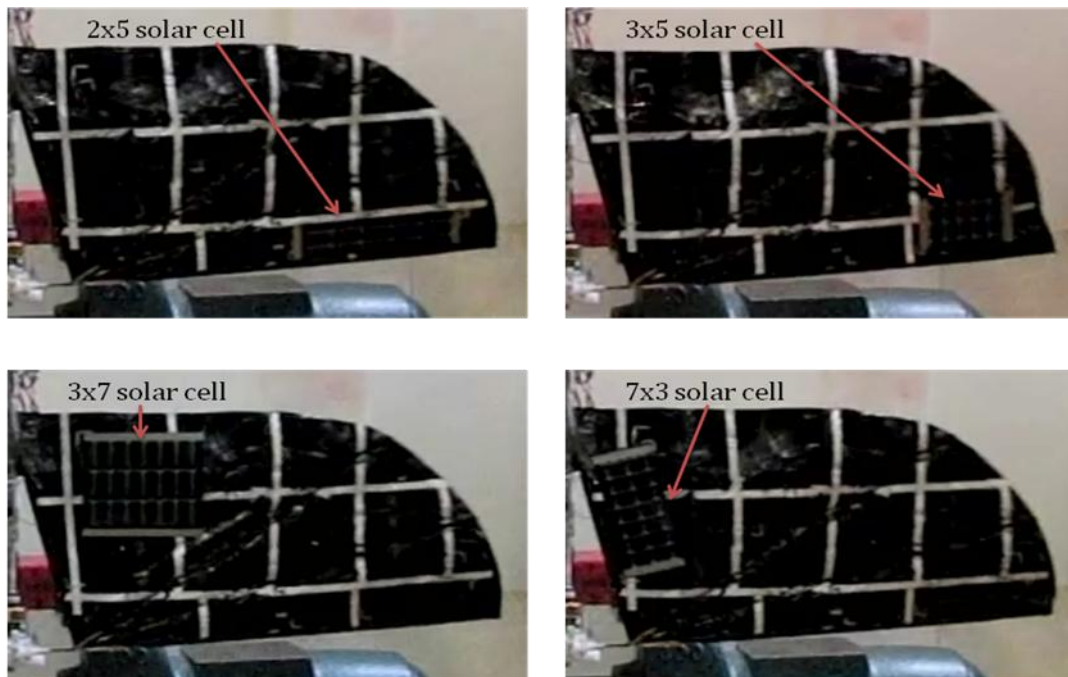
Figure 78 Solar cell placement on wings

5.2 *Data Collection*

The wing characterization method described in Chapter 4 was applied to the four different solar cell configurations on two different wing types, resulting in eight characterizations being performed. Leading spar displacement, centroid location, volume captured, and measured wing imaging were all developed for the different configurations.

5.2.1 Wing F Results

Figure 79 compares the lift versus thrust data for the four solar cell configurations with the original wing F lift and thrust data. The lift and thrust forces generated by the solar cells were not as large for wing F as the original values; the addition of the solar cells to the wings obviously negatively impacted compliance. Because the optimal placement is in the upper right quadrant of the chart, the placement of the 3x5 solar cell has the best overall result of the four different configurations tested; however, none of the solar cell configurations really outperforms the others.
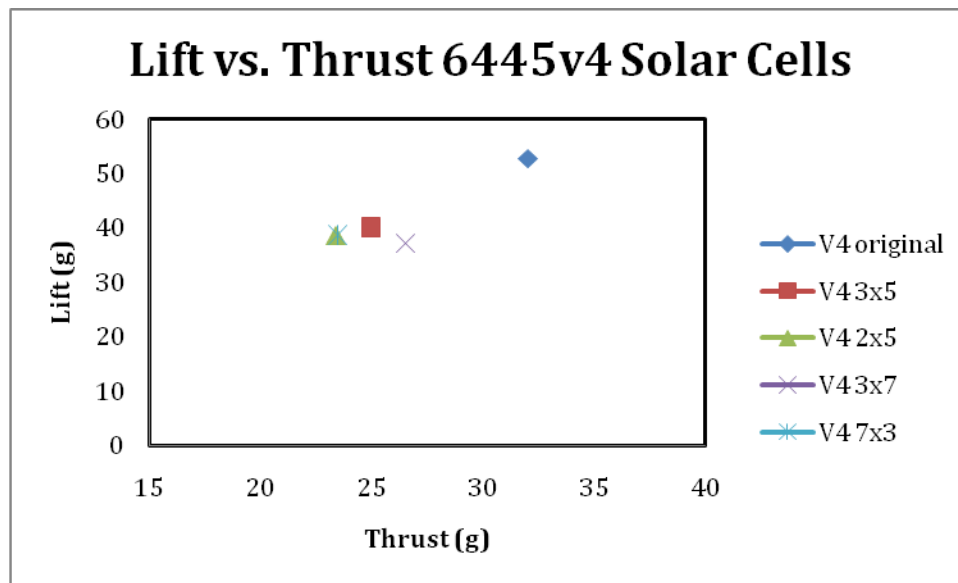
Figure 79 Lift vs. thrust for solar cells on wing F

The motion of the leading spar, both from the head-on and over-top perspective, were also considered for wing F with the four different solar cell configurations. Figure 80 and Figure 81 compare the leading spar's head-on and over-top motion, respectfully.
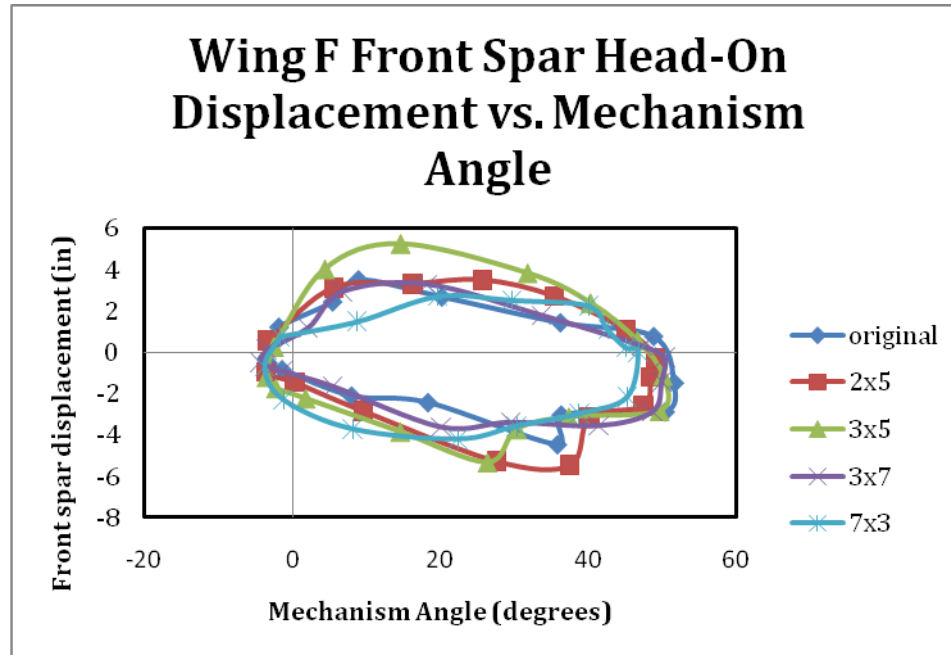
Figure 80 Leading spar head-on displacement (Wing F w/solar cells)

From the head-on perspective, the wing F original data, shaped like a parallelogram, most closely approximates how the leading spar should move; while the spars move similarly for all configurations from the head-on perspective since the spars are all the same 0.06" thickness, the addition of the 2x5 solar cell and the 3x5 solar cell caused more deviation from the original data, since those cells were placed very close to the leading spar. The placement of those cells increased the compliance in the leading spar, causing it to be driven further from the rigid position.

From the over-top perspective, the wing F original data, shaped like a bow tie, again most closely approximates how the leading spar would move in an ideal case. The addition of solar cells had a significant effect on the results; all four configurations had very skewed plots. The motion in all four configurations was significantly reduced, indicating that the solar cells restricted the measured movement of the leading spar.
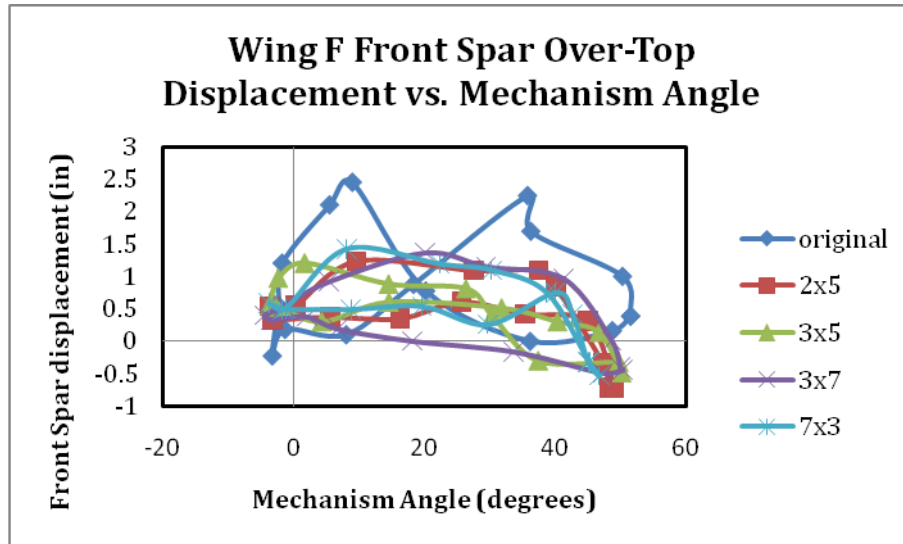
Figure 81 Leading spar over-top displacement (Wing F w/solar cells)

After the leading spar displacement was considered, the motion of the horizontal and vertical centroids were considered for the four different solar cell configurations. The resulting plots can be seen in Figure 82 and Figure 83.

Like in the original wing set, the ideal centroid location should move away from the center spar during the up-flap and towards the center spar during the down-flap for the horizontal values. In observing Figure 82, the original wing best approximates the ideal, with the 3x5, 2x5, and 7x3 solar cell configurations also following similar patterns. The 3x7 solar cell configuration, however, has a very different centroid path; it does move away from the center spar during the up-flap, but has a much greater motion towards the center spar during the down flap and shifts from toward the center spar to away from the center spar much sooner than the other wing configurations. Because the 3x7 solar cell covers the most area of the wing and was placed in an area lacking spars, it had the greatest effect on changing the compliance of the wing and also on the horizontal centroid location.
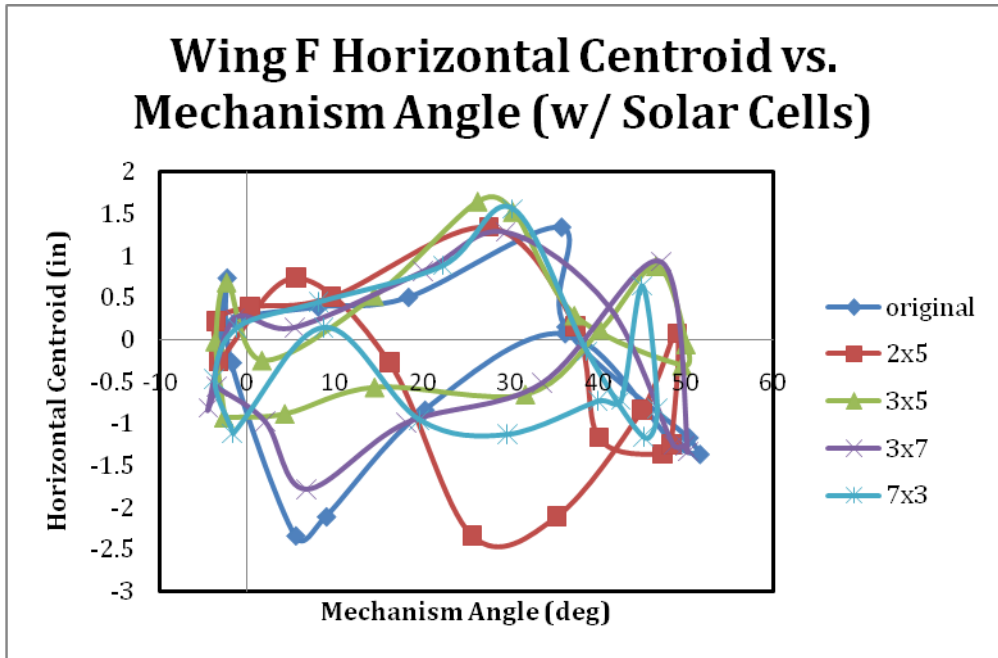
Figure 82 Horizontal centroid progression (Wing F w/solar cells)
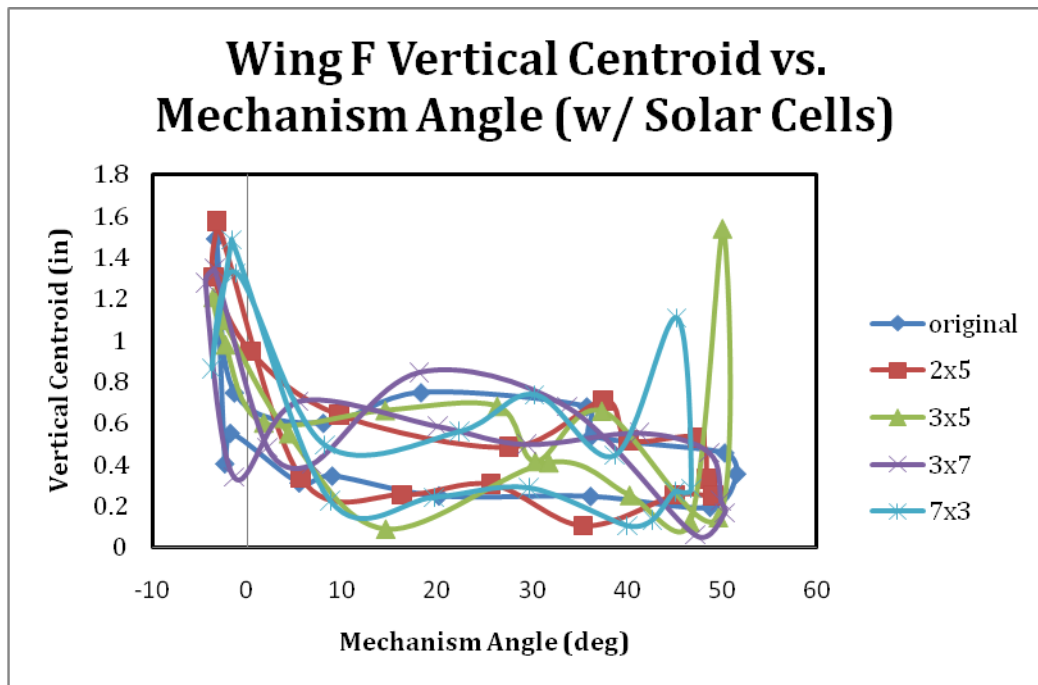
Figure 83 Vertical centroid progression (Wing F w/solar cells)

For the vertical values, the ideal centroid location should move away from the leading spar during the up-flap, and towards the leading spar during the down-flap. In observing Figure 83, all of the solar cell configurations follow the original wing spar with the exception of the 3x7 configuration; in that wing, the centroid moved opposite the ideal. Again, this is due to the effect of the solar cell placement on the wing compliance; because it was placed in an area of the wing lacking in spars, and thus very compliant, putting a solar cell there caused a significant reduction in the wing's overall compliance. The 3x5 and 7x3 configurations also had large centroid movement at the shift from up-flap to down-flap; this is due to placement of the solar cells near the center and leading spars, affecting how the wings are able to snap from up-flap to down-flap. Like in the horizontal centroid, the 3x7 solar cell caused the greatest change in vertical centroid location because its large area significantly reduced compliance in the wing.
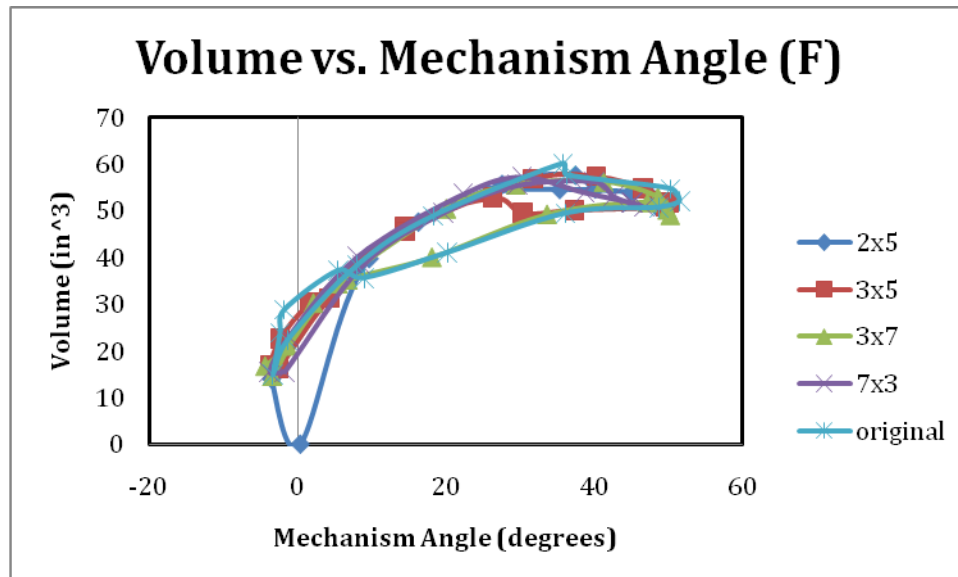
Figure 84 Volume vs. Mechanism angle for solar cells on wing F

The final calculated value considered for the F wing design with the addition of solar cells is volume; the plot comparing the results for the solar cell configurations with the original wing data can be seen in Figure 84. Based on the figure, it is clear that the addition of solar cells did not significantly affect the collection of volume by the Mylar-based wing films; all of the configurations move similarly to the original design. However, the 2x5 solar cell configuration experienced a larger overall volume change, as it completely flattened out during the transition from down-flap to up-flap. Thus, the addition of a solar cell along the leading spar forces wing F to completely flatten out during the transition, forcing all air out of the wing during flapping.

5.2.2 Wing E Results

Figure 85 compares the lift and thrust results for the four different solar cell configurations with the original results for wing E. Unlike the results for wing F, the values for the solar cell configurations were much more similar to the original data; all of the thrust values were within five grams, while the lift values were all within ten grams. Because the optimal position is in the upper right quadrant, the wing with the 7x3 solar cell configuration performed the best of the solar cells; however, the other configurations were not significantly worse, as in the case of wing F. The addition of solar cells on the wing E configuration did not have a large negative effect on wing lift and thrust forces.
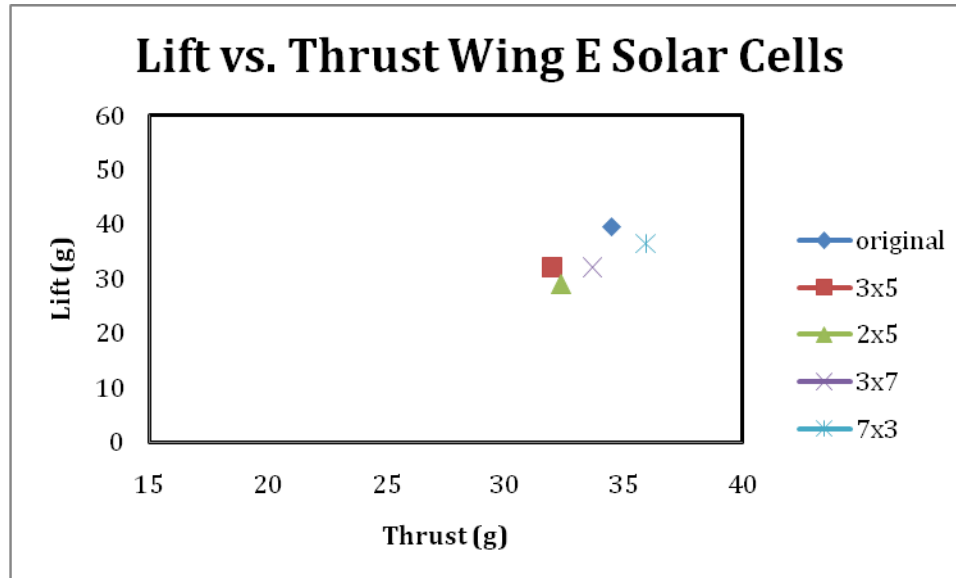
Figure 85 Lift vs. thrust for solar cells on wing E

The motion of the leading spar was also considered for wing E for all four solar cell configurations. Plots comparing the results for the different configurations with the original results for both the head-on and over-top perspectives can be seen in Figure 86 and Figure 87, respectively.

The ideal shape for the motion of the leading spar from the head-on perspective is a parallelogram; although none of the configurations exactly approximate a parallelogram, all of the configurations follow the path of the leading spar on the original wing configuration with the exception of the 2x5 solar cell configuration. Because this configuration places a solar cell right along the leading spar, the compliance of the area around the leading spar was reduced, affecting how the spar moved. Thus, the deviation from the original path accurately reflects the change in compliance introduced by the solar cell placement.
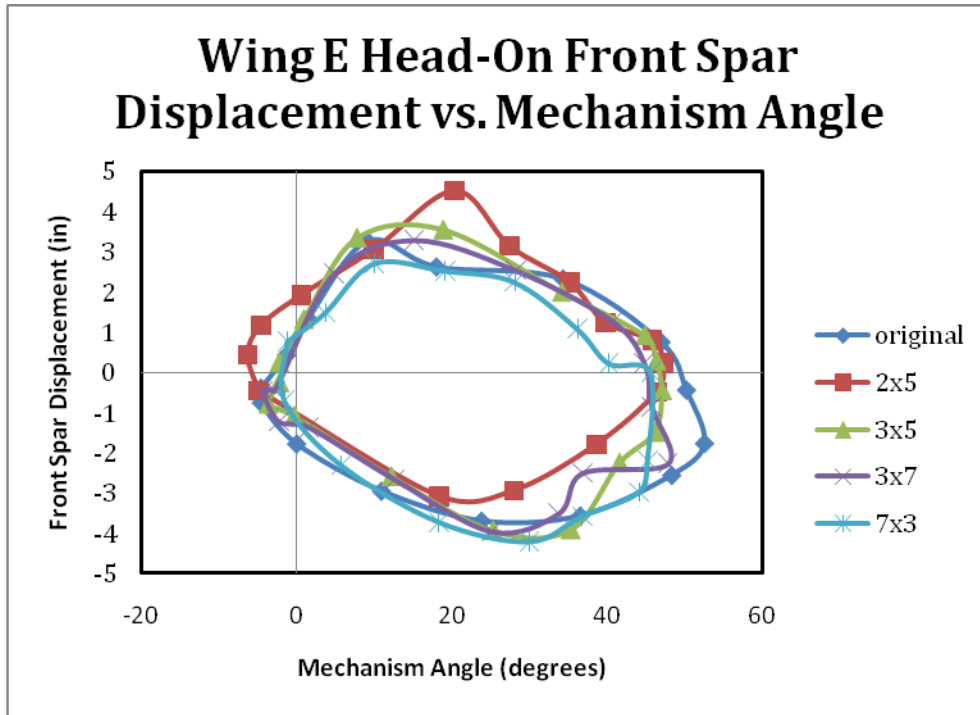
Figure 86 Leading spar head-on displacement (Wing E w/solar cells)
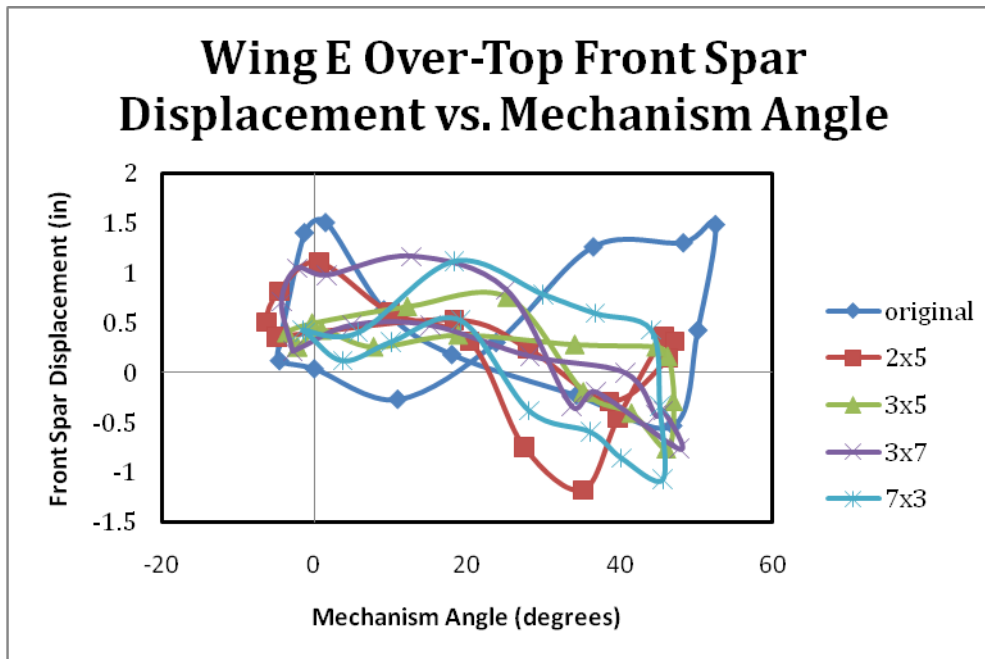
Figure 87 Leading spar over-top displacement (Wing E w/solar cells)

For the over-top perspective, the ideal motion of the leading spar most closely approximates a bowties, as seen in Figure 87 by the black dotted line. Although the original wing E configuration did not quite resemble the ideal bowtie, it was possible that the addition of solar cells would change the compliance in the wing in such a way that the movement of the leading spar would improve; this was not the case. Much like the addition of solar cells to the wing F configuration, the addition of solar cells to wing E altered compliance in such a way that all four configurations saw a restriction in motion of the leading spar in the plane.

The movement of both horizontal and vertical centroid location was also considered for the wings with the solar cell configurations. The progression of the horizontal centroid location through the flap cycle can be seen in Figure 88. As previously stated, the ideal centroid location should move away from the center spar during the up-flap and towards the center spar during the down-flap for the horizontal values; the addition of solar cells to wing E caused skewed results. While the 3x5 and 7x3 solar cell configurations seem to generally follow this trend, the 2x5 and 3x7 configurations move away from the center spar during both the up-flap and down-flap, moving toward the center spar only during the transition from up-flap to down-flap. The 3x7 configuration behaved this way because it is the largest solar cell added, and thus greatly reduces compliance; the 2x5 solar cell, however, is one of the smallest, so the location along the leading spar significantly changed the wing behavior.
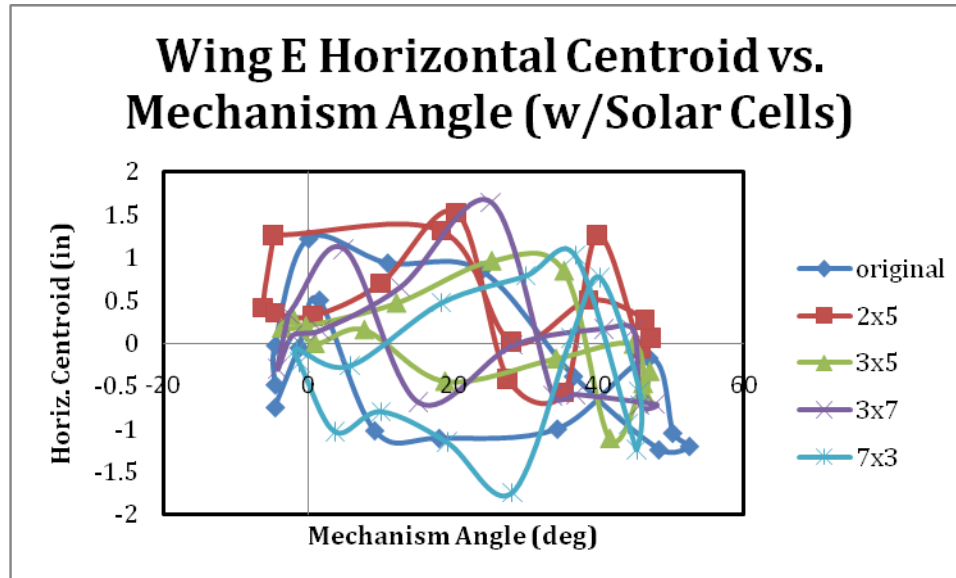
Figure 88 Horizontal centroid progression (Wing E w/solar cells)

For the vertical centroid progression, the ideal centroid location should move away from the leading spar during the up-flap and towards the leading spar during the down-flap. The resulting plot for the wing E configuration with solar cells can be seen in Figure 89. As seen in the figure, the vertical centroid progression for all of the wing configurations, including the original construction, are not ideal; however, the 7x3 solar cell configuration most closely approximates the ideal of all the wing E results. Thus, the addition of the 7x3 solar cell improved the movement of the vertical centroid location.
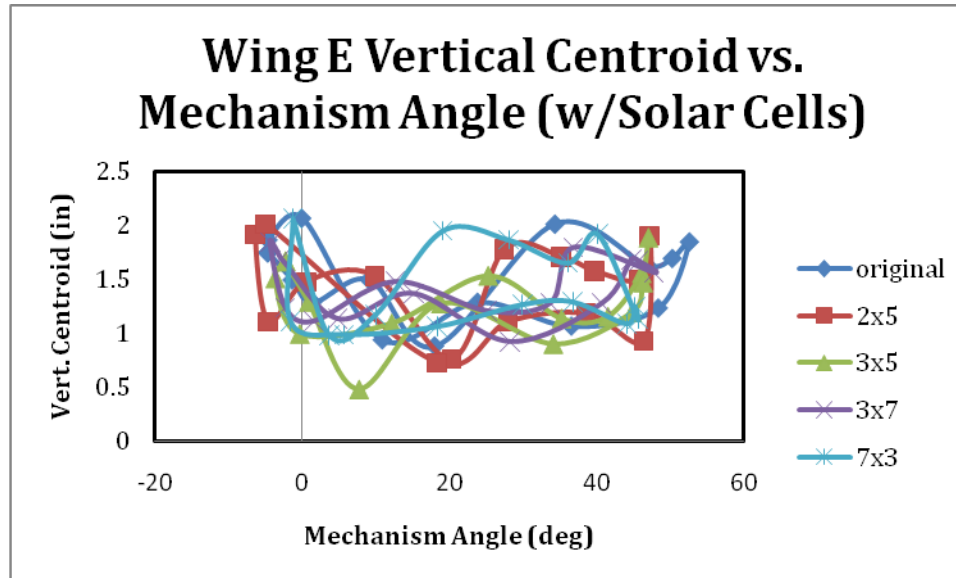
Figure 89 Vertical centroid progression (Wing E w/solar cells)

The final calculation considered for the wing E configuration with the addition of solar cells was volume. The plot showing the resulting volumes for the solar cell configurations in comparison with the original data for the wing can be seen in Figure 90. Based on the figure, the 3x7 and 7x3 configurations follow the same progression as the original data for wing E; however, the 3x5 and 2x5 configurations capture more volume at the top of the flap cycle and the 2x5 configuration captures significantly less volume during the down-flap. So, the addition of solar cells to the wing E design can positively affect the amount of volume collected and displaced.
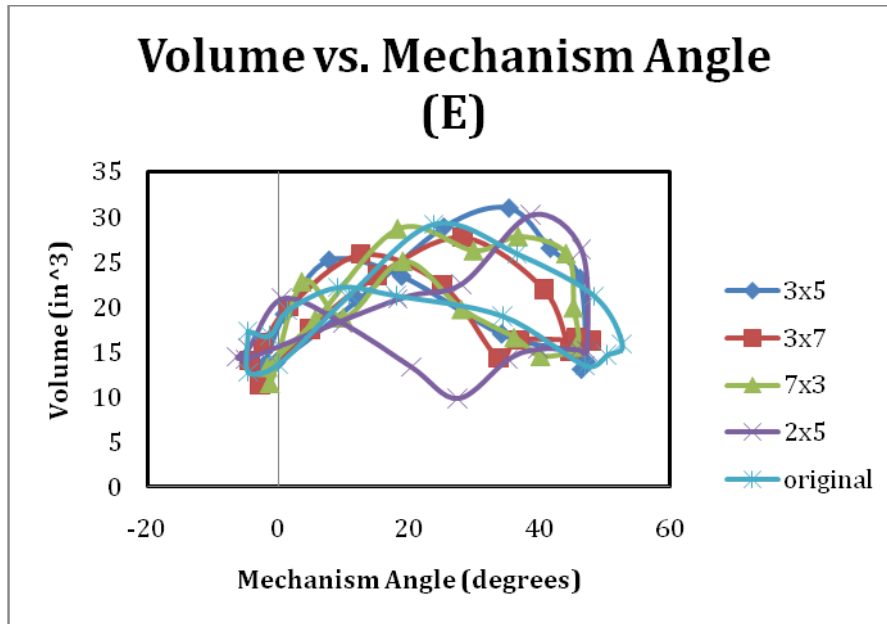
Figure 90 Volume progression through flap cycle (Wing F w/ solar cells)

5.3   Wing Imaging

5.3.1   Wing F Imaging

Figure 91-Figure 94 show measured imaging for wing F with the four different solar cell configurations. The original wing F design measured imaging can be seen in Figure 60 in chapter 4. In comparing Figure 91-Figure 94 with Figure 60, there is not a significant difference in the images. All five of the up-flaps and down-flaps create smooth, bowl-like structures with few ripples or bubbles, indicating a smooth wing surface throughout the flap cycle. The only difference lies in the z-displacement; the original data has a larger highest z-value, indicating the wing traveled further up during the cycle, capturing and displacing more volume than the four solar cell configurations, accounting for the significant difference in lift and thrust values.

117
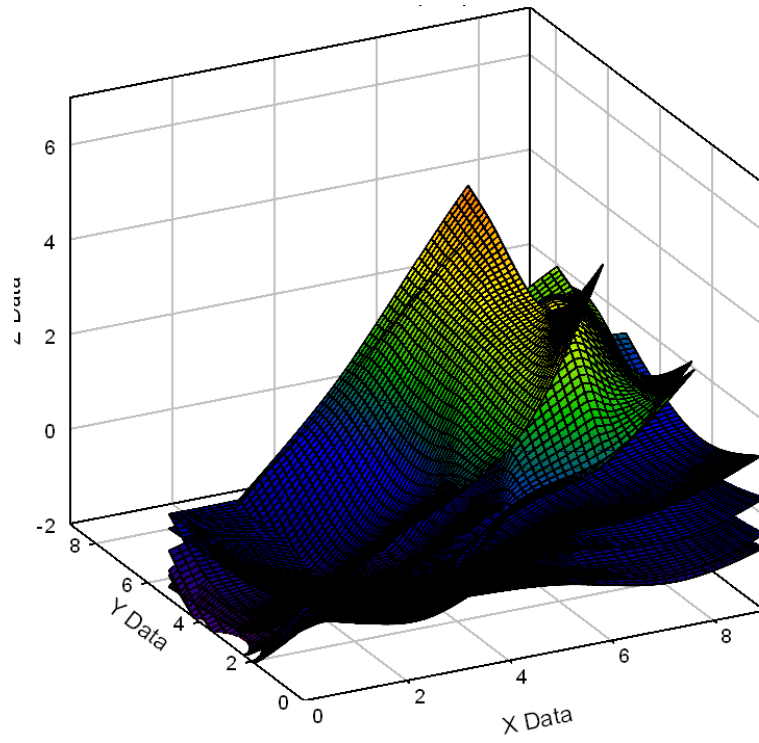
(a)
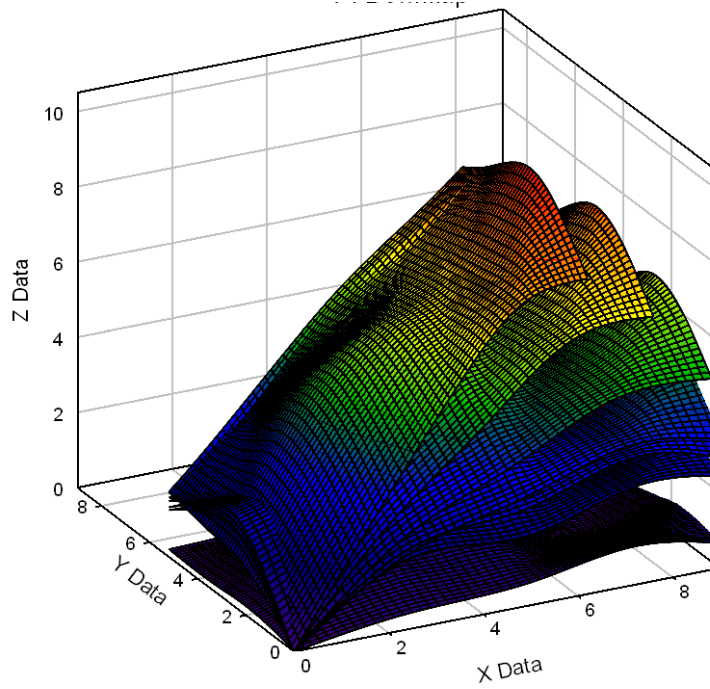
(b)

Figure 91 Wing F with 7x3 solar cells up-flap (a) and down-flap (b) imaging
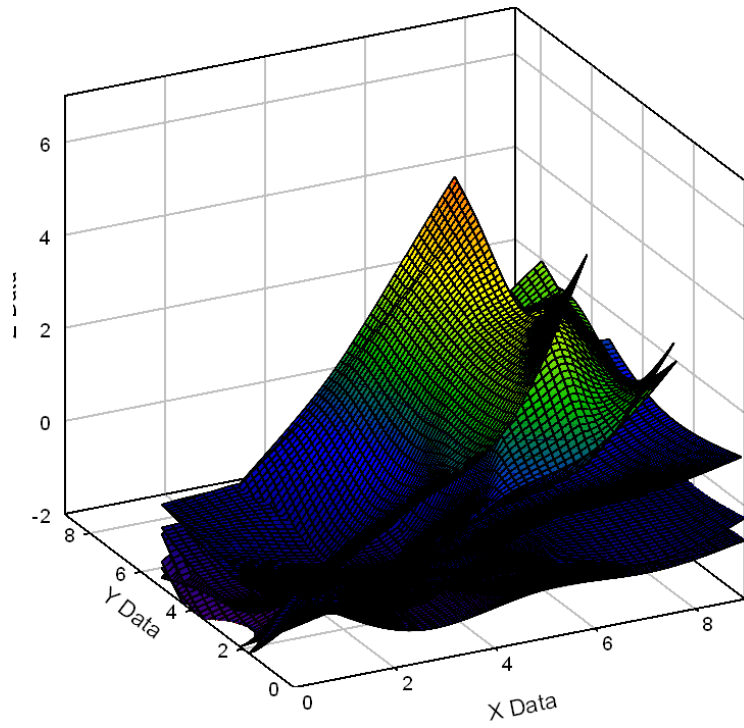
(a)
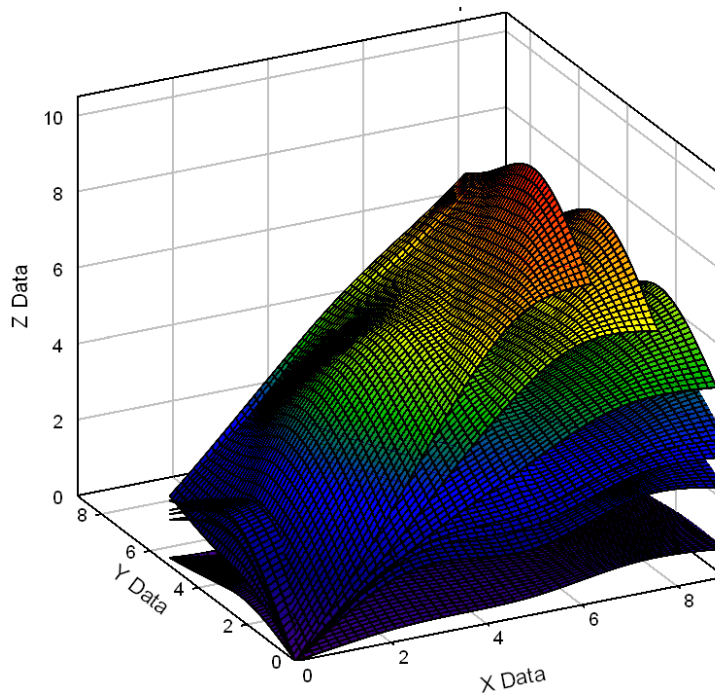
(b)

Figure 92 Wing F with 2x5 solar cells up-flap (a) and down-flap (b) imaging
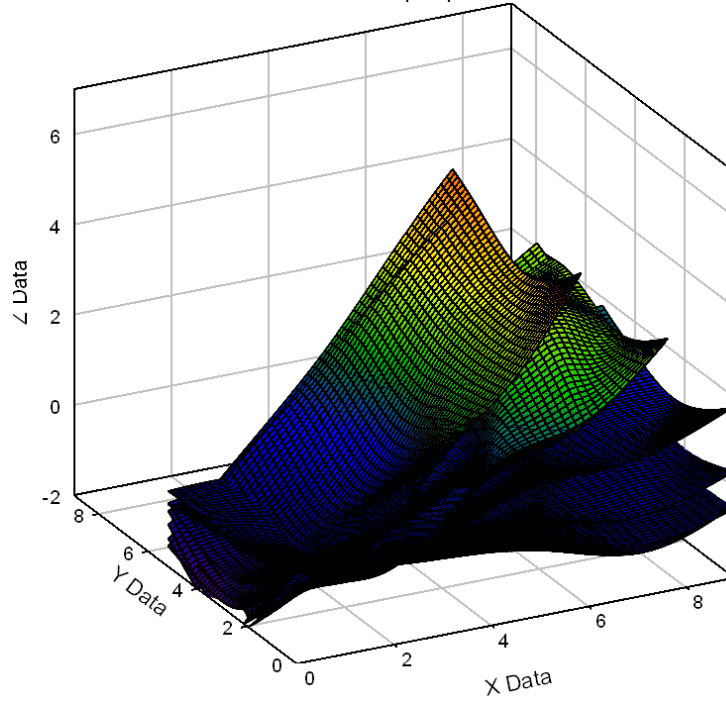
(a)
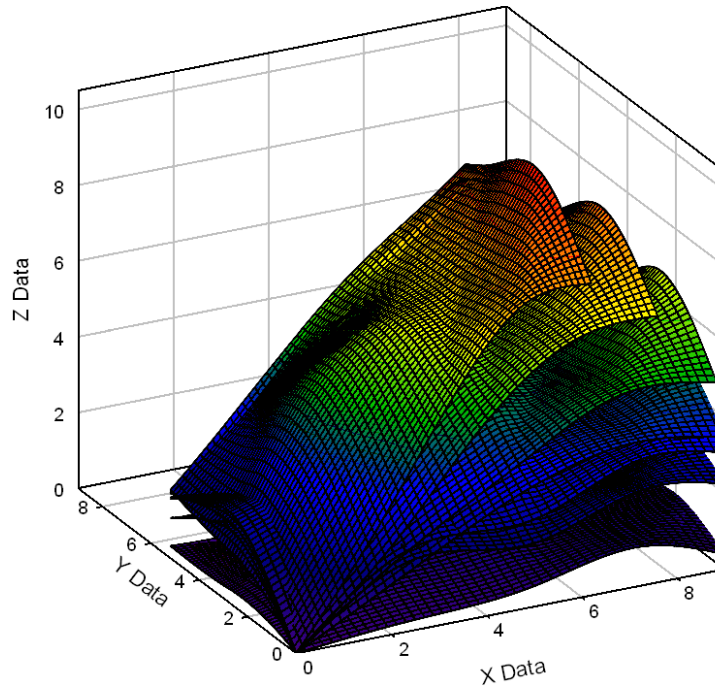
(b)

Figure 93 Wing F with 3x5 solar cells up-flap (a) and down-flap (b) imaging
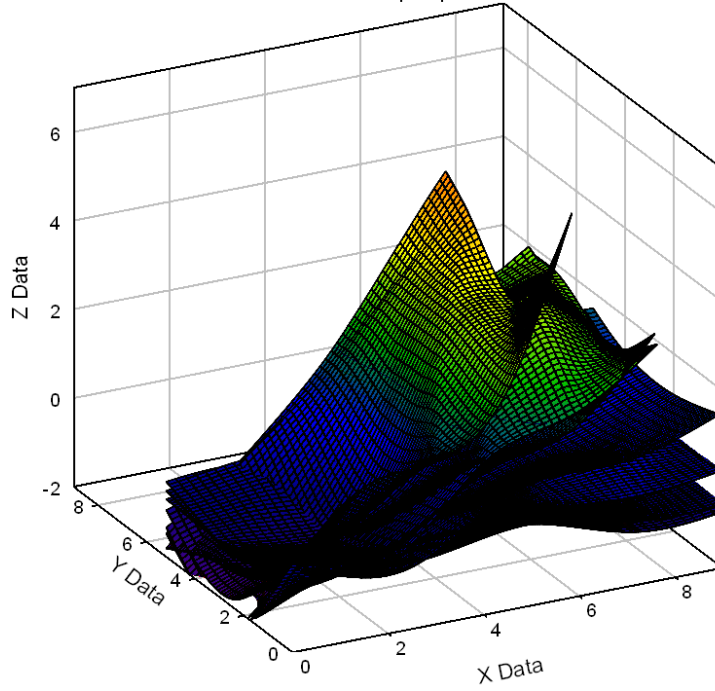
(a)
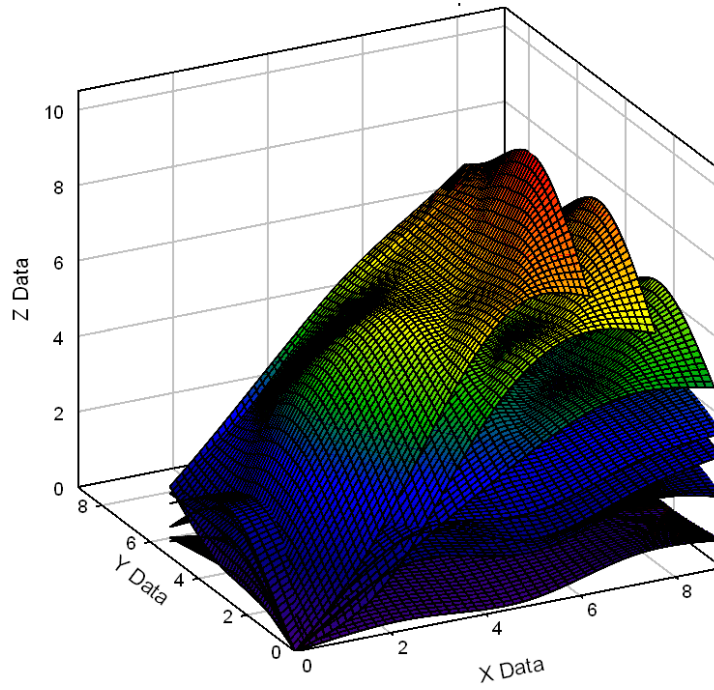
(b)

Figure 94 Wing F with 3x7 solar cells up-flap (a) and down-flap (b) imaging

5.3.2   Wing E Imaging

Figure 95-Figure 98 show the measured imaging for the four different solar cell configurations for the wing E design. The measured imaging for the original construction can be seen in Figure 59 in chapter 4. In comparing the original imaging with the four figures seen below, the plots are very similar; while the ideal shape is a concave bowl-like structure during the up-flap that deepens towards the top of the cycle, and a convex bowl-like structure during the down flap that flattens out towards the bottom of the cycle, wing E, both with and without solar cells, does not have significant curvature in either the up-flap or down-flap and has some rippling in the shapes. However, the maximum values in z-displacement in the solar cell configurations were slightly higher than the values in the original wing design. The similarities in the imaging reinforce the similarities found in the lift and thrust values.
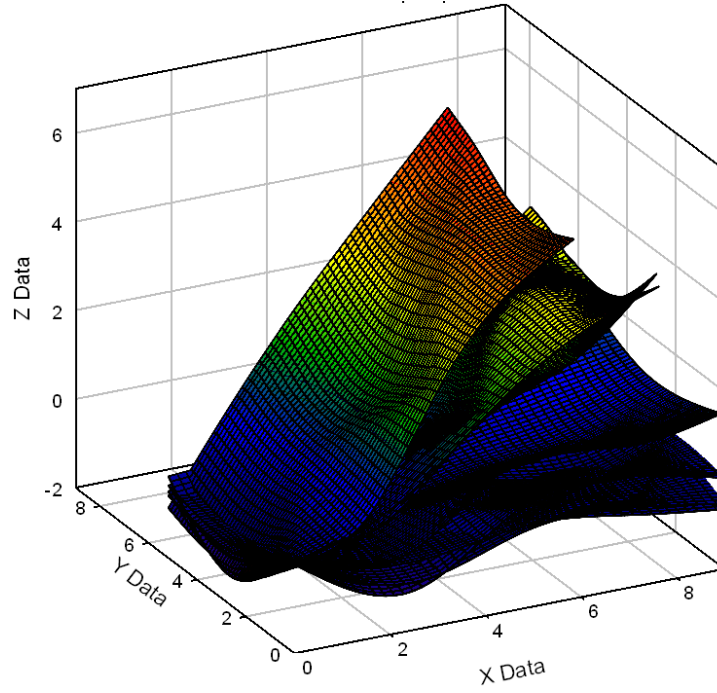
(a)
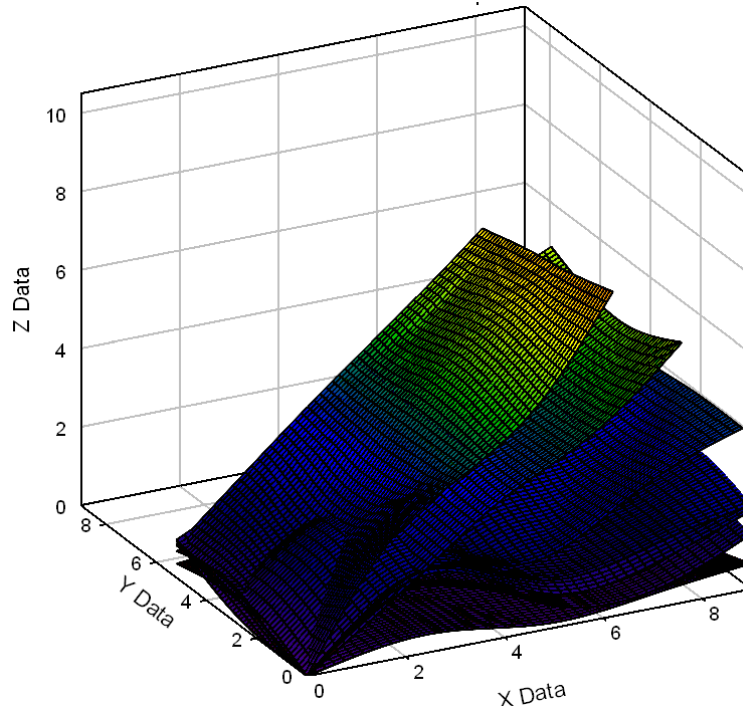
(b)

Figure 95 Wing E with 7x3 solar cells up-flap (a) and down-flap (b) imaging
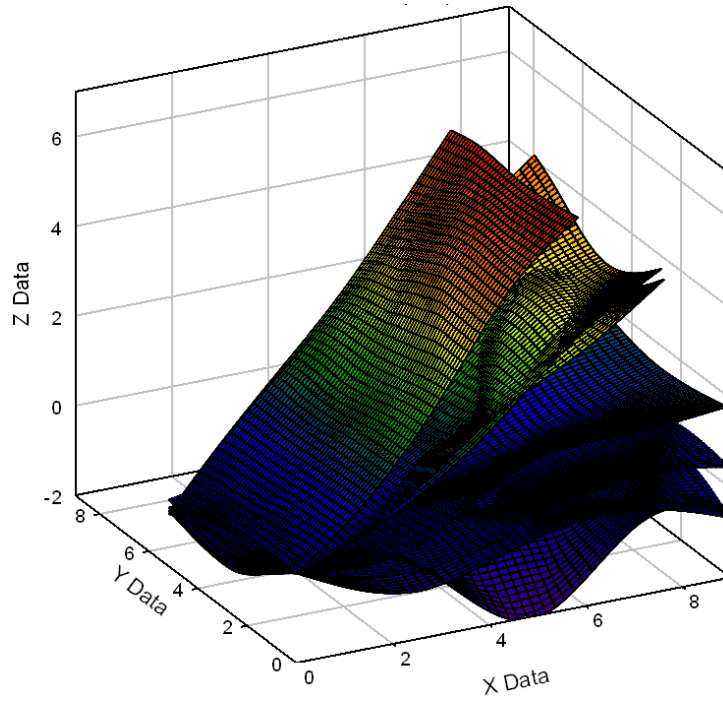
(a)
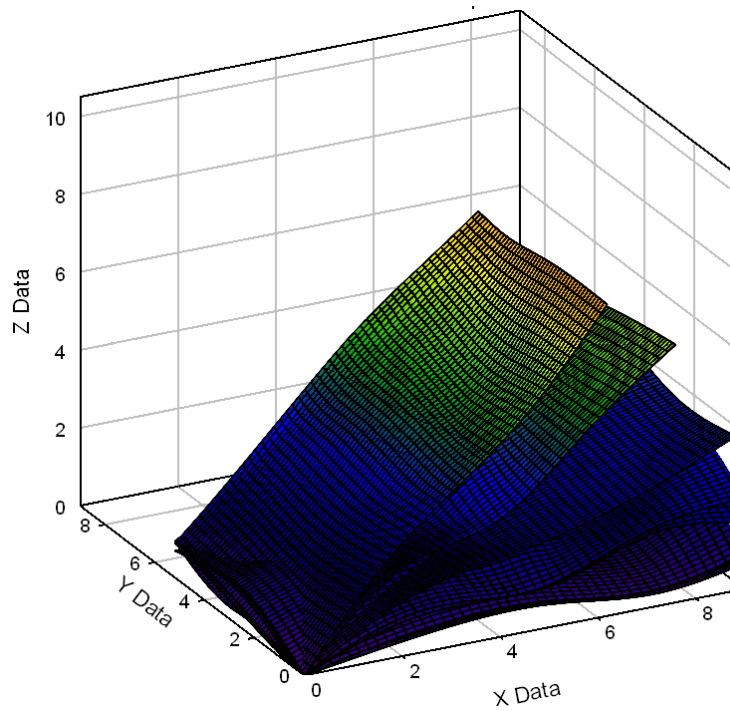
(b)

Figure 96 Wing E with 2x5 solar cells up-flap (a) and down-flap (b) imaging
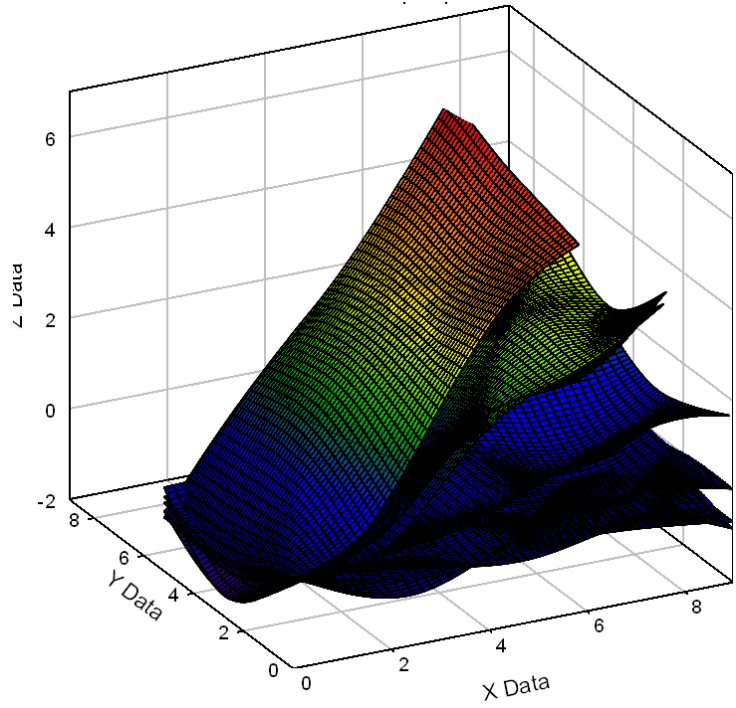
(a)
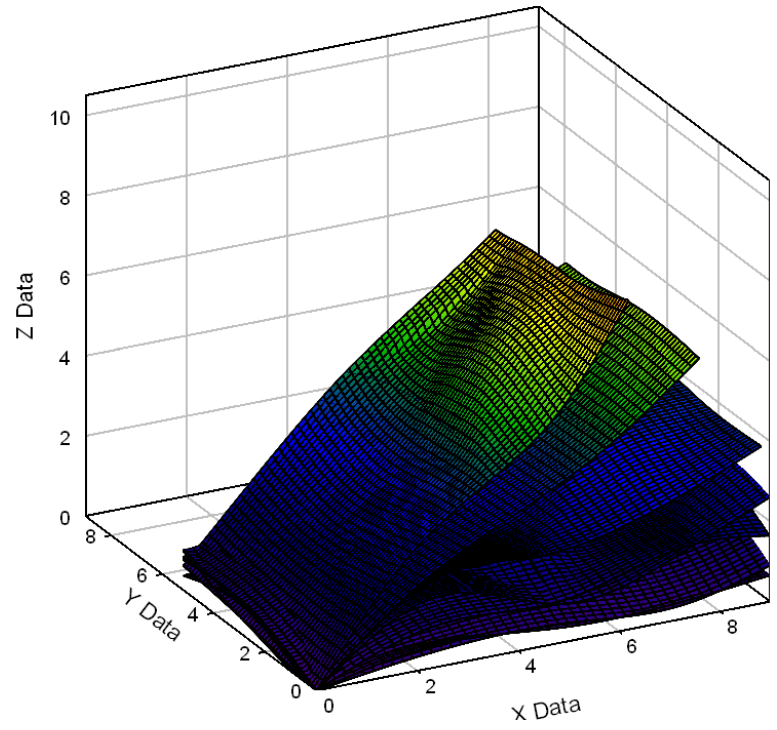
(b)

Figure 97 Wing E with 3x5 solar cells up-flap (a) and down-flap (b) imaging
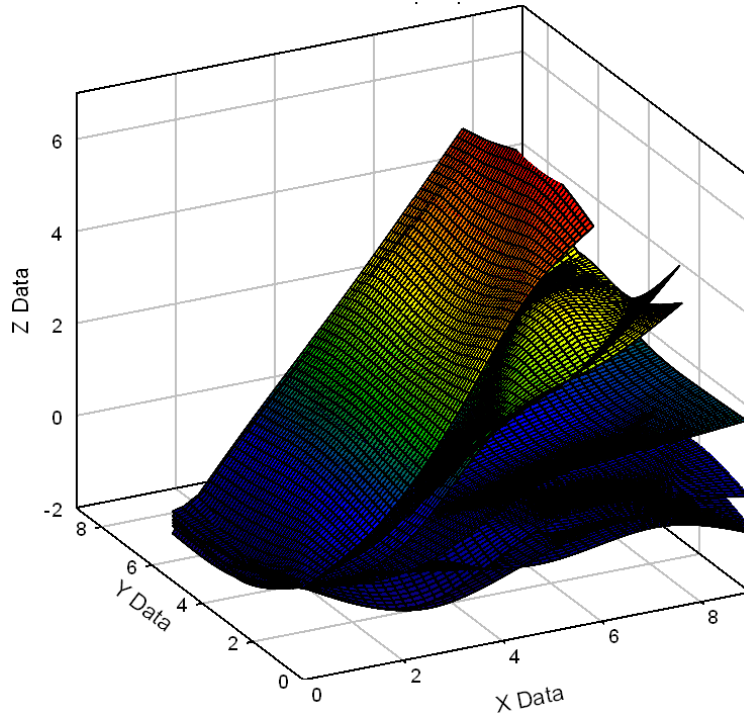
(a)
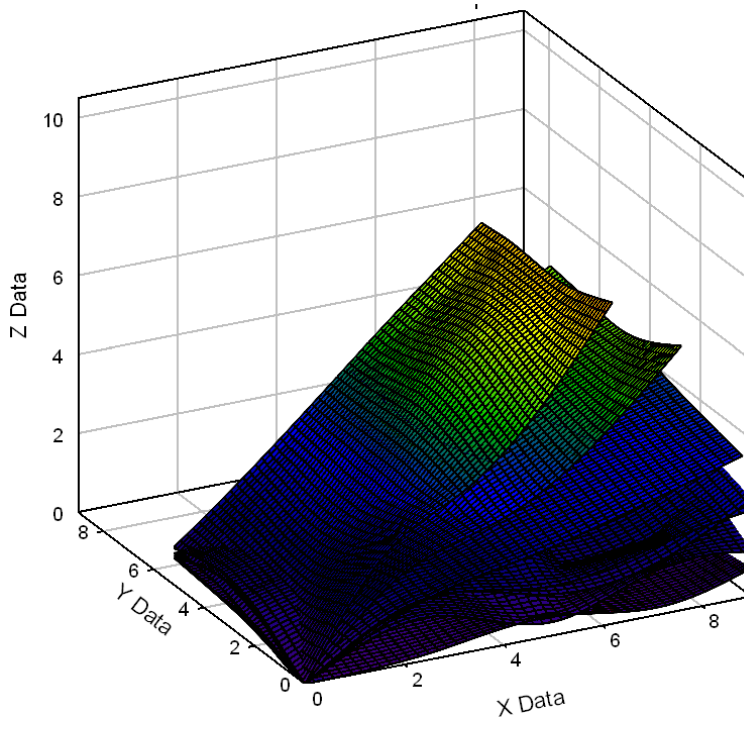
(b)

Figure 98 Wing E with 3x7 solar cells up-flap (a) and down-flap (b) imaging

5.4   Summary

In this chapter, the integration of solar cells into the flexible flapping wing structures of the 'Jumbo Bird' MAV was introduced. The motivation behind this integration, which is multi-functional capability and the improvement of time-in-flight and/or payload capacity, was discussed, and the types of solar cells used were presented. The locations of the solar cells on the wings were selected, and the reasoning behind the configurations selected was discussed. The wing characterization method developed in chapter four was then implemented on four solar cell configurations for two different wing constructions, wings E and F. The results of the wing characterizations were then presented. Based on the results gleaned from the wing characterization method, the addition of solar cells on wing F did not result in improved flight performance. The lift and thrust forces generated were smaller than those generated by the original wing design, and this negative difference was reflected in the deviations in leading spar movement and centroid location, as well as the smaller magnitudes in the measured imaging results. However, the results presented for wing E indicate potential for an improvement in performance with slight modification in solar cell placement. Because the lift and thrust forces obtained were much more similar than in wing F, and the centroid location as well as volume progression indicate improvements in the wing design with certain solar cell placement, further testing could result in better wing E performance with the addition of solar cells.

Chapter 6:   Multi-functional Performance

6.1   Theoretical Analysis of time-in-flight

MAV performance, which can be quantified through time-in-flight, t_f, or payload capacity, is affected by three main components: the power supplied to the motor, and the thrust and lift forces generated by the flapping wings. Power, lift, and thrust are affected by: (1) the area of the wing, A; (2) the distribution of the stiffness in the wing, φ, which is a function of both carbon fiber spar placement and the solar cell placement, since both affect the compliance; and (3) flapping frequency, f, in Hertz. These relationships, seen in equation 7, were the starting point for the development of the theoretical equation for the time-in-flight. Time-in-flight is a function of power supplied to the motor, P, lift, L, and thrust, T.

$$P(A, \varphi, f)$$
$$T(A, \varphi, f)$$
$$L(A, \varphi, f)$$

$$t_f = f(P, L, T)$$

<div align="right">EQ.7</div>

Time-in-flight can also be written as the energy stored in the platform, U_{stored}, divided by the average power expended by the platform over time, $P_{expended}$. The energy stored in the MAV platform equipped with solar cells is the sum of the energy stored in the batteries, $U_{battery}$, and the power provided by the solar cells, $P_{solarcell}$ for the time-in-flight. Equation 7 then becomes:

$$t_f = \frac{U_{stored}}{\overline{P}_{exp\,ended}} = \frac{U_{battery} + P_{solarcell} t_f}{\overline{P}_{exp\,ended}}$$

<div align="right">EQ.8</div>

The expended average power is a function of the amount of work done by the motor. This work is affected by two coupled factors: the thrust produced by the wings and the velocity at which the MAV is flying. Assuming constant velocity, the only variable in power is the thrust. Mueller et. al. [53] determined that the thrust in compliant wings is proportional to the squared frequency value at which the wings are flapped; his results are shown in Figure 99.
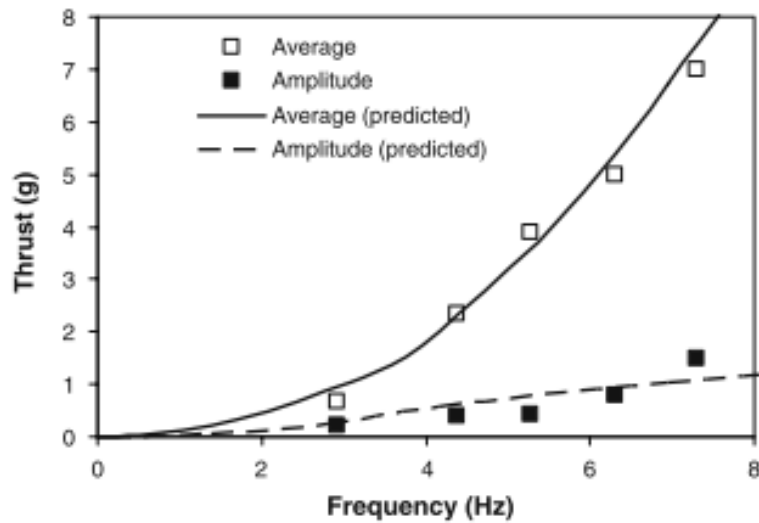
Figure 99 Thrust vs. Frequency for compliant flapping wings [53]

Based on Mueller's findings, the average power expended by the platform, defined by equation 9, is equal to the thrust produced by the wings at the flapping frequency, T, multiplied by the flapping frequency, f, and a proportionality constant, k. The proportionality constant must be calculated for each different wing set using equation 10, as it changes based on the flapping frequency and the corresponding thrust value. The resulting time-in-flight equation is described by equation 11.

$$P = kTf \qquad \text{EQ.9}$$

$$k = TfP_0 \qquad \text{EQ.10}$$

$$t_f = \frac{U_{battery} + P_{solarcell}t_f}{kTf} \qquad \text{EQ.11}$$

where P_0=45W corresponds to the power of the brushless motor.

Rearranging equation 11 results in the following:

$$t_f kTf - P_{solarcell}t_f = U_{battery} \qquad \text{EQ.12}$$

In order to further reduce the equation, a few assumptions must be made. While thrust is not necessarily a constant value throughout a specified flight time, it is assumed constant based on the way the value was experimentally measured. The energy stored in the battery is based on its overall capacity and the average voltage across the pack. The power provided by the solar cells is based on the area of the wing the solar cell covers, while the thrust is based on the area of the wing, its stiffness distribution, φ, and the flapping frequency, f. After rearranging equation 12 to solve for t_f, the final equation for the time-in-flight becomes:

$$t_f = \frac{U_{battery}}{kTf - P_{solarcell}} \qquad \text{EQ.13}$$

6.2   Solar Cell Performance

As stated in chapter 5, four different-sized solar cells were used in solar cell testing; each of the solar cells covered a different amount of area and was rated for different power outputs. A summary of areas and power ratings for the solar cells is listed in Table 3.

Table 3: Solar Cell Data

Solar Cell	Area (in^2)	Power Rating (W)	mA Rating (mA)
2x5	3.9	0.07	25
3x5	5.25	0.06	22
3x7	4.95	0.09	22
7x3	8.97	0.18	50

The rate at which the different solar cells can charge the batteries is an important factor in determining how beneficial the resulting multi-functionality is for the MAV platforms. In order for the multi-functional aspect to be beneficial, the charging must occur at a rate at which the charging-to-flight time ratio is not significantly different. The largest battery pack used in the 'Jumbo Bird' MAV contained three 300 mAh batteries, giving a total capacity of 900 mAh. Since each solar cell is rated for a different mA value, the time to charge the batteries depends on the solar cell chosen. Based on the configurations tested in chapter 5, two of each of the solar cells were used, giving twice the milli-amperes during charging. To calculate the charge time, the battery capacity, 900 mAh, was divided by the doubled mA rating for the solar cell. Table 4 shows the resulting charge times.

Table 4: Solar cell charging time

Solar cell	Charge time
2x5	18 hours
3x5	20.45 hours
3x7	20.45 hours
7x3	9 hours

Based on the results in Table 4, the 7x3 solar cells provided the fastest charging time based on the battery pack size, which was also explained by the larger area covered

by the solar cell. If the 7x3 solar cells were to cover fifty percent of the wing surface, the battery pack would theoretically be able to charge in 3 hours, and with 75% of the wings covered, the battery pack would charge in 1.8 hours; the resulting ratio of charge time to flight time is 3.6:1. Thus, the larger area of the wing covered by solar cells, and the larger milli-ampere rating possessed by the solar cells, the faster the solar cells are able to charge the battery pack.

6.3 Experimental Prediction of t_f

Experimental predictions for time-in-flight can be generated using equation 13 determined in section 6.1. Based on this equation, six quantities must be known in order to solve for time-in-flight: the energy stored in the batteries, the thrust characteristics based on the solar cell area and the cell distribution , the flapping frequency of the MAV, the power generated by the solar cell based on the area covered, and the proportionality constant, k. The thrust values were measured for all the wing sets at the maximum flapping frequency of 6.1 Hz, both with the different solar cell configurations and without the solar cells. The results of these measurements were discussed in chapters 4 and 5. The power ratings for the solar cells were listed in Table 2 of section 6.2. The energy stored in the battery pack, the largest of which contained three 300mAh batteries wired in series, was calculated by multiplying the capacity (0.3Ah) by the average voltage, which was 11.1V (three 3.7V batteries wired in series). The energy stored in the battery pack was therefore 12 kJ. Finally, the flapping frequency for the original wing sets at the thrust values comparable to the values produced by the solar cell wings had to be determined, so the time-in-flight values can be compared. The power consumed by the motor is proportional to the thrust at a certain flapping frequency multiplied by that

flapping frequency, thus the flapping frequency at the average maximum thrust value

produced by the solar cells on each wing type must be calculated. Because thrust is a

function of the value of flapping frequency squared, the flapping frequency can be

determined by comparing the second order polynomial variations of the original wing

thrust and the thrust produced by the wing with solar cells. The frequency that occurs at

the intersection of the average maximum thrust value for the solar cells and the original

data best-fit line was the flapping frequency. Figure 100 and Figure 101 show the plots

of thrust versus flapping frequency for the wing F and wing E configurations,

respectively.
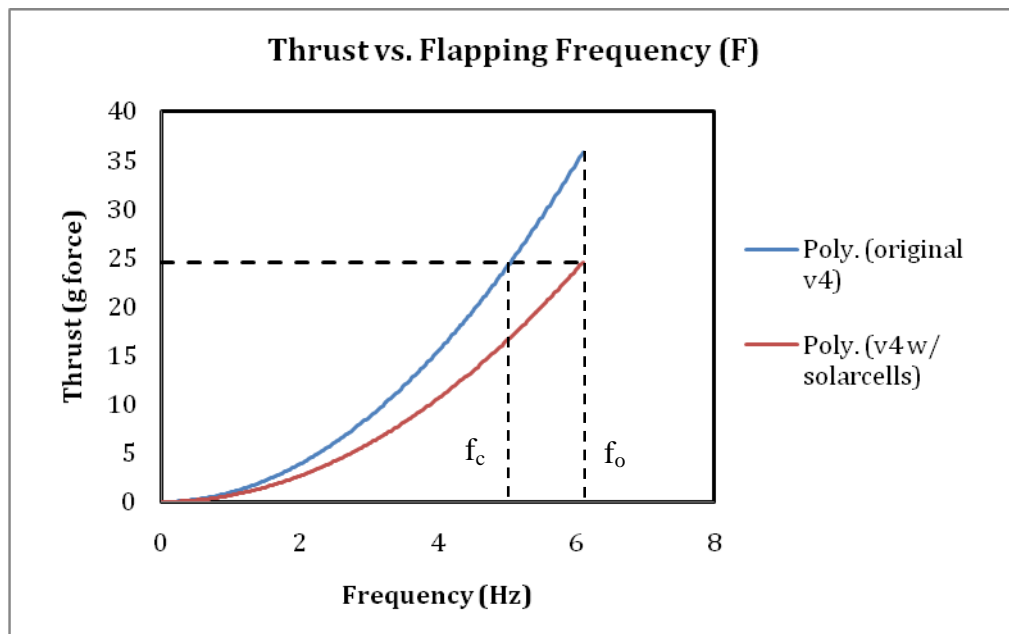
Figure 100 Thrust versus flapping frequency for wing F
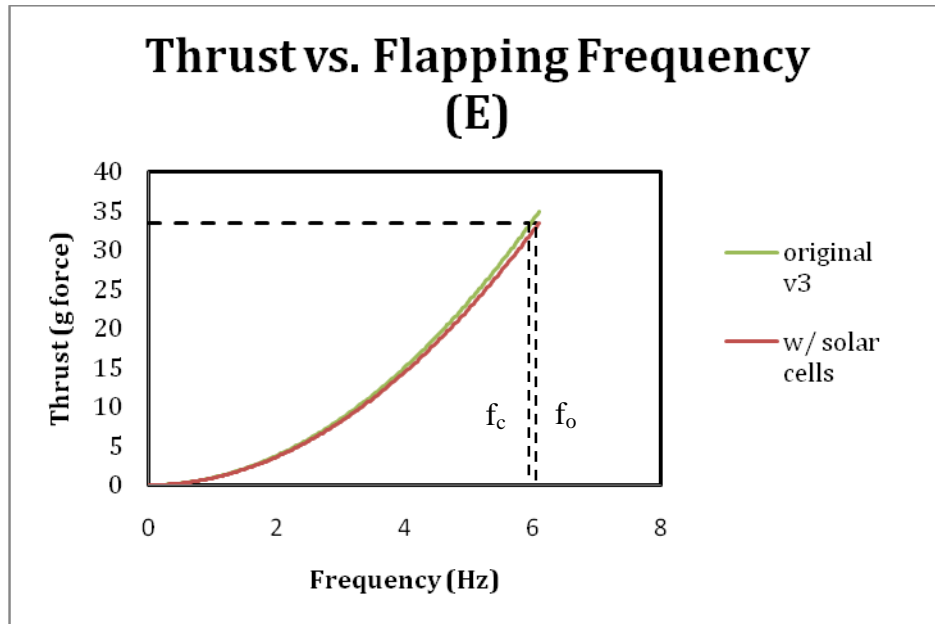
Figure 101 Thrust versus flapping frequency for wing E

From previous two figures, the flapping frequency for each of the wing configurations was determined by obtaining the flapping frequency at the intersection of the original curve with the dashed line indicating the average thrust value for the wing with solar cells. The flapping frequency required to generate 24.58566 grams force of thrust for wing F was 5.053 Hz, while the flapping frequency required to generate 33.48871 grams force for wing E was 5.975 Hz. Using these values of frequency in the equation determined in section 6.1, time-in-flight was calculated for the original wing sets as well as the wing sets with solar cells. Table 5 compares data for the thrust, flapping frequency, and calculated time-in-flight based on the final equation presented in section 6.1 for the six original wing configurations. Table 6 compares the thrust, flapping frequency, and calculated time-in-flight for the wing F solar cell configurations with the original wing F performance. Table 7 compares the thrust, flapping frequency, and

calculated time-in-flight for the wing E solar cell configurations with the original wing E performance.

Table 5: t_f for original six wing configurations

Wing Design	Thrust (g force)	Frequency (Hz)	Time-in-flight (min)
A	31.044	6.1	13.332
B	24.14146	6.1	13.332
C	36.89729	6.1	13.332
D	31.445	6.1	13.332
E	34.9037	6.1	13.332
F	35.83145	6.1	13.332

Since the power supplied to the motor is the same for each wing, the proportionality constant for each wing set was a different value to obtain that 45 W of power supplied. Thus, the time-in-flight for each of the wing-sets was all the same, at 13.332 minutes, as seen in Table 4. The lack of variation in time-in-flight between the wing-sets was present because other effects, including power loss and lift, are not considered. Also, the significant loss in thrust between the different wing designs was not accounted for in the proportionality constant calculation, so it was not a factor in the overall time-in-flight.

Table 6: Δt_f for wing F solar cell configurations

Wing Design	Thrust (g force)	Frequency (Hz)	Time-in-flight reduction (min)
2x5	23.38158	6.1	9.393
3x5	24.97165	6.1	10.296
3x7	26.5193	6.1	11.049
7x3	23.46566	6.1	9.375
Original F	24.58455	5.053	0

The time-in-flight values presented in Table 5 show that while there was little variation between the different solar cell configurations, the time-in-flight for the solar cell configurations was reduced by 40% when compared with the original wing construction flapping with the same thrust value. This significant difference occurred because the solar cell output, which was only about 1% of the consumption rate, does not recharge the battery fast enough to impact time-in-flight. However, the difference in thrust was large enough that it greatly reduced the time-in-flight for the solar cells, since the thrust was much less for those configurations.

Table 7: Δt_f for wing E solar cell configurations

Wing Design	Thrust (g force)	Frequency (Hz)	Time-in-flight reduction (min)
2x5	32.37054	6.1	0.348
3x5	31.97166	6.1	0.207
3x7	33.67576	6.1	0.876
7x3	35.93688	6.1	1.671
Original E	33.48871	5.975	0

The time-in-flight values for Table 6 show that there was again very little difference between the four solar cell configurations; however, when compared with the original wing configuration, there was only a 5% loss in time in flight for a wing producing a similar thrust value. Like the wing F configurations, the solar cell output was only 1% of the power consumption rate of the motor. Unlike the wing F configurations, however, the solar cell configurations for wing E produces thrust values that were only slightly smaller than the original wing design; thus, the time-in-flight values were only slightly smaller.

Table 8: Comparison solar cell effects on Δt_f for wings E and F

Wing Design	E	F
2x5	4.613	9.393
3x5	4.668	10.296
3x7	4.437	11.049
7x3	4.172	9.375

Table 8 compares the results for time-in-flight between the solar cell configurations and the original values for wings E and F. From this comparison, it can be seen that the solar cell configurations for both sets of wings produced similar time-in-flight values. While the original wing F design produced a significantly higher time-in-flight value than its solar cell configurations, the original wing E design produced only a slightly higher value than its solar cell configurations. This indicates that while the original wing F design outperformed the other wings, implementing solar cells should be done with the wing E design, as the change in thrust was not as detrimental to flight time.

6.4   Design Implications

The experimental values of time-in-flight determined in section 6.3 indicated that the multifunctionality of the wing was not a factor in the results. The changes in thrust, not the power output of the solar cells were the major contributor to the differences in time-in-flight. Thus, a model must be developed that relates the power output of the solar cells to the time-in-flight, allowing for the effectiveness of different MAV designs to be analyzed. Time-in-flight is proportional to the energy stored in the system divided by the energy expended by the system. The energy stored in the system, U, is assumed to be the power required, P_o, and the time-of-flight of the system, t_{f_o}, without the addition of solar cells, as seen in equation 14. The power required without the addition of solar cells is

determined using the thrust-frequency curves, from which the appropriate frequency is found for the corresponding thrust. The found thrust and frequency are then used to get power.

$$U = t_{f\_o} P_o$$ EQ.14

The energy expended by the system is the difference between the power needed by the system with solar cells incorporated, P_s, and the power supplied by the solar cells themselves, S. P_s is determined in equation 15, through multiplying the power required for the system without the addition of solar cells with a multi-functional criterion, k.

$$P_s = kP_o$$ EQ.15

Equation 8 in section 6.1 describes time-in-flight as the stored energy divided by the energy expended. Using equations 14 and 15 in equation 8, equation 16 describes time-in-flight reduction, t_f, with respect to multi-functional design.

$$t_f = \frac{U}{P_s - S} = \frac{t_{f\_o} P_o}{kP_o - S} = \frac{t_{f\_o}}{k - S/P_o}$$ EQ.16

From equation 16, it can be determined that the multi-functional criterion, k, is related to the power output of the solar cells through power relationships. Equation 17 defines parameters of equation 16.

$$k \geq 1$$

$$infinite\ t_f\ when\ k = S/P_o$$ EQ.17

The multi-functional criterion, k, defines how the design of MAVs with solar cells should be approached. In order for the solar cells to be effective when implemented in MAVs, k must be kept as close as possible to one, as this means that the power supplied by the solar cells is as close as possible to the power required for flight without solar

cells. In the ideal configuration, S would be greater than P_o, meaning that the solar cells supply more power than necessary for flight. If P_o is significantly greater than S, the integration of solar cells is unnecessary, as it would not increase time-of-flight.

The power required by the MAV without the addition of solar cells is affected by the mass of the MAV as well as the wingspan of the MAV. Pines et. al. compared the weight of current flying apparatuses, both biological and manmade across the size spectrum, with the cruising speed of the apparatuses; it is evident from this plot, seen in Figure 102, that as weight increases, cruising speed increases. Since power can be described as drag force multiplied by velocity, and drag force is proportional to the squared value of velocity, if Figure 102 were to be converted to a comparison of weight and power required for cruising, the slope of the curve would be significantly steeper.
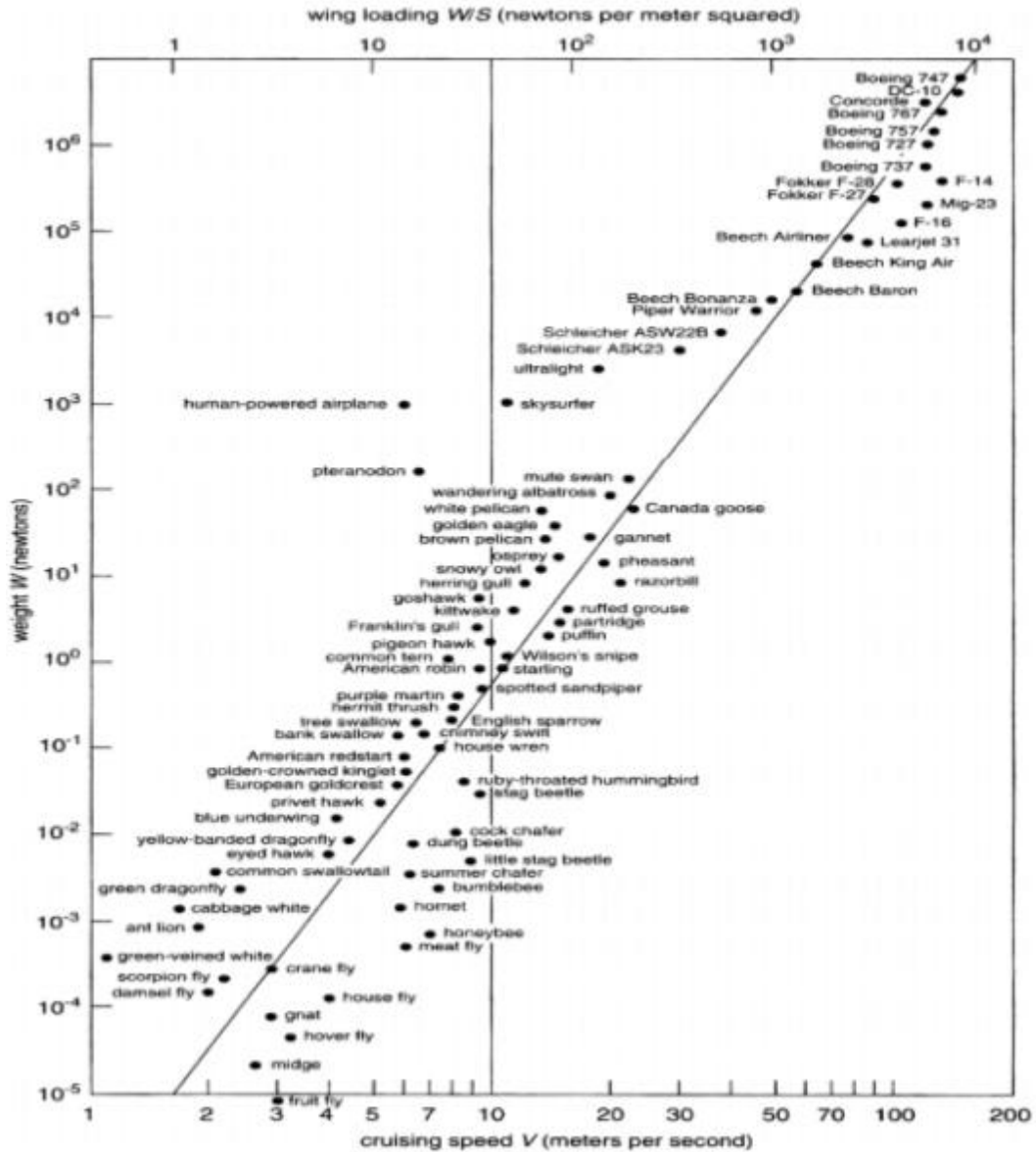
Figure 102 Great flight diagram [54]

The wingspan, or area of the wing, also affects the power required of the MAV. As the mass of the MAV increases, the wingspan must increase to carry the extra mass. However, the wing area does not increase with mass as quickly as power does; thus, mass has a greater effect on required power than overall wing area. Pines et. al. developed a comparison between weight and wingspan of MAVs as well; it is seen in Figure 103.
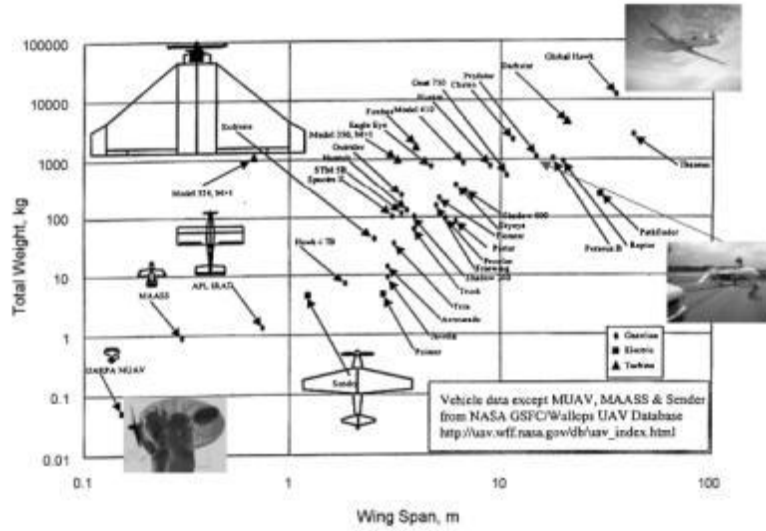
Figure 103 Comparison between MAV wingspan and total weight [54]

While wingspan is a method of comparing wing size, wing area is a better choice when dealing with multifunctional applications, as the area of the solar cells affects compliance and efficiency. The three MAVs built at University of Maryland are compared based on mass, wing area, and power in Figure 104.
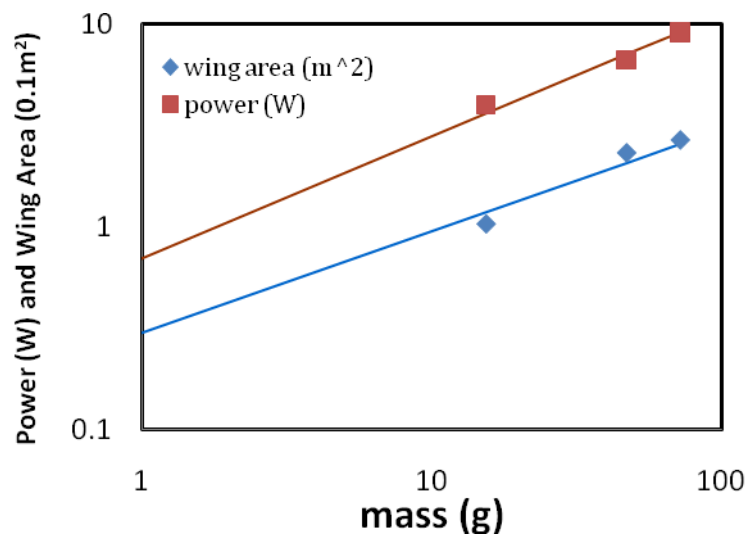
Figure 104 Comparison of power and wing area versus mass for UMD MAVs

The area of the wingspan covered by the solar cells and the efficiency of the solar cells used are also a significant factor in determining the multi-functional capabilities of an MAV platform. As seen in the previous section, if the solar cells do not supply power at a similar rate that power is expended, the addition of those solar cells is unnecessary. Also, adding solar cells affects the compliance of the wing itself; if the wings with solar cells do not generate enough lift and thrust, their addition is again unnecessary. Because the solar cells used in this thesis do not generate power at the same level that the 'Jumbo Bird' MAV consumes power, the solar cells were ineffective; however, if the same solar cells were used on one of the smaller MAVs built in the same lab, the effectiveness of the solar cells would be improved, since the power consumed is much closer to the amount of power generated by the cells.

The power contributed by the solar cells S, is a function of the area of the wings, A, the percentage of the wing covered by the solar cells, n, the power flux of the sun, Q, and the conversion efficiency, c. This relationship is shown in equation 18.

$$S = ncQA$$ EQ.18

The power flux of the sun, Q, is commonly defined as 100 mW/cm^2, and the typical conversion efficiency for solar cells is 30%. In equation 17, infinite time-in-flight was achieved when the multifunctional criterion k was equal to the power from the solar cells divided by the power consumed by the MAV with no solar cells, known as k_c. or k critical. Using this equation, the critical multifunctional criterion can be evaluated based on two governing factors, the wing area and the power consumed by the MAV, both of which vary with MAV mass. From Figure 104, the relationship between mass and wing

area as well as the relationship between mass and power were determined to obtain

equation 19, which obtained k_c based on current University of Maryland MAV platforms:

$$k_c = \frac{S}{P_o} = \frac{cQA(m)}{P_o(m)}$$

EQ.19

Since the values of Q and c were known, and values of A and P_o were calculated

based on the equations gleaned from Figure 104, a comparison between the

multifunctional criterion, k, and the mass of the MAV, m, was made in Figure 105.
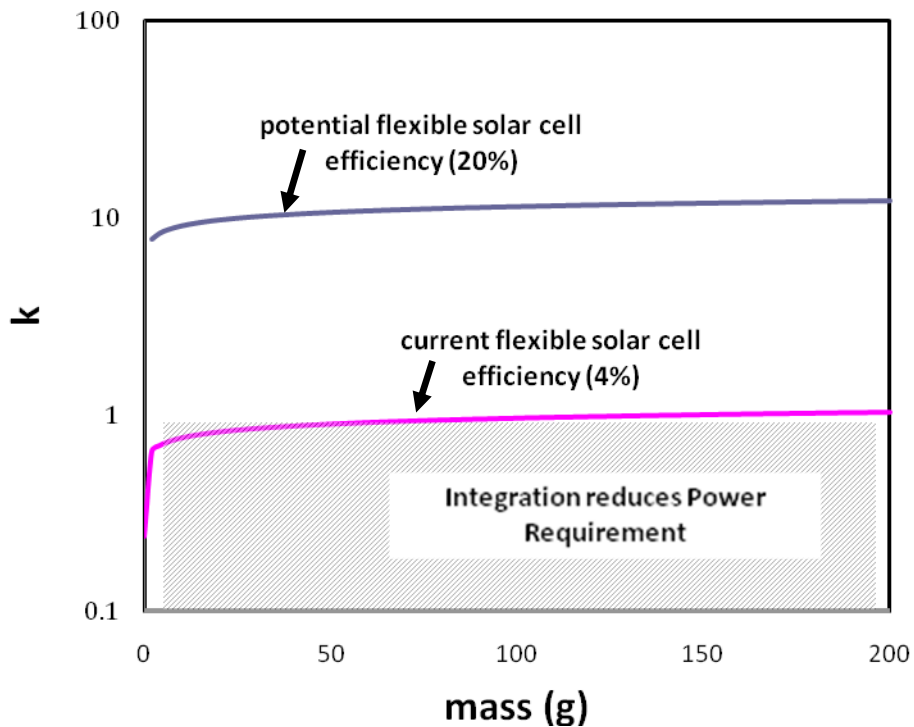
Figure 105 Comparison of k_c and MAV mass for UMD MAVs

As seen in Figure 105, as the MAV mass increases, the multifunctional criterion

increases and plateaus, indicating that the power produced by the solar cells must be

approximately equal to the power required by the MAV without solar cells at higher

values of mass. When the multifunctional criterion is one, the maximum mass for infinite

time-in-flight for the given MAV power requirements has been reached; should the

multifunctional criterion be less than one, the MAV requires less power, so batteries can

be removed or the motor size can be decreased. Should the UMD MAVs be made more

efficient, the curve comparing k_c will shift right, increasing the maximum mass values for

the MAV. Factors such as solar cell size, solar cell efficiency, and the percentage of the

wing covered will ultimately change the plot seen in Figure 105, as this plot is specific to

UMD MAVs and full wing coverage with solar cells.

The overall goal of adding solar cells is to increase the endurance of MAVs

without significantly affecting performance. Pines et. al. [54] developed a comparison of

current MAV weights and endurance times; while the current MAVs cover a large range

of weight values, the effective implementation of solar cells could effectively take the

three boxed planes in Figure 106 and significantly shift them left.
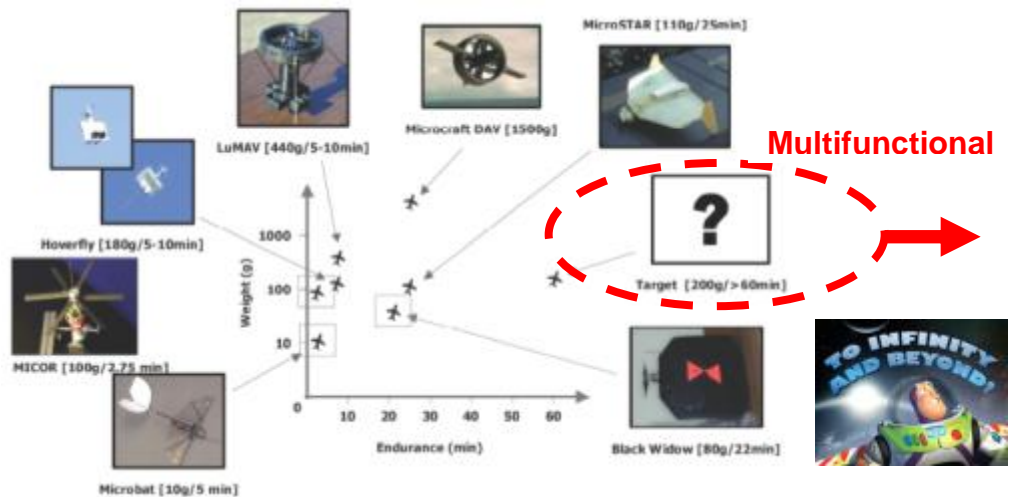
Figure 106 Endurance or hover time of current MAVs [54]

Solar cells were effectively integrated into the 'Jumbo Bird' MAV at the University of Maryland, as seen in Figure 107. The MAV was successfully flapped with the solar cells and wiring; however, the method of attaching the solar cells stands to be improved. The wires create additional drag, and also lack flexibility, increasing effects on compliance and introducing additional potential connection failures, as the soldered joints are weak in comparison to the forces applied when the wings are flapped.
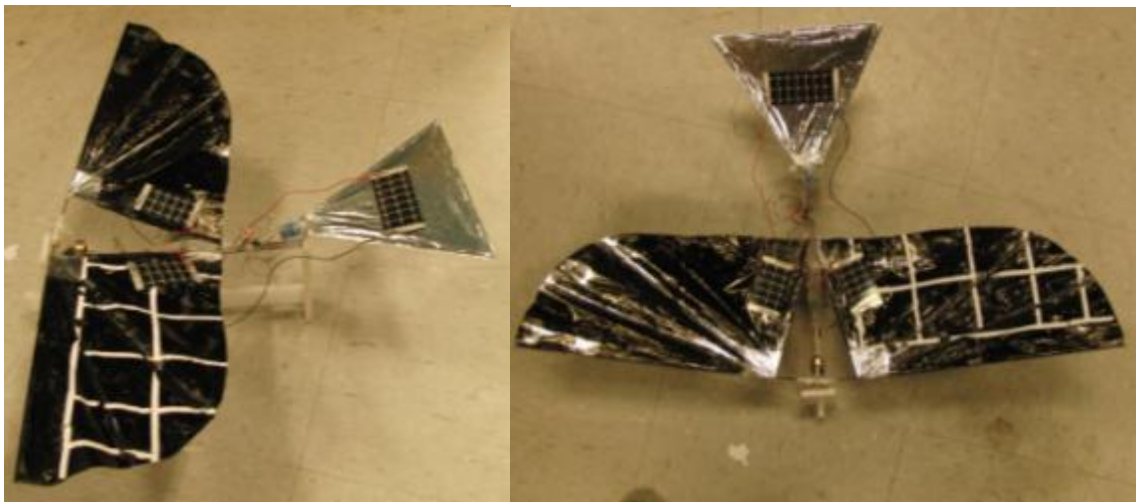
Figure 107 MAV with solar cells wired in (wing F)

6.5   Summary

This chapter detailed the multi-functional performance of the wing structures for the 'Jumbo Bird' MAV introduced in chapter 3 with the addition of the solar cells discussed in chapter 5. An equation to calculate the time-in-flight parameter of the wing based on energy stored in the battery pack, thrust generated by the wings, velocity of air, and power supplied by the solar cells was developed, with the assumptions made to derive the equation and then apply it to the MAV explicitly stated. The derived equation

was then applied to the original six wing configurations as well as the four solar cell configurations on two of the wing designs, and the resulting time-in-flight values were presented. Based on the values presented, solar cells improve performance only when the solar cell configuration generates a similar amount of thrust to the configuration without the solar cells because the solar cells used only provide approximately 1% of the power consumed by the motor. Also, the wing E design had only small variations in time-in-flight values, while the wing F design had significant variation between the original design and the solar cell configurations. From these results, it can be determined that the wing E design would be a better wing construction to implement solar cells, even though the wing F design has a better overall time-in-flight result. Next, an equation was derived to relate solar cell output to time-in-flight, allowing the multi-functionality of the MAV system to be assessed. Factors affecting this equation and the resulting multi-functionality were power, weight, wing area, solar cell area, and solar cell effectiveness. Based on this equation, the MAV tested in this thesis was not conducive to the addition of solar cells, as the power output of the solar cells was approximately 1% of the power consumption of the platform. However, should the solar cells be integrated into the smaller MAV designs at the University of Maryland, the powers would be much more compatible. The solar cells were effectively integrated into the wings of the 'Jumbo Bird' with successful flapping, but design constraints such as the flexibility of wiring were identified.

Chapter 7:   Conclusion

7.1   Contributions

This thesis is envisioned to yield several contributions in the field of MAV development by providing a new integrated approach to characterize the wing designs and create novel multi-functional wing-battery structures. The contributions of this work are in the three primary categories:

1)   A generalized wing characterization methodology has been presented and applied to six previously developed wing designs. This approach combined the leading spar displacement, the blowback measurement, the centroid calculation, the volume calculation, and the measured and calculated imaging to justify the lift and thrust results generated for the 'Jumbo Bird' MAV platform. The experimentally determined lift and thrust forces were correlated by an accurate image of the wing shape throughout the flap cycle.

2)   The presented generalized wing characterization methodology was applied to a new set of wings to determine the change in wing performance after addition of the solar cells. The results for wings with solar cells were presented and conclusions were drawn about the implications of solar cell addition on the wing compliance and the potential for the future development in that field. While integrating solar cells into wing designs has potential for improving MAV endurance, the power output of current solar cell technology is not large enough to positively affect larger MAVs such as the 'Jumbo Bird'. Implementing the solar cells used in this thesis onto smaller MAVs, such as the University of Maryland's Small Bird, may result in large gains in time-of-flight.

3)   Computational methods were developed to calculate the in-flight time and analyze the multi-functional performance of the wings with solar cells. Based on the energy stored in the battery, the wing flapping frequency, the thrust generated at a given flapping frequency, and the solar cell power, the equation allowed for quantifying the impact of the solar cells on overall wing performance.

7.2   *Anticipated Benefits*

The work presented in this thesis has the potential to open many doors in the world of miniature air vehicles, especially in terms of incorporating multi-functionality into different components. Through the integration of the wing characterization method developed, the performance of wings can be improved in both current and future designs, resulting in better performing MAVs, and thus, more consumer interest. Through the wing characterization method, the effects of small wing changes can be assessed to optimize the MAV platform for payload capacity, speed, time-in-flight, or other desired performance metric.

The introduction of solar cells as a power source is a relatively underexplored area in the field of flapping wing MAVs. Developing methods which add additional power without also increasing weight could potentially lead to multiple advancements within MAV applications. The successful integration of an additional power source allows for either the reduction of battery power, and hence, weight, resulting in greater payload capabilities; or an increase in time-in-flight to improve the long-range mission capabilities. The introduction of solar cells as a power source is envisioned to initiate new realms of multi-functionality. Implementing multi-functional wing structures is expected to expand the range of possible MAV applications.

The concepts introduced and developed in this thesis are meant to act as a launching platform for future designers. Combining the improved wing characterization method with the multi-functional concepts is envisioned to allow for further design improvement and hence, a new class of performance in miniature air vehicles.

7.3   *Future Work*

This thesis constitutes a considerable step towards development of a new and improved aerial flapping wing vehicle. There are, however, many areas in which future contributions could greatly improve the field of MAV development. This section defines the possible extensions of the work presented in this thesis.

7.3.1   Solar Cell Positioning and the Effects on Compliance

In this thesis, a new wing characterization method was developed and used to determine the effects of solar cell positioning on the compliance of flexible flapping wings. However, more work still needs to be done to better understand how the distribution of solar cells and carbon fiber spars effect the resulting compliance of flapping wings. Only four different shapes were considered in this thesis, and each solar cell shape was tested only in one location. Therefore, this wing characterization method can be extended to deal with a larger range of solar cell shapes and their positions on the wings. By increasing the number of shapes, as well as testing multiple solar cell shapes in multiple locations, a better understanding of the effect of solar cell distribution on compliance can be developed.

7.3.2 Solar Cell Integration into Wing Material

In this thesis, a method of integrating flexible solar cells into Mylar-based foil flexible flapping wings was developed to make the wings as multi-functional structures. However, the integration introduced a reduction in compliance due to both the wiring and the packaging of the solar cells. The stiffness of the wires used to connect the solar cells with the electrical system affected the wing motion during the flap cycle and thus, altered compliance of the wings. While the packaging used to hold the solar cells was made of flexible material, it was still less flexible than the Mylar-based foil used in the wings, and hence, reduced the wing compliance. Therefore, integration of wiring into the wing structure and eventually, the integration of the entire solar cell into the wing film itself are the required development areas in order to further reduce the effects of solar cells on compliance.

7.3.3 Development of Strain Calculation

In this thesis, a wing characterization method was developed to analyze the deformations of different points on the wing and use them to create the measured and calculated imaging. However, the method used does not present a straightforward way to calculate the strains on the object at different points. Therefore, the wing characterization method can be extended to include a strain measurement based on flapping wing deformations. Knowing the strains at different points on the wing should allow for concentration areas to be identified and the wing performance to be improved. Modifying the wing characterization method to use the digital image correlation is one possible way to incorporate the strain determination within the wing characterization method.

7.3.4   Digital Image Correlation of Wings

In this thesis, a wing characterization method was developed to provide accurate wing shapes and correlate the lift and thrust values to the wing images. However, this optical technique was based on a fifteen-point mapping of the wing shape, which limits the precision of the technique. Therefore, this wing characterization method can be extended to involve digital image correlation and tracking. Once a proper system is built and calibrated, the use of digital image correlation on the wings will allow for deformation, displacement, and strain to be calculated for thousands of points on the wing surface, greatly enhancing the quality of the wing characterization.

7.3.5   Application of characterization in other aspects of MAV

In this thesis, a new wing characterization method was developed to analyze the flapping wings of the MAVs. However, this characterization method does not take into account any of the other aspects of the MAV platform. Therefore, the wing characterization method that was developed can be extended to the tail design, the body design, and the electronic components. The method would allow for the development of an integrated optimization approach that would maximize different performance characteristics. By determining the best way to create different parts of the MAV platform, huge improvements can be made in MAV technology.

References

[1] Epson, 2004, Epson Announces Advanced Model of the World's Lightest Micro-Flying Robot, February 3,
http://global.epson.com/newsroom/news_2004_08_18.htm

[2] Tsuzuki, N., Sato, S., and Abe, T., 2007, "Design Guidelines of Rotary Wings in Hover for Insect-Scale Micro Air Vehicle Applications," *Journal of Aircraft*, Vol. **44** (1), pp. 252-263.

[3] Albertani, R., Stanford, B., Hubner, J. P., and Ifju, P., 2005, "Characterization of Flexible Wing Mavs: Aeroelastic and Propulsion Effects on Flying Qualities," *Proceedings of the AIAA Atmospheric Flight Mechanics Conference and Exhibit*, San Francisco, California.

[4] Viieru, D., Albertani, R., Shyy, W., and Ifju, P., 2005, "Effect of Tip Vortex on Wing Aerodynamics of Micro Air Vehicles," *Journal of Aircraft*, Vol. **42** (6), pp. 1530-1536.

[5] Finio, B. M., Shang, J. K., and Wood, R. J., 2009, "Body Torque Modulation for a Microrobotic Fly," *Proceedings of the IEEE International Conference on Robotics and Automation*, Kobe, Japan, pp. 3449-3456.

[6] Thomas, J.P. Thomas and Qidwai, M.A., 2005, "The Design and Application of Multifunctional Structure-Battery Materials Systems," *JOM*, Vol **57** (3), pp. 18-24.

[7] J.W. Gerdes, S.K. Gupta, and S. Wilkerson, "A Review of Bird-inspired Flapping Wing Miniature Air Vehicle Designs," In Proceedings of the ASME Mechanism and Robotics Conference, Montreal, Canada, August, 2010.

[8] Pornsin-Sirirak, T., Tai, Y., Ho, C., and Keennon, M., 2001, "Microbat: A Palm-Sized Electrically Powered Ornithopter," *Proceedings of the NASA/JPL Workshop on Biomorphic Robotics*, Pasadena, CA.

[9] Yang, L.-J., Hsu, C.-K., Ho, J.-Y., and Feng, C.-K., 2007, "Flapping Wings with Pvdf Sensors to Modify the Aerodynamic Forces of a Micro Aerial Vehicle," *Sensors and Actuators A: Physical*, Vol. **139** (1-2), pp. 95-103.

[10] Hsu, C.-K., Ho, J.-Y., Feng, G.-H., Shih, H.-M., and Yang, L.-J., 2006, "A Flapping Mav with Pvdf-Parylene Composite Skin," *Proceedings of the Asia-Pacific Conference of Transducers and Micro-Nano Technology*.

[11] Madangopal, R., Khan, Z., and Agrawal, S., 2005, "Biologically Inspired Design of Small Flapping Wing Air Vehicles Using Four-Bar Mechanisms and Quasi-Steady Aerodynamics," *Journal of Mechanical Design*, Vol. **127** (4), pp. 809-817.

[12] Bejgerowski, W., Ananthanarayanan, A., Mueller, D., and Gupta, S., 2010, "Integrated Product and Process Design for a Flapping Wing Drive-Mechanism," *Journal of Mechanical Design,* Vol. **50**, pp.725-735.

[13] Mueller, T. J., 2001, "Fixed and Flapping Wing Aerodynamics for Micro Air Vehicle Applications," American Institute of Aeronautics and Astronautics, Reston, VA.

[14] Osaka Slow Fliers Club, January 4, http://blog.goo.ne.jp/flappingwing.

[15] Ltd, F. T., 2009, Wingsmaster Ornithopters, March 17, http://www.flyingtoys.com/index.php?categoryID=28.

[16] Delfly, T., 2005, Delfly, January 4, http://www.delfly.nl/?site=DI&menu=&lang=en.

[17] Jones, K. D., Bradshaw, C. J., Papadopoulos, J., and Platzer, M. F., 2004, "Improved Performance and Control of Flapping-Wing Propelled Micro Air Vehicles," *Proceedings of the AIAA 42nd Aerospace Sciences Meeting and Exhibit*, Reno, Nevada.

[18] Berg, C. V. D., and Ellington, C., 1997, "The Vortex Wake of a 'Hovering' Model Hawkmoth," *Philos Trans Roy Soc Lond Ser B-Biol Sci*, Vol. **352** (1351), pp. 317-328.

[19] Ellington, C., Berg, C. V. D., Willmott, A., and Thomas, A., 1996, "Leading-Edge Vortices in Insect Flight," *Nature*, Vol. **384** (6610), pp. 626-630.

[20] Birch, J., and Dickinson, M., 2001, "Spanwise Flow and the Attachment of the Leading-Edge Vortex on Insect Wings," *Nature*, Vol. **412** (6848), pp. 729-733.

[21] Dickinson, M., Lehmann, F., and Sane, S., 1999, "Wing Rotation and the Aerodynamic Basis of Insect Flight," *Science*, Vol. **284** pp. 1954-1960.

[22] Dickinson, M., and Gotz, K., 1993, "Unsteady Aerodynamic Performance of Model Wings at Low Reynolds Numbers," *Journal of Experimental Biology*, Vol. **174** pp. 45-64.

[23] Wang, Z., Birch, J., and Dickinson, M., 2004, "Unsteady Forces and Flows in Low Reynolds Number Hovering Flight: Two-Dimensional Computations Vs. Robotic Wing Experiments," *Journal of Experimental Biology*, Vol. **207** pp. 449-460.

[24] Weis-Fogh, T., 2005, "Quick Estimates of Flight Fitness in Hovering Animals, Including Novel Mechanisms for Lift Production," *Journal of Experimental Biology*, Vol. **59** (1973), pp. 169-230.

[25] Hsu, C.-K., Evans, J., Vytla, S., and Huang, P., 2010, "Development of Flapping Wing Micro Air Vehicles - Design, Cfd, Experiment and Actual Flight," Orlando, Florida.

[26] Breugel, F. V., Teoh, Z. E., and Lipson, H., 2009, *Flying Insects and Robots*, Springer Berlin Heidelberg.

[28] Mueller, D., Gerdes, J., and Gupta, S., 2009, "Incorporation of Passive Wing Folding in Flapping Wing Miniature Air Vehicles," San Diego, CA.

[29] Billingsley, D., Slipher, G., Grauer, J., and Hubbard, J., 2009, "Testing of a Passively Morphing Ornithopter Wing," AIAA Paper Number 2009-1828.

[30] Billingsley, D., and Hubbard, J., 2007, "Passive Wing Morphing for Improved Lift in Flapping Wing Ornithopters," *Proceedings of the AIAA Student Conference Region I-MA*.

[31] Hovo, J.D., Elliott, A., and Christie, D.A., 1992, *Handbook of the Birds of the World*, Barcelona.

[32] Ornithology, C. L. O., 2003, Baltimore Oriole, March 17, http://www.birds.cornell.edu/AllAboutBirds/BirdGuide/Baltimore_Oriole.html.

[33] Olszewski, A., 1997, The Canary Faq, March 19, http://www.upatsix.com/faq/canary.htm.

[34] Harper, E. J., Lambert, L., and Moodie, N., 1998, "The Comparative Nutrition of Two Passerine Species: The Canary (*Serinus Canarius*) and the Zebra Finch (*Poephila Guttata*)," *The Journal of Nutrition*, Vol. **128** pp. 2684S-2685S.

[35] Suarez, R., 1992, "Hummingbird Flight: Sustaining the Highest Mass-Specific Metabolic Rates among Vertebrates," *Cellular and Molecular Life Sciences*, Vol. **48** (6), pp. 565-570.

[36] Pearson, O., 1950, "The Metabolism of Hummingbirds," *The Condor*, Vol. **52** (4), pp. 145-152.

[37] 2009, Northern Cardinal, March 17, http://www.birds.cornell.edu/AllAboutBirds/BirdGuide/Northern_Cardinal.html.

[38] Sl Halkin, S. L., 1999, "Northern Cardinal (Cardinalis Cardinalis)," *The Birds of North America*, Vol. **440** (32).

[39] J.P. Thomas et al, "Multifunctional Structure-Plus-Power Concepts," *AIAA*, (2002-1239), pp. 1-11.

[40] P. Liu, E. Sherman, and A. Jacobsen, "Design and Fabrication of Multifunctional Structural Batteries," *Journal of Power Sources*, 189 (2008), pp. 646-650.

[41] Ifju, P.J., Stanford, B., Sytsma, M., and Albertani, R., "Analysis of a Flexible Wing Micro Air Vehicle," In Proceedings of the AIAA Aerodynamic Measurement Technology and Ground Testing Conference, San Francisco, California, June, 2006.

[42] Stanford, B., Albertani, R. Viieru, D., Shyy, W., and Ifju, P., "Static Aeroelastic Model Validation of Membrane Micro Air Vehicle Wings," In Proceedings of the AIAA Aerospace Sciences Meeting and Exhibit, Reno, Nevada, January 2007.

[43] Gerdes, J., 2010, "Design, Analysis, and Testing of a Flapping Wing Miniature Air Vehicle", Master's thesis, University of Maryland, College Park..

[44] March 17, 2010, http://www.wes-technik.de/English/Motors-Brushless.htm.

[45] June 19, 2010, http://www.bphobbies.com/view.asp?id=A0780191&pid=B1908555.

[46] June 19, 2010, www.microinvent.com.

[57] June 19, 2010, http://www.bphobbies.com/view.asp?id=V253880&pid=D2635028.

[58] March 19, 2010, http://www.bsdmicrorc.com/index.php?productID=520.

[49] W. Bejgerowski, J.W. Gerdes, S.K. Gupta, H.A. Bruck and S. Wilkerson, "Design and fabrication of a multi-material compliant flapping wing drive mechanism for miniature air vehicles," In Proceedings of the ASME Mechanism and Robotics Conference, Montreal, Canada, August, 2010.

[50] March 4, 2010, http://www.omega.com/Pressure/pdf/LCFD.pdf.

[51] March 9, 2010, http://www.edmundoptics.com/onlinecatalog/displayproduct.cfm?productID=1618.

[52] November 1, 2010, http://www.siliconsolar.com/flexible-solar-panels-3v-051285-p-500994.html.

[53] D. Mueller, H.A. Bruck, and S.K. Gupta, (2010), "Measurement of Thrust and Lift Forces Associated With Drag of Compliant Flapping Wing for Micro Air Vehicles Using a New Test Stand Design," *Experimental Mechanics*, Vol **50**, pp. 725-735.

[54] D.J. Pines and F. Bohorquez, (2006), "Challenges Facing Future Micro-Air-Vehicle Development," *Journal of Aircraft*, Vol **43** (2), pp. 290-305.